ANALYSIS OF AUTOMOTIVE TURBOCHARGER NONLINEAR VIBRATIONS INCLUDING BIFURCATIONS

A Thesis

by

ARIAN VISTAMEHR

Submitted to the Office of Graduate Studies of
Texas A&M University
in partial fulfillment of the requirements for the degree of

MASTER OF SCIENCE

August 2009

Major Subject: Mechanical Engineering

ANALYSIS OF AUTOMOTIVE TURBOCHARGER NONLINEAR

VIBRATIONS INCLUDING BIFURCATIONS

A Thesis

by

ARIAN VISTAMEHR

Submitted to the Office of Graduate Studies of
Texas A&M University
in partial fulfillment of the requirements for the degree of

MASTER OF SCIENCE

Approved by:

Chair of Committee, Luis San Andrés
Committee Members, Alan Palazzolo
　　　　　　　　　　Monique Hite Head
Head of Department, Dennis L. O'Neal

August 2009

Major Subject: Mechanical Engineering

ABSTRACT

Analysis of Automotive Turbocharger Nonlinear Response
Including Bifurcations. (August 2009)
Arian Vistamehr, B.S., Texas A&M University
Chair of Advisory Committee: Dr. Luis San Andrés

Automotive turbochargers (TCs) increase internal combustion engine power and efficiency in passenger and commercial vehicles. TC rotors are usually supported on floating ring bearings (FRBs) or semi-floating ring bearings (SFRBs), both of which are inexpensive to manufacture. However, fluid film bearings are highly nonlinear components of TC units and contribute to the complex behavior (i.e. bifurcations and frequency jumps between a first whirl frequency and a second whirl frequency) of the entire rotor-bearing system (RBS). The frequency jump phenomenon concerns the TC manufacturing industry due to increased levels of noise generation. This thesis presents progress on assessing the effects of some bearing parameters and operating conditions on the RBS dynamic forced performance and the frequency jump phenomenon.

A fluid film bearing model is integrated into a finite element rotordynamics computational model for numerical prediction of the TC linear and nonlinear (time transient) forced response. Since automotive TCs operate with variable rotational speed, predictions are conducted with shaft acceleration/deceleration.

Over most of its operating speed range, TC rotor nonlinear response predictions display two subsynchronous whirl frequencies ω_1 and ω_2 representing a conical mode and a cylindrical bending mode, respectively. At low shaft speeds ω_1 is present up to a shaft speed $(\Omega_{bifurcation})$, where there is a frequency jump from ω_1 to ω_2. The second whirl frequency may persist up to the highest shaft speeds (depending on operating conditions). Results show during rotor deceleration the $\Omega_{bifurcation}$ may be different from the one during rotor acceleration (hysteresis).

Predictions show the following factors delay the $\Omega_{bifurcation}$: increasing oil supply pressure, decreasing oil supply temperature, and increasing shaft acceleration. Also,

rotor imbalance distribution greatly affects $\Omega_{bifurcation}$ and the shaft amplitude of total motion.

Overall, this study shows the sensitivity of bifurcations and frequency jump phenomenon in TC nonlinear response due to various bearing parameters and operating conditions. Further analysis is required to generalize these findings and to assess the effect of other bearing parameters (i.e. clearances, outer film length, ring rotation, etc.) on this phenomenon. In addition further validation of the predictions against test data is required for refinement of the predictive tool.

DEDICATION

I dedicate my thesis to my parents, Nasrin and Homayoun Vistamehr. I admire them for sacrificing the joy of living with the family, and for letting me go thousands of miles away from home to achieve a better education, and a refined mindset. I thank them for their extraordinary vision, their unconditional love and continuous support.

I also dedicate my thesis to all the interested readers in academia and industry.

ACKNOWLEDGEMENTS

TABLE OF CONTENTS

LIST OF FIGURES

Page

LIST OF TABLES

CHAPTER I

INTRODUCTION

Turbochargers (TCs) increase internal combustion engine power and efficiency in passenger and commercial vehicles. TCs consist of a thin shaft with a turbine wheel friction welded at one end and compressor wheel (slide in) at the other end. TC rotors are usually supported on floating ring bearings (FRBs) or semi-floating ring bearings (SFRBs), both of which are inexpensive to manufacture and last longer than other types of bearings (i.e. ball bearings). Figure 1 depicts a TC supported on a SFRB. Oil is supplied through the center housing to the compressor and turbine fluid film bearings. Note the anti-rotation pin hole in the middle of the SFRB. SFRBs are pinned and restrained from rotation. Therefore, the motion in SFRBs is limited to precession, whereas in FRBs the ring is free to rotate. As the lubricant is supplied, (S)FRBs form two fluid films in series; the inner film (between the journal and inner ring) and the outer film (between the outer ring and center housing). SFRBs are advantageous over FRBs due to lesser power loss [1] .
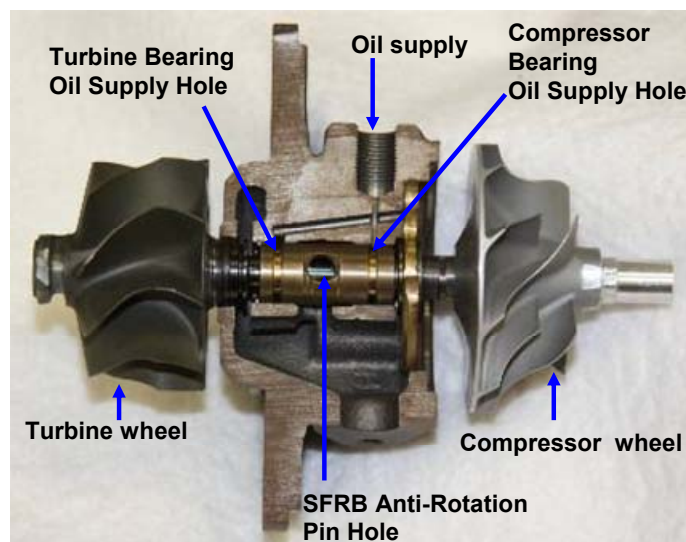
Figure 1: Turbocharger supported on SFRB

_____

This thesis follows the style of Journal of Engineering for Gas Turbines and Power.

Hot exhaust gas from the engine drives the turbine wheel that is connected through the shaft to the compressor wheel. The compressor feeds air to the engine intake manifold. This process improves the air/fuel ratio for a more efficient and a cleaner combustion. Air/fuel ratio is one of the main factors influencing the composition of the exhaust emission. For instance, insufficient amount of air mixing with the fuel in the combustion chamber, leads to increased hydrocarbons (HCs) emissions in diesel engines [2].

Fluid film bearings provide viscous damping. However, in some instances these bearings are prone to induce a condition called subsynchronous oil whirl, where the RBS (rotor-bearing system) motion response contains one or more frequencies at fractions of the rotor (and ring in case of a FRB) rotational frequency. Fluid film bearings are highly nonlinear components of TC units and responsible for the complex behavior of the entire RBS [3].

TC rotors operate at high rotational speeds. Due to heat generation and shaft and casing thermal gradients, changes in lubricant properties (i.e. viscosity) and thermal growth of the rotor and the bearings must be considered. The inner and outer film clearances, ring rotational speed (in FRBs), and journal and ring eccentricities are functions of the shaft rotational speed, shaft temperature, and oil inlet pressure and temperature. These parameters play a crucial role in the RBS response behavior [4]. As the rotor speed increases, subsynchronous whirl motions appear with increasing amplitudes. However, at high shaft speeds, sometimes due to fluid film bearing nonlinearities, rotor imbalance can limit the amplitude of TC rotor subsynchronous motions [5]. The TC shaft motion often reaches a limit cycle within the rotor-bearing clearance physical limit, which allows TC units to operate safely at high speeds [6].

Turbocharger performance assessment involves rigorous testing which is both costly and time consuming. Significant time and costs can be saved by replacing the shop assessment with a proven predictive model, experimentally benchmarked. The development and refinement of such model has been the goal of a research project [1], [3-7] over nearly the past decade at Texas A&M University.

A fluid film bearing model [7], accounting for the thermal energy transport between the fluid films and the bounding solids, predicts the hydrodynamic pressure generation and bearing performance characteristics (i.e. inner/outer film clearances, oil viscosities, lubricant flow rate, ring rotational speed, power loss and bearing reaction forces). This flow model is integrated to a finite element rotordynamics code, XLTRC^2™ [8], for predicting linear and nonlinear rotordynamic responses. The nonlinear predictive model assists the design and optimization of high performance, high reliability TC RBS.

CHAPTER II

FREQUENCY JUMP PHENOMENON IN TC ROTORDYNAMIC RESPONSE

(BETWEEN THE 1ST AND THE 2ND WHIRL FREQUENCIES)

Figures 2-6 depict the waterfalls of measured TC center housing accelerations (at the oil outlet location) provided by Honeywell Turbo Technologies (HTT) [9]. The TC shaft is supported on a SFRB for results shown in Figures 2, 3, 4, and 6. Figure 5 depicts similar waterfalls recorded in a TC supported on FRBs [10]. The horizontal axis shows frequency content, the vertical axis shows the rotor speed, and the color intensity denotes amplitude of acceleration. The following color pattern shows the increasing order of response amplitude: dark blue, light blue, green, yellow, orange, and red. Therefore, red corresponds to the highest acceleration amplitude. The oil inlet pressure and temperature corresponding to the case in Fig. 2 are 4 bar and 30°C, respectively. Synchronous and subsynchronous frequencies are labeled in all figures. According to Ref. [10], at low shaft speeds (< 1,800 Hz = 108 krpm) the dominant whirl frequencies are ω_1 (conical mode) and $2\omega_1$. In the speed range between 1,500 Hz and 1,800 Hz oil whip phenomenon seem to occur, where the first whirl frequency (ω_1) and its multiples ($2\omega_1$ and $3\omega_1$) lock (also known as whip) at the system natural frequency[*]. As shaft speed (Ω) increases, the whirl motion, ω_1, bifurcates to another branch of frequency, $\Omega - \omega_2$ (shaft speed minus the second whirl frequency, ω_2). At a certain speed $(\Omega_{bifurcation})$, ω_1 vanishes and the second whirl frequency (cylindrical mode) appears with a high amplitude of acceleration (red color). Hence, at this speed, $(\Omega_{bifurcation})$, there is apparently a jump from the first to the second subsynchronous whirl frequency. The

---

[*] Note according to the TC manufacturer, the natural frequencies of the RBS calculated using an eigenvalue analysis, do not correspond to the measured subsynchronous frequencies (ω_1 and ω_2). Therefore, one cannot make a definitive statement regarding the occurrence of oil whip phenomenon in the measured results. In addition, the TC manufacturer determines (using a visual software and predicted test data) that the rotor whirls in a conical mode at shaft speeds where ω_1 is the dominant frequency, and it whirls in a cylindrical bending mode at high shaft speeds where ω_2 is dominant. Based on the information provided by the TC manufacturer, one cannot conclude whether ω_1 and ω_2 correspond with actual rotor-bearing system natural frequencies [11].

second whirl motion is dominant at rotor speeds higher than the bifurcation speed [10]. HTT states that there is sudden increase in noise generation associated with this frequency jump (from 1st to 2nd whirl frequency). Therefore, the jump phenomenon is of concern to TC manufacturers. In vibration (and acoustic) measurements obtained in a passenger vehicle, a gas-stand test rig, and a VSR (Vibration Sorting Rig), HTT engineers [9-10] detected the jump phenomenon from the first to the second subsynchronous whirl frequency in TC rotors supported on both FRBs and SFRBs.

One can find relations between the whirl frequencies and the operating speed by measuring the synchronous and subsynchronous frequencies at the bifurcation speed. In the results shown in Figs. 2-4, it appears the bifurcation speed $(\Omega_{bifurcation})$ is equal to twice the first whirl frequency plus the second whirl frequency $(\Omega_{bifurcation} \sim 2\omega_1 + \omega_2)$. In vibration this is called a combined resonance if ω_1 and ω_2 represent the system natural frequencies [12]. This type of combined resonance occurs in systems with for example, a cubic nonlinearity such as Duffing-type systems [10] , [13]. In addition, at the bifurcation speed, three times the first natural frequency is approximately equal to twice the second natural frequency $(3\omega_1 \sim 2\omega_2)$. In other words, (if ω_1 and ω_2 represent the system natural frequencies) there is a 3:2 internal resonance between the first and second natural frequencies of the TC system. Yamamoto and Ishida [12] introduce internal resonance as a means of energy transfer between the natural modes. Moreover, they hold nonlinearities responsible for energy transfer between the natural modes.

Figure 3 depicts the waterfalls of measured center housing accelerations for the same TC RBS at 100°C and 4 bar oil inlet temperature and pressure, respectively. The operating conditions are identical to the ones stated in Fig. 2 except the oil inlet temperature increases to 100°C. The relations between the whirl frequencies and the running speed are the same as the ones found in the data shown in Fig. 2. Note the bifurcation shaft speed $(\Omega_{bifurcation})$ drops to a lower speed (~1,400 Hz = 84 krpm) just by increasing the oil inlet temperature. As a reminder, the bifurcation speed corresponding to the case with 30°C oil temperature is 1,800 Hz (108 krpm). HTT reports that the bifurcation speed is sensitive to the oil temperature [10]. The sensitivity of the bifurcation speed to oil inlet temperature is especially interesting. In prior studies, for a

TC supported on FRBs, Holt *et al.* [5] observe from TC casing acceleration measurements, the presence of two sets of subsynchronous whirl motions. At low speeds only one set of subsynchronous whirl is present. At a certain shaft speed, the first whirl frequency disappears and the second whirl frequency appears with a higher amplitude of acceleration. The test data does not show any oil whip. Holt *et al.* report increasing oil inlet pressure delays the onset speed of second subsynchronous whirl appearance; however, the oil temperature has a minimal effect. Nevertheless, a decreasing oil inlet temperature acts to reduce the amplitudes of synchronous and subsynchronous motions due to the lubricant higher viscosity.
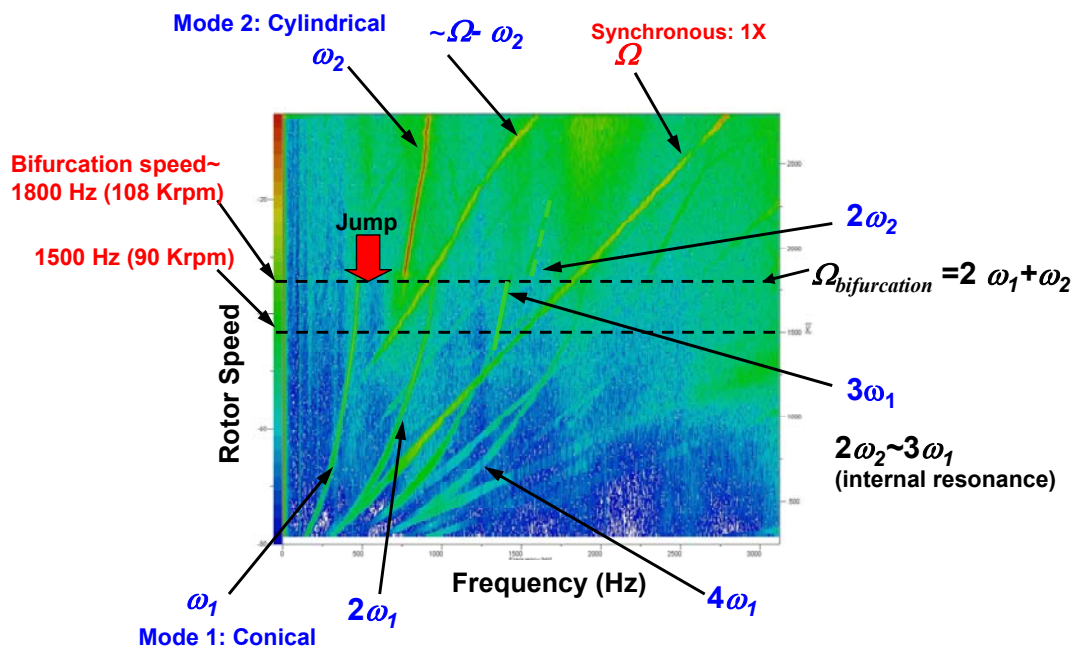
Figure 2: Waterfalls of TC center housing acceleration for **30°C** oil inlet temperature and **4bar** oil inlet pressure [9]
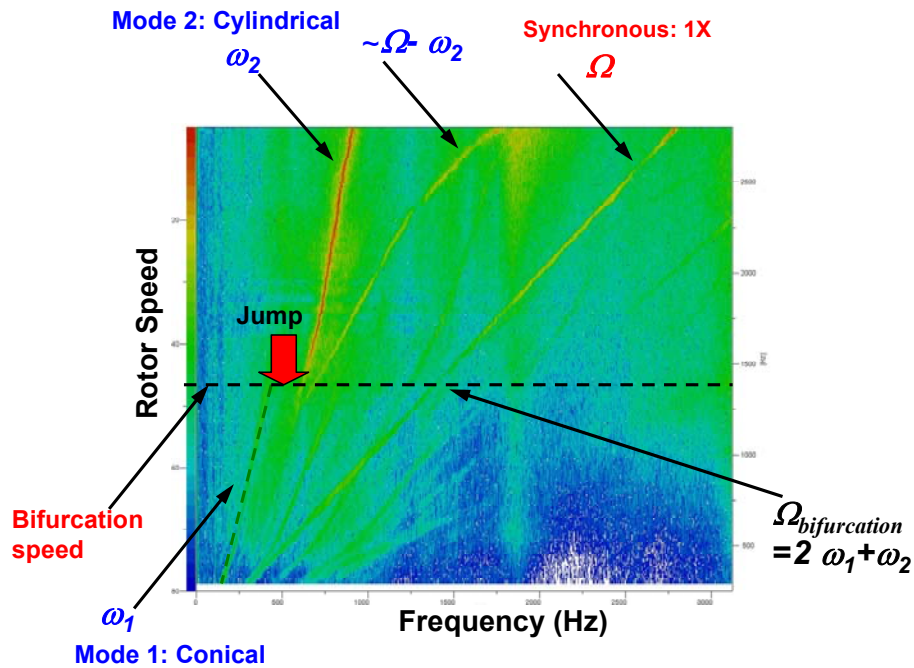
Figure 3: **Waterfalls of TC center housing acceleration for 100°C oil inlet temperature and 4bar oil inlet pressure [9]**

Figure 4 depicts waterfalls of measured center housing acceleration. The oil inlet temperature and pressure are 30°C and 4bar, respectively. Measurements are taken while the TC shaft accelerates. The relations between the whirl frequencies and the running speed (at the bifurcation speed) are identical to the ones found in the data of Figs. 2 and 3. At a rotor speed below the bifurcation speed $(\Omega_{bifurcation})$, the dominant whirl frequencies are ω_1 (conical mode) and $2\omega_1$. However, beyond the bifurcation speed, the second whirl frequency ω_2 (cylindrical mode) is dominant. The dark lines indicate high amplitudes of motion. Hence, a cylindrical mode with high amplitude continues to be the dominant whirl motion at speeds beyond the bifurcation speed [10].
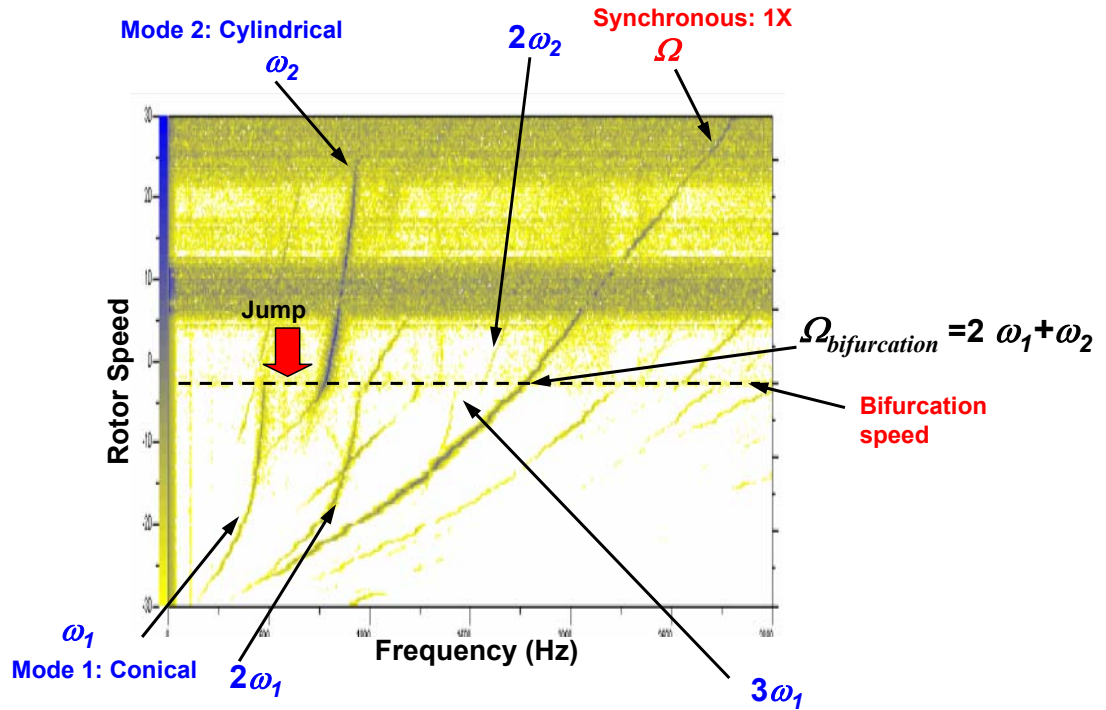
Figure 4: Waterfalls of TC center housing acceleration as the shaft accelerates [10]
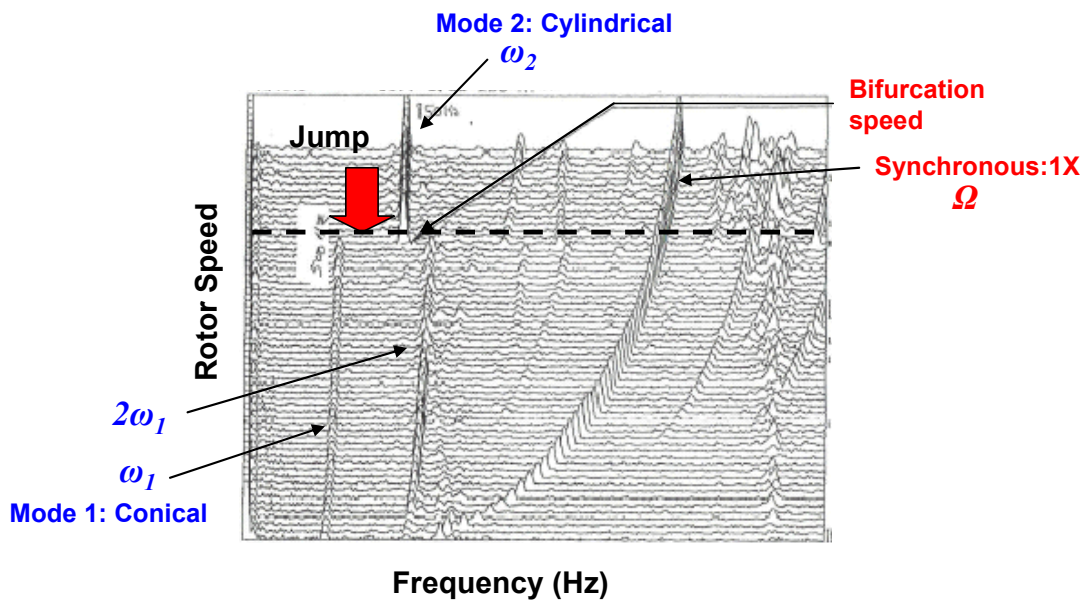
Figure 5: Waterfalls of TC center housing acceleration as the shaft accelerates, TC supported on FRBs [10]

For a TC supported on SFRBs, Figure 6 depicts the waterfalls of TC housing acceleration at 30°C oil inlet temperature and 4 bar oil inlet pressure. Results in Fig. 6 (a) correspond to a rotor with higher imbalance amount. Expectedly, increasing the imbalance amount increases the amplitude of synchronous motion, but more interestingly, note the disappearance of the first and second subsynchronous whirl frequencies at shaft speeds above 60 krpm (1000Hz).

In addition to lubricant temperature, HTT suggests that the bifurcation speed is sensitive to the rotor imbalance distribution and amount. This observation is based on test data in Fig. 6 (from Ref. [9]) and some rotordynamic predictions on a TC supported on a SFRB [14]. However, no technical reports are advanced by HTT regarding this observation. Hence, according to HTT, the rotor bifurcation speed varies with oil inlet temperature, imbalance distribution and amount, and how fast the rotor accelerates or decelerates. However, the type of bearing (SFRB or FRB) and the oil inlet pressure appear to play lesser significant roles [10].
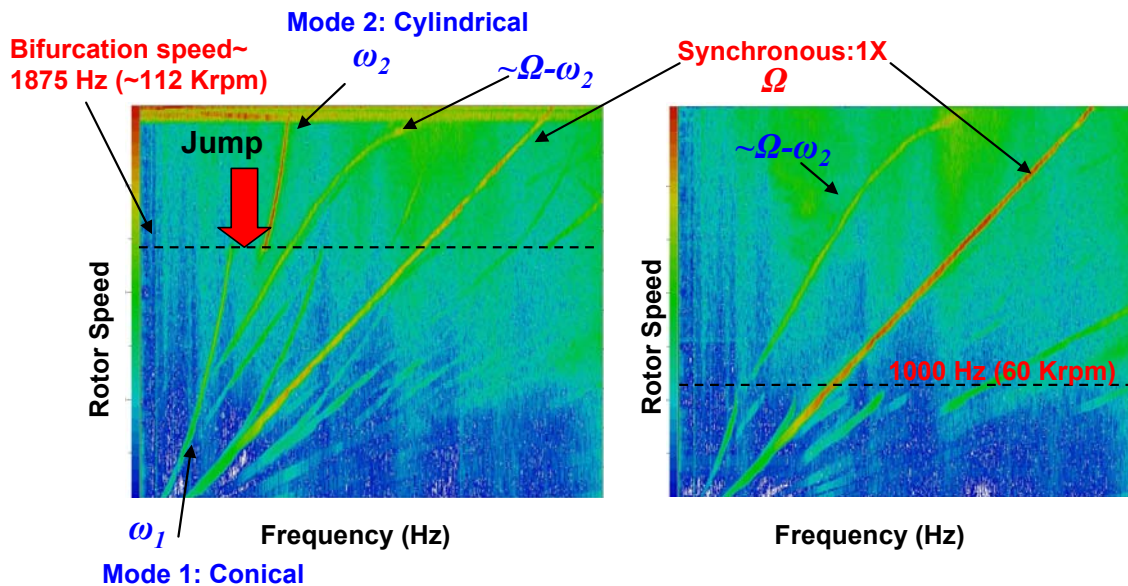
Figure 6: **Waterfalls of TC center housing acceleration for 30°C oil inlet temperature and 4bar oil inlet pressure; (a) low imbalance amount, (b) high imbalance amount. TC supported on SFRB [9]**

As mentioned earlier, the jump phenomenon from the first to the second whirl frequency generates noise, and that is the main concern to TC manufacturers. Sahay and LaRue [15] note subsynchronous whirl in turbochargers as the second major source of structural noise generation (the first source is rotor imbalance).

A parametric study on the bearing performance characteristics as well as rotor responses for a TC supported on (S)FRBs (using computational tools such as a fluid film bearing thermo-hydrodynamic model [7] and XLTRC^2™ rotordynamics code [8]) will provide useful insight which can lead to a better understanding of the jump phenomenon. In order to accomplish this, it is critical to understand the fundaments of modal interactions and nonlinearities in rotordynamics. Recall that TCs supported on fluid film bearings display highly nonlinear characteristics. The following section presents a literature review of the past work related to modal interactions as a result of internal and combined resonances in nonlinear systems.

CHAPTER III

LITERATURE REVIEW

As Noah and Sundararajan [16] point out, rotors supported on fluid film bearings display a highly nonlinear behavior, which linear analysis cannot predict. A few examples of nonlinear behavior include subsynchronous, quasi-periodic and chaotic responses; all occurring in rotating machinery with nonlinear supports. For instance, rotating multi-shaft systems exhibit multi frequency excitations which may lead to quasi-periodic response and even chaos [16].

The stability of a dynamic system can be analyzed using Hopf bifurcation theory. This theory explains how a dynamic system behaves qualitatively based on the motion of the system's Eigenvalues in complex plane. Consider the Eigenvalues (pair of complex conjugate) of a RBS linearized at the static equilibrium position of the rotor. As the rotor speed varies, at a certain critical speed, Ω_0, the real parts of a pair of complex conjugate Eigenvalues cross the imaginary axis and enter the positive (real part) region. It is said that the fixed stable point (at static equilibrium position) loses stability and bifurcates into a limit cycle, which can be either stable (if the bifurcation is supercritical) or unstable (if the bifurcation is subcritical) [17].

In cases where a subcritical bifurcation occurs, the system response can display a phenomenon known as hysteresis [18]. Pinkus [19] observes hysteresis in the rotor onset (and disappearance) speed of instability. He describes during rotor acceleration, the onset speed of instability is higher than the speed at which the instability disappears (return to stable region) during rotor deceleration. Muszynska [20] attributes the occurrence of hysteresis in RBS response to the fluid mean circumferential velocity which is smaller during rotor acceleration than during rotor deceleration. Wang and Khonsari [18] investigate the effect of lubricant viscosity on hysteresis in RBS instability. Analytical results show that subcritical bifurcations and hysteresis occur with high viscosity oil. Therefore, by controlling the lubricant temperature (and hence its viscosity) one can control the hysteresis phenomenon.

Choi and Noah [21] state the increase in significance of fluid film bearing nonlinear effects at higher speeds in rotating machinery. They introduce hydrodynamic bearings with clearance as highly nonlinear components in rotating machinery. As a result of nonlinearities in hydrodynamic bearings, subsynchronous whirl motions and bifurcations of periodic motions into quasi-periodic motions may occur in rotor-bearing systems. The authors use a fixed point algorithm (FPA) to solve for quasi-periodic solutions of a nonlinear Jeffcott rotor with imbalance. Then, a Winding (or rotation) number, obtained numerically, is introduced to assist in identifying any trends in nonlinear system behavior. The Winding (rotation) number is the ratio of forcing frequency to Hopf bifurcation frequency. Choi and Noah [21] observe that in certain regions the forcing frequency (rotor frequency) locks to a system natural frequency. This locking phenomenon occurs below certain forcing amplitude (critical amplitude). However, above the critical forcing amplitude, chaotic response appears in addition to subsynchronous and quasi-periodic responses.

Brown *et al.* [22] describe that chaotic motions can occur in rotors supported on journal bearings for a certain values of imbalance and rotor speed. For instance, at high journal eccentricities, the total vertical load (caused by static load and vertical component of imbalance excitation force) may be very small at some portions of an orbit. This event may give rise to chaos. Chaotic motion can also occur in systems with weak gyroscopic effects. Inoue and Ishida [23] observe chaotic motion at the fundamental and twice the fundamental critical speed in a 2DOF rotor model with weak nonlinearity and weak gyroscopic effects. In this case, the absolute value of forward (ω_f) and backward (ω_b) critical speeds become almost equal. Since $\omega_f \sim -\omega_b$, the combined resonance $\Omega = 0.5(\omega_f - \omega_b)$ results in $\Omega \sim \omega_f$. If the gyroscopic effects are completely neglected, the magnitudes of the forward, backward critical speeds and combined resonance $0.5(\omega_f - \omega_b)$ coincide; and interestingly, chaotic motion does not occur.

One of the means for energy transfer between the natural modes of a nonlinear system is internal resonance. If at a certain operating speed, two (or more) of the natural frequencies are rational multiples of each other, an internal resonance may occur. In other words, it is said that those natural frequencies are commensurate. Yamamoto and

Ishida [12] as well as Nayfeh and Balachandran [13] hold nonlinearities responsible for the occurrence of internal and combined resonances in multi-degree-of-freedom (multi-DOF) systems. The two resonance phenomena can couple the natural modes of a system and cause an exchange of energy among the coupled modes. Moreover, the modal interactions may lead to quasi-periodic and chaotic responses.

In Ref [17], Shaw and Shaw explain the critical role of the Winding (rotation) number in determining the dynamic behavior of a system. For instance, based on how commensurate the rotation number is, the bifurcating limit cycle can become periodic, quasi-periodic, or chaotic. Moreover, consider a system with a cubic nonlinearity, where Ω is the rotor speed (forcing frequency) and ω is the bifurcating limit cycle frequency. In this case, the strongly resonant cases are 1:1 ($\Omega \sim \omega$), 2:1 ($\Omega \sim 2\omega$), and 3:1 ($\Omega \sim 3\omega$). Most interestingly, Shaw and Shaw state that jump phenomenon is often observed in these resonant conditions.

Nayfeh and Balachandran [13] review the related work to systems with internal and combined resonances. Consider ω_n and ω_m as any two natural frequencies of the system where $n>m$. The 1:1 internal resonance ($\omega_n \sim \omega_m$) occurs in systems with quadratic or cubic nonlinearities. The 2:1 internal resonance ($\omega_n \sim 2\omega_m$) occurs in systems with quadratic nonlinearities; and the 3:1 internal resonance ($\omega_n \sim 3\omega_m$) occurs in systems with cubic nonlinearities. The combination internal resonance can occur in systems with quadratic and/or cubic nonlinearities. Therefore, the degree of nonlinearity determines the type of internal resonance. The possible types of combined resonance in systems with quadratic and cubic nonlinearities are given in detail in Ref.[13].

One of the particularly interesting effects of internal resonance is saturation. For instance, consider a 2 DOF system with a quadratic nonlinearity, and internal resonance, $\omega_2 \sim 2\omega_1$ where the system is excited with $\Omega \sim \omega_2$ (Ω is the excitation frequency). The second mode is dominant up to a certain value of excitation amplitude, known as critical amplitude. Beyond the critical excitation amplitude, the second mode becomes saturated and the excessive energy excites the first natural mode. The value of critical amplitude depends on system damping [13].

Ref. [24] mentions a few practical examples where internal resonances have led a mechanical system to failure. These examples encouraged Nayfeh *et al.* to investigate the response of a 3DOF nonlinear system with quadratic nonlinearities and internal resonances $\omega_3 \sim 2\omega_2$ and $\omega_2 \sim 2\omega_1$. The response of the system to a primary excitation $\Omega = \omega_3$ is examined. As the system is excited starting with low excitation amplitudes, the response consists of only the third mode (excited mode) and the amplitude of response increases linearly with the amplitude of excitation up to a critical amplitude. With further increasing the excitation amplitude, Hopf bifurcation occurs and the second (lower) mode is excited in addition to the third mode. As the excitation amplitude further increases, a secondary Hopf bifurcation occurs and the result is an unstable response with all the three modes present.

Yamamoto and Ishida [12] explain that internal resonance may happen in systems where the forward whirl and backward whirl natural frequencies are equal in magnitude and related to each other by antisymmetric nonlinearities. For instance, in Jeffcott rotors [25], the forward and backward natural frequencies are equal in magnitude (absolute value); hence these rotors are susceptible to internal resonance.

The nonlinear Jeffcott rotor model is used to study theoretically and experimentally the effect of internal resonance on nonlinear system response at the critical speed, as well as two and three times the fundamental critical speed [26]. Note that in Jeffcott rotors the gyroscopic effects are negligible, so natural frequencies are speed independent and the magnitude of forward and backward natural frequencies coincide (1:-1 internal resonance may occur).

When exciting the nonlinear Jeffcott rotor system with the fundamental critical speed, the magnitude of the forward, ω_f, and backward, ω_b, synchronous frequencies coincide with the combined resonance of $0.5(\omega_f - \omega_b)$. In a case where the system is excited with twice the major critical speed, the magnitude of the forward subsynchronous $0.5(2\omega_f)$ and backward subsynchronous $0.5(2\omega_b)$ frequencies coincide with combined resonance $0.5(2\omega_f - 2\omega_b)$. Also, in a case where the system is excited with three times the major critical speed, the magnitude of the forward subsynchronous $1/3(3\omega_f)$ and backward subsynchronous $1/3(3\omega_b)$ frequencies coincide with combined

resonances ($2\omega_f$-ω_b) and (ω_f-$2\omega_b$). In all cases due to occurrence of internal resonance, the response of the system is nearly periodic due to Hopf bifurcation and the nonlinearities bend the resonance curves. As gyroscopic effects are introduced to the system, the forward and backward synchronous speeds diverge from each other. Therefore, internal resonance does not occur and responses appear similar to cases with solitary resonance (no internal resonance) [26].

A combined resonance $\Omega= 2\omega_1 +\omega_2$ occurs in systems with cubic nonlinearity [13] such as Duffing-type systems. However, Shaw and Shaw [27] demonstrate that in presence of internal damping, the nonlinear behavior of an unbalanced rotating shaft is far more complicated than a Duffing-type response. In a rotating shaft with internal damping they observe quasi-periodic motion, which results from amplitude modulations of the whirl motion.

Yamamoto and Yasuda [28] obtain the forced response of a 2DOF system with both quadratic and cubic nonlinearities and internal resonance 1:2 ($\omega_2 \sim 2\omega_1$). In addition, viscous damping is present. They observe that at small excitation frequencies, Ω (away from resonance) the system behaves similar to a case without internal resonance. However, as Ω increases and approaches to the first natural frequency, ω_1, the amplitude of second natural mode increases in addition to the first natural mode. At this excitation frequency both the first and second harmonics are present. As Ω increases beyond the first natural frequency, a jump occurs in the response. With further increase of Ω there is a back and forth exchange of energy between the first and second natural modes. This region is called quasi-periodic region. As Ω increases, the response becomes completely periodic and both first and second harmonics are observed. With further increasing Ω, the amplitude of the second natural mode becomes very small, and the behavior of the system is again similar to a case without internal resonance. Yamamoto and Yasuda [28] also observe that damping ratio greatly affects the response in the quasi-periodic region. As the damping ratio increases, the back and forth energy exchanges between the first and second modes cease, and the response becomes fully periodic and stable.

Asmis and Tso [29] investigate the effect of internal resonance on combined resonance response in a 2 DOF system with a cubic nonlinearity. The system has a combined resonance, $\Omega \sim \omega_1 + \omega_2$ and an internal resonance, $\omega_1 \sim \omega_2$. They use the concept of internal and external detuning as a way to quantify how well the internal and combined resonance relations are satisfied by the actual values of natural frequencies. The larger the internal detuning, the farther are the first and second natural frequencies from each other. Also, the larger the external detuning, the less accurate is the combined resonance approximation $\Omega \sim \omega_1 + \omega_2$. Interestingly, Asmis and Tso report that for a certain range of external detuning, the system exhibits amplitude modulated quasi-periodic response. In other words, the system displays beating and energy is exchanged between the first and second natural modes. As the internal detuning increases the range of modulated quasi-periodic response increases. However, the amplitude of beating decreases and the response becomes more periodic. For cases where internal detuning is zero ($\omega_1 = \omega_2$), internal resonance causes larger steady state response amplitude and tends to reinforce the combined resonance.

In another study, Mook $et\ al.$ [30] investigate the effect of internal resonance on the response of a system of differential equations with cubic and quadratic nonlinearities. The system has a combined resonance of $\Omega = \omega_1 + \omega_2$, where Ω is the excitation frequency, and ω_1 and ω_2 are the first and second natural frequencies, respectively. For a case with no internal resonance, the response of the system consists of a trivial solution where the excited frequency is near the excitation frequency, Ω. There is also a non-trivial solution where the responses occur near ω_1 and ω_2 due to combined resonance. For a case with internal resonance $\omega_1 \sim \omega_2$ the trivial solution is identical to the one for without internal resonance. However, the nontrivial solution does not reach steady state as a result of back and forth exchange of energy between the first and second natural modes. In fact, the response is quasi-periodic. Mook $et\ al.$ [30] also report that internal resonance decreases the amplitude of response due to combined resonance. However, this conclusion is the exact opposite of what Asmis and Tso report in Ref. [29] . The discrepancy in results may be due to the different types of nonlinearity in two cases.

Recently, Schweizer and Sievert [31] study bifurcations in measured turbocharger shaft responses during rotor acceleration (from 0 krpm-160 krpm). The TC rotor is supported on FRBs. Shaft displacements, along horizontal and vertical directions, are measured (using eddy current sensors) at the compressor end. Measurements are at two oil supply pressures (1.5 bar and 3 bar) and oil inlet temperatures (75°C and 90°C). In addition, the authors increase the imbalance amount (by adding 0.25gr.mm and 0.57gr.mm) at the compressor wheel, and study its effect on the nonlinear response. The measured waterfalls of shaft motion display a jump from a 1st subsynchronous whirl frequency to a 2nd (higher), and sometimes to a 3rd (lower) subsynchronous frequencies. The authors relate the 1st and 2nd subsynchronous frequencies to the inner film whirl/whip exciting the conical and cylindrical modes, respectively. The 3rd subsynchronous frequency is attributed to the outer film instability exciting the conical mode of the RBS.

According to the measured waterfalls of TC shaft motion, $\Omega_{bifurcation}$ (the rotor speed at which the frequency jump occurs) is more sensitive to oil inlet pressure than it is to oil inlet temperature. At 75°C oil supply temperature, increasing the oil inlet pressure (from 1.5 bar to 3 bar) delays the $\Omega_{bifurcation}$ (from ~45 krpm to 60 krpm). However, a higher oil inlet temperature results in the disappearance of the 2nd subsynchronous motion at a shaft speed below 120 krpm (which persists up to 160 krpm with low oil inlet temperature). The sensitivity of $\Omega_{bifurcation}$ to oil supply pressure is not in agreement with the earlier observations of HTT engineers. The waterfalls of casing accelerations provided by HTT correspond to various inlet temperatures, but not various inlet pressures.

Interestingly, increasing the imbalance amount by adding 0.25gr.mm, results in the disappearance of the 2nd subsynchronous whirl frequency at approximately 130 krpm. However, the $\Omega_{bifurcation}$ remains unchanged. Further increase in the imbalance amount (by adding 0.57gr.mm) delays the onset speed of a 2nd whirl frequency to a TC speed of 80 krpm. In addition, the 1st whirl frequency disappears at a lower shaft speed (~45 krpm). However, between 60 krpm and 80 krpm, a 0.5 whirl frequency motion

appears to be dominant. Amplitudes of motion in the horizontal and vertical directions are similar, indicating of FRB operation at low journal eccentricities.

In addition to the shaft response measurements, Schweizer and Sievert [31] also find the bifurcations in predicted TC shaft responses using a flexible rotor model supported on simple FRBs. The frequency spectrum of the predicted results shows the 1st whirl frequency bifurcating into the 2nd whirl frequency; however, the figures do not show the speed at which the bifurcation occurs. Only one case of simulation is presented, with few details given as per either the predicted results, or the bearing model, or the TC rotor finite element model.

Based on the literature review, in order to analyze the jump phenomenon from the first to the second subsynchronous frequency, one must pay special attention to the fluid film bearing nonlinearities and operating conditions under which internal and combined resonances occur.

Objective

According to the TC manufacturer, the frequency jump phenomenon from a first subsynchronous whirl frequency to a higher whirl frequency, results in increased level of noise generation in automotive turbocharger units. Hence, the objective of this research is to investigate some of the bearing parameters and rotor characteristics affecting the rotor-bearing system performance and the frequency jump phenomenon, as well as the severity and persistence of subsynchronous whirl motions. This study will assist turbocharger manufacturers in achieving a quantifiable understanding of the frequency jump phenomenon and will aid to the optimization of turbocharger design, achieving lower noise generation.

Prior Work at TAMU

Turbocharger rotordynamic performance assessment involves rigorous testing which is both costly and time consuming. Significant time and costs can be saved by replacing the shop assessment with a proven predictive model, experimentally benchmarked. The development and refinement of such model are the goal of a research project, nearly a decade long, at Texas A&M University [1-6], [33-35].

Holt et al., [5] measure center housing acceleration of a turbocharger supported on FRBs. The authors assess the effect of lubricant supply temperature and pressure on TC housing acceleration response. The waterfalls of center housing acceleration show motions with two typical subsynchronous frequencies, ranging between 40% and 70% of shaft speed. Tests show that lubricant supply pressure delays the onset speed of the second subsynchronous whirl motions. However, lubricant supply temperature shows negligible effect on the onset speed of subsynchronous whirl motions. Further, Holt et al. [5] validate a TC FE rotor model against measured free-free natural modes, and obtain TC shaft response predictions at the compressor end. Predicted waterfalls of shaft motion display two subsynchronous frequencies at ½ ring speed and ½(rotor + ring) speed, denoting instability of the outer and inner films, respectively. Most importantly, waterfalls of TC response predictions with rotor imbalance demonstrate a more stable operation at high shaft speeds compared to the case with a TC rotor perfectly balanced. The measured center housing accelerations [5] , in which the TC rotor includes an unknown imbalance, also show the absence of subsynchronous whirl motion at high shaft speeds.

San Andrés and Kerth [4] detail a thermo-hydrodynamic (THD) model and compare predicted bearing performance parameters against measurements on a TC rotor supported on FRBs. Measured ring speed, lubricant exit temperature, and power loss agree well with predictions. The floating ring rotational speed is proportional to the inner film viscosity and outer film clearance. Predictions show that with increasing shaft speed, the inner film viscosity and the outer film clearance decrease due to thermal effects. Therefore, the ring speed decreases with shaft speed. Waterfalls of measured and predicted TC shaft motions show the presence of two subsynchronous whirl motions due to instability of the inner and outer films. However, predictions typically overestimate the amplitude of subsynchronous whirl shaft motions. The discrepancy is attributed to an inaccurate knowledge of the rotor imbalance.

Kerth [32] measures and predicts the shaft motion response of a TC supported on FRBs. Kerth also assesses the effect of compressor aerodynamic load on the measured TC rotor response by rotating (statically) the compressor housing (cut water) to redirect

the aerodynamic load. The TC rotordynamic response appears insensitive to compressor housing orientation. In addition, Kerth obtains test data and predictions of TC shaft response at various oil supply pressures. The measurements show a reduction in response amplitude with increases in oil supply pressure. However, predictions do not display such reduction in response amplitude. Therefore, San Andrés and co-workers continue to improve the fluid film bearing THD flow model (XLFEMSFRB™ [7]).

Rivadeneira [33] accounts for hydrostatic (side) loads acting on the FRBs due to oil supply pressurization and obtains TC rotor response predictions for various oil inlet temperatures and oil inlet pressures. The shaft total motion response does not show great sensitivity to the variations of oil inlet temperature and pressure. However, accounting for the hydrostatic side loads significantly improves the agreement between the predicted and measured shaft responses.

Maruyama [3] continues the refinement to the developed TC rotor-bearing motion predictive tool by including the effect of engine-induced base motion excitations. Fluid film bearings transmit the base excitation from the center housing to the TC rotor. A TC manufacturer provides center housing and compressor housing accelerations measured in a commercial vehicle TC whose inlet manifold is attached to a four-cylinder engine. Test data reveals that center housing and compressor housing do not move as a rigid body. TC housing accelerations show prominent amplitudes of acceleration at two and four orders of engine fundamental frequency. The center housing acceleration is input into the rotordynamics code (base excitation) as components of a Fourier time series. Nonlinear response predictions agree well with test data, demonstrating a rich subsynchronous behavior. However, nonlinear predictions, excluding the effect of base excitation, show little subsynchronous motions, indicating of the importance of base excitation effects in TC nonlinear response predictions.

CHAPTER IV

OVERVIEW OF THERMO-HYDRODYNAMIC MODEL FOR SFRB

FORCED RESPONSE AND FINITE ELEMENT MODEL FOR

TURBOCHARGER STRUCTURE

Fluid film bearing parameters play a key role in TC rotordynamic performance. Bearing parameters such as operating clearances, fluid film viscosity, and inlet film pressure vary with the TC shaft rotational speed. Further, these parameters are functions of shaft, ring, and casing temperatures as well as the lubricant supply pressure and temperature. San Andrés and Kerth [4] develop a FE thermo-hydrodynamic fluid film bearing model, which predicts the (S)FRB static and dynamic performance characteristics (i.e. operating bearing clearances, effective film viscosity, fluid film temperature rise, ring and journal eccentricities, power losses, film flow rates, and dynamic fluid film force coefficients).

The THD model accounts for the fluid film bearing clearance variations due to shaft and ring thermal growth. The shaft temperatures at the turbine and compressor bearing locations are estimated using an empirical temperature defect ratio [shaft temperature - lubricant inlet temperature]/ [turbine wheel temperature - lubricant inlet temperature]. Measurements show the temperature defect ratio at the turbine bearing and the compressor bearing are 0.16 and 0.13, respectively, when the turbine wheel temperature is ~ 700°C [34].

TC units often use non-Newtonian lubricants. Therefore, the oil viscosity decreases with shear rate, in addition to temperature. The available fluid film bearing model incorporates Cross equation [35] to account for shear thinning effects in the lubricant viscosity.

Lubricant pressure drop into the inner and outer films may occur for various reasons and must be taken into account. For instance, experiments show the supply pressure into the outer film feed plenum is lower than the feed pressure recorded at the inlet port in the center housing. In the fluid film bearing model, an empirical pressure loss factor quantifies this loss [3]. In addition, the rotation of the ring (in FRB) and shaft

cause a pressure drop into the inner film due to centrifugal flow effects. The bearing model incorporates a centrifugal pressure loss model developed in Ref. [36].

The turbocharger CHRA (Center Housing Rotating Assembly) in this study is similar to the one shown in Figure 1 (Chapter I). The TC rotor is supported on a SFRB. Figure 7 (not to scale) enlarges the SFRB and the center housing. The SFRB is a long and hollow cylinder with the compressor side bearing and turbine side bearing at its ends. Lubricant is supplied through the TC center housing into the outer film of both bearings, and from there to the respective inner films through four equidistant holes in both sides (compressor and turbine ends) of the SFRB. Note the center housing incorporates a ½ moon groove on the turbine bearing side; hence, creating a larger hydrostatic side load factor on the turbine bearing than the one on the compressor bearing. Ref [33] provides details on predicting side load factors.

Figure 8 depicts the cross section schematic view of the TC analyzed, excluding the thrust collar and the ring spacers. The inner and outer film clearances are greatly exaggerated. The figure is not to scale and intends to qualitatively show the bearing inner and outer fluid films. The yellow sections represent regions filled with lubricant. For simplicity, Fig. 8 shows only the upper half section of the TC rotor-bearing system.
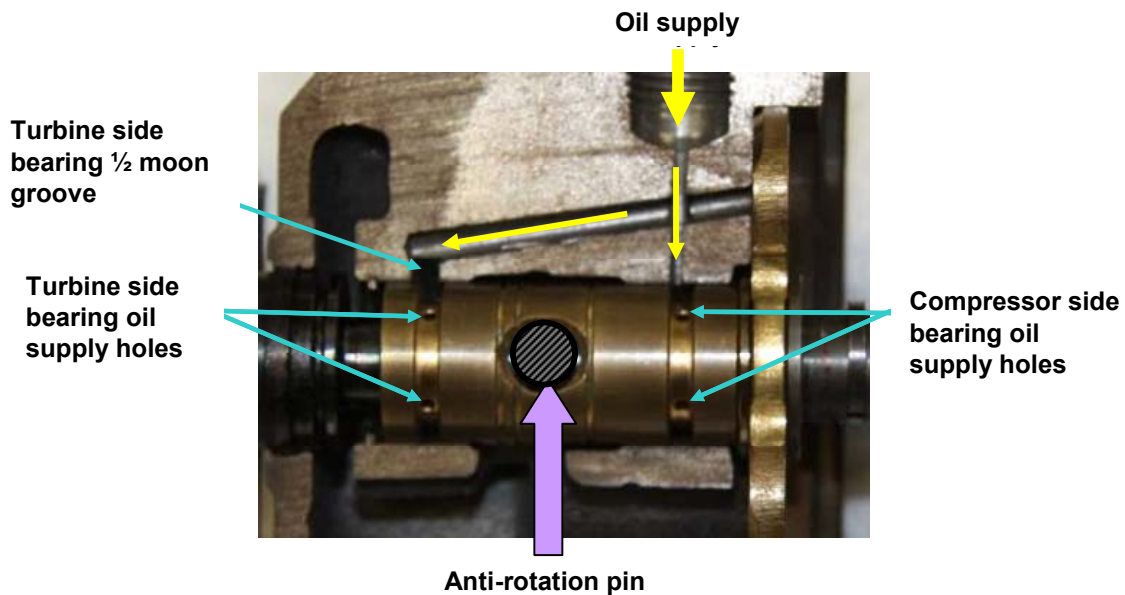
Figure 7: Photograph of typical SFRB and center housing with oil feed lines
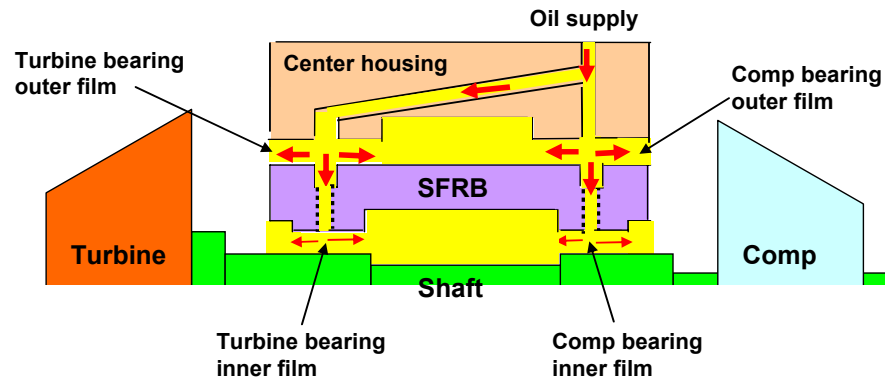
Figure 8: Schematic cross section view of TC rotor and SFRB (not to scale, films enlarged)

Figure 9 depicts the TC rotor finite element model, consisting of 43 finite elements, and the SFRB modeled with 13 elements. A blue arrow shows the rotor-bearing system (RBS) center of gravity. A spring connecting the shaft to the SFRB models the inner film, and a spring connecting the SFRB to the ground represents the outer film. The shaft and SFRB are made of steel and brass, respectively. The turbine and compressor wheels are modeled as low density elements with added lumped mass and mass moments of inertia (polar and transverse). The TC manufacturer provides a four plane imbalance mass distribution. Appendix A lists the TC and SFRB physical properties.

The fluid film bearing model is integrated with the finite element rotordynamics computational model for numerical prediction of the TC linear and nonlinear (time transient) forced response. The FE rotor model uses Timoshenko's beam theory to model the TC shaft and the ring. Each node in a structural finite element has four degrees of freedom (two rotations and two translations). The number of degrees of freedom for the RBS is reduced using component mode synthesis [37]. The nonlinear rotordynamic analysis applies the instantaneous bearing reaction forces (dependent on operating conditions; i.e., actual clearances, ring speed, films viscosity, journal and ring displacements and velocities, and lubricant supply pressure) into the equations of motion (EOM). The EOM are integrated using a Gear-Stiff method [8]. Appendix D provides the equations of motion for the RBS.
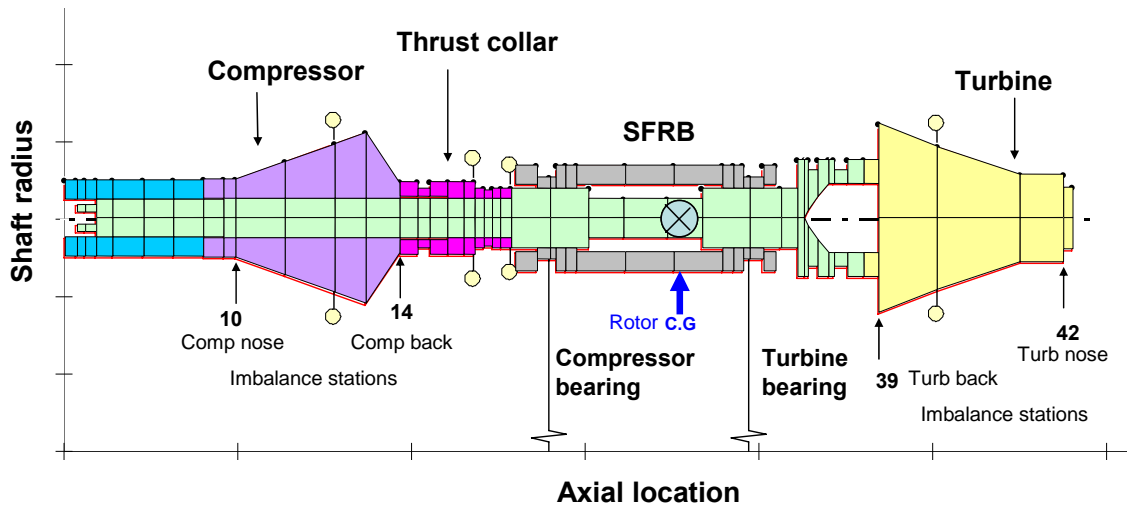
Figure 9: TC finite element rotor model

Predicted SFRB Performance Characteristics

This section details the SFRB static load performance characteristics predicted by the THD flow model XLFEMSFRB™ [7]. Note in this analysis, the bearing reaction force is always equal to the rotor static load applied on the bearing. The turbocharger shaft speed varies from 30 krpm to 240 krpm. Table A.5 (Appendix A) lists the nominal operating conditions.

In the following, performance parameters are shown in dimensionless form as ratios with respect to inlet conditions, unless otherwise stated. Figure 10 depicts the inner and outer oil films exit temperatures for the compressor and turbine bearings. The exit temperatures are higher at the turbine bearing location due to heat transfer from the hotter turbine wheel. In addition, in both turbine and compressor bearings, the inner oil film has a higher temperature (compared to the outer film) due to shaft rotation shear effects. Recall that the floating ring is pinned, i.e., it does not rotate.

Figure 11 depicts the inner oil film power loss (relative to the maximum power loss at the highest shaft speed) for the compressor and turbine bearings. Power dissipation is a quadratic function of shaft speed. As shaft speed increases, the shear dissipation in oil films increases; therefore power dissipation increases.

Figure 12 shows, for the compressor and turbine bearings, the effective inner and outer oil film viscosities versus shaft speed. The outer oil film, which acts as a squeeze

film damper has a lower film temperature and a higher viscosity. The inner film reduced viscosity is due to its higher temperature as well as more lubricant shear thinning effects as a result of shaft rotation.

Figure 13 depicts the operating (inner and outer film) clearances (relative to the respective cold clearances) for the turbine and compressor bearings. The changes in operating clearances between the lowest and highest shaft speeds are approximately 7% for both the inner and outer films. As the shaft speed increases, the inner film clearance increases and the outer film clearance decreases, indicating of ring thermal expansion.

Figure 15 shows the journal relative to ring eccentricity ratio for the compressor and turbine bearings. Note the maximum value of journal eccentricity relative to ring (at lowest shaft speed) for the turbine and compressor bearings are around 7% and 3% of the inner film clearance, respectively. In other words, the journal operates at centered position relative to the ring.
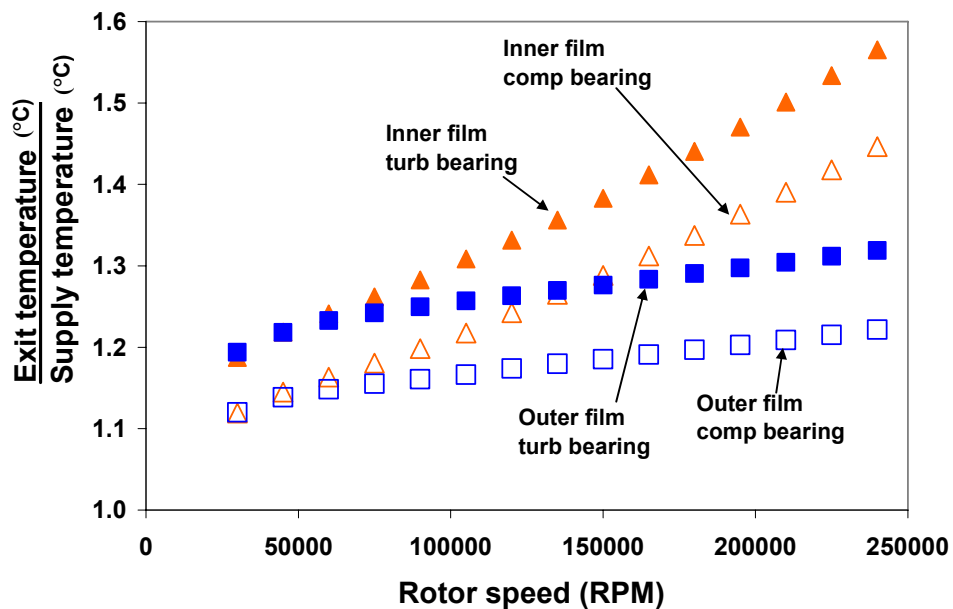
Figure 10: Predicted (inner and outer) oil films exit temperature versus rotor speed in TC compressor and turbine bearings
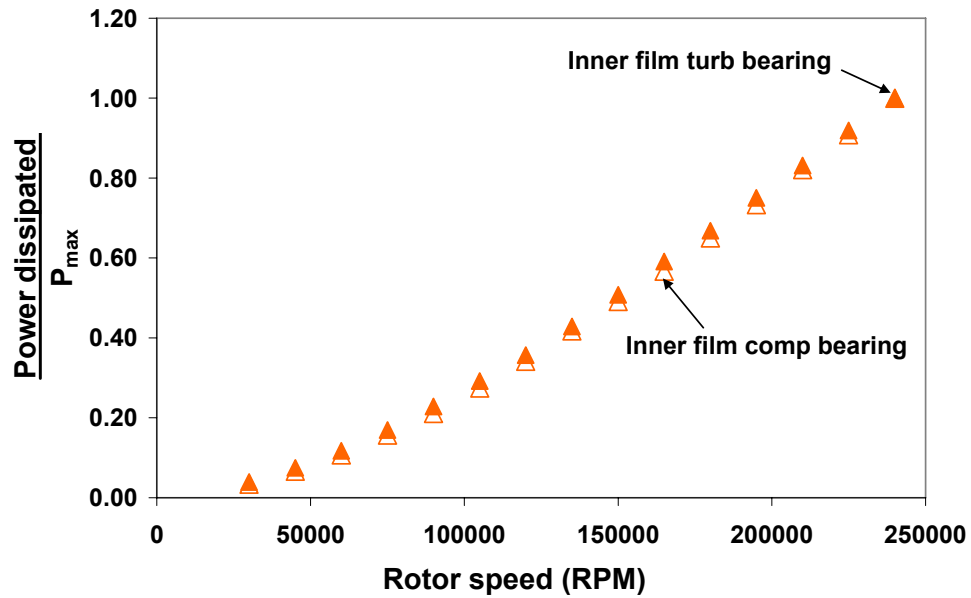
Figure 11: Predicted normalized power loss at the inner film of the compressor and turbine bearings versus rotor speed

Figure 12: Predicted effective (inner and outer) oil film viscosity versus rotor speed for the compressor and turbine bearings
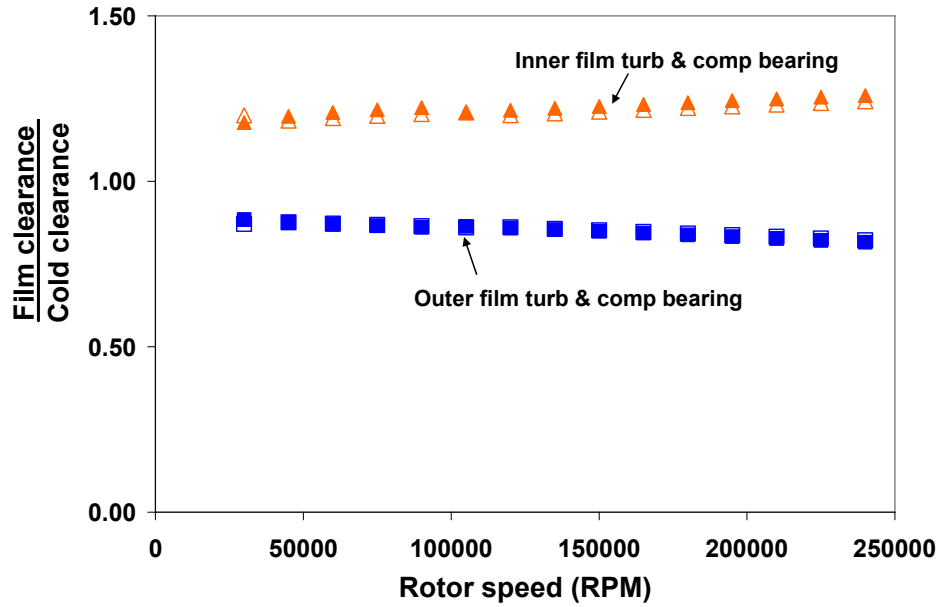
Figure 13: Predicted (inner and outer) film clearance ratios versus rotor speed for the compressor and turbine bearings
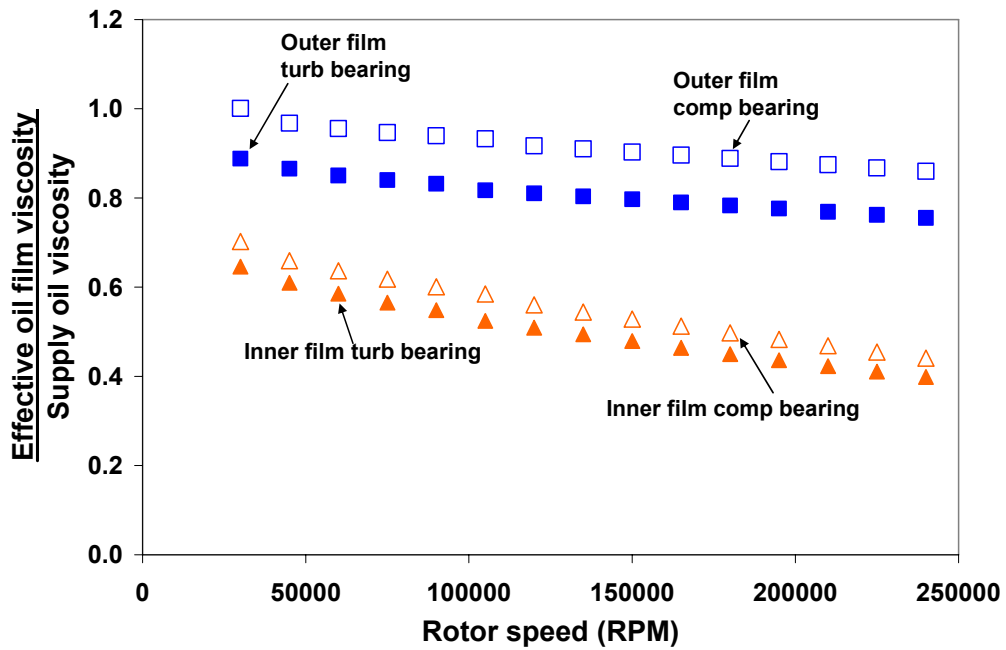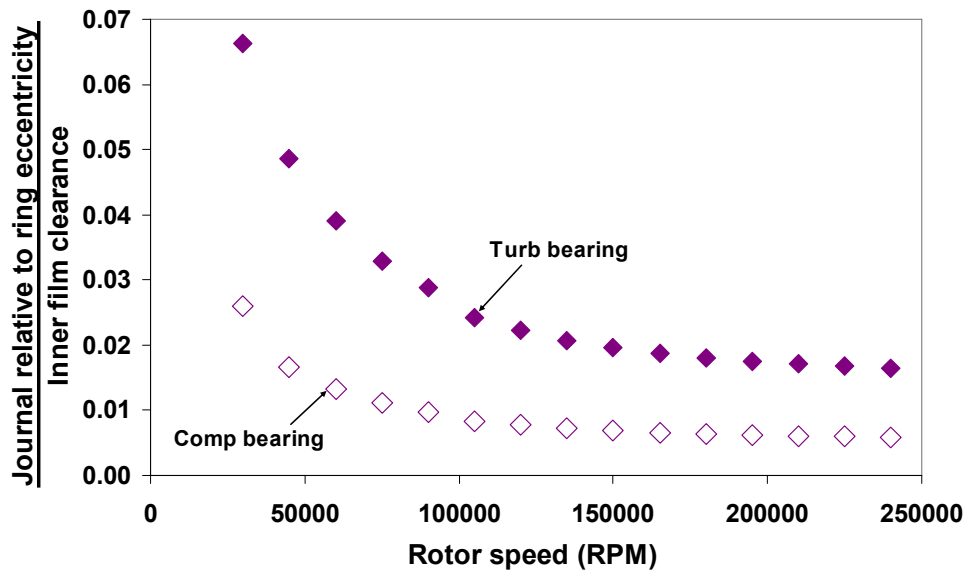

Figure 14: Predicted journal eccentricity relative to ring versus rotor speed for the compressor and turbine bearings

CHAPTER V

LINEAR TURBOCHARGER RESPONSE PREDICTIONS

Linear Eigenvalue analysis uses the linearized bearing force coefficients, obtained from the THD flow model [7], in predicting the rotor-bearing system (RBS) natural frequencies. Figure 15 shows a schematic view of the coordinate system for. Figure 16 depicts the predicted (non-dimensional) SFRB inner film stiffnesses as well as the inner and outer films damping coefficients for the compressor and turbine bearings. The graphs on the left and right sides correspond to the compressor and turbine bearings, respectively. The non-dimensional stiffness ($\bar{k}$) and damping force ($\bar{c}$) coefficients are defined using [39]:

$$\bar{k} = \frac{K}{K^*}, \quad K^* = \mu \frac{D}{2}\left(\frac{L}{C_l}\right)^3 \Omega$$

$$\bar{c} = \frac{C}{C^*}, \quad C^* = \mu \frac{D}{2}\left(\frac{L}{C_l}\right)^3$$

where K and C are the physical force coefficients, μ is the lubricant viscosity at the supply temperature and Ω is the shaft rotational speed. For the inner film force coefficients, D, L, and C_l represent the nominal values of shaft diameter, bearing inner film length, and (cold) inner film clearance, respectively. For the outer film coefficients, D, L and C_l represent the nominal values of ring (outer) radius, bearing outer film length, and (cold) outer film clearance, respectively. Appendix A details the shaft and ring dimensions.

As a note, hydrostatic side loads are applied only on the bearing outer film. For the inner film, only the weight of the shaft is considered, so the journal operates close to the center of the ring. Chapter VI further explains the reason for applying hydrostatic loads only to the outer film.

Figures 16 (a) and (b) show that for compressor and turbine bearings, the inner film direct stiffness coefficients are nil due to the low static load. Also, the cross-coupled stiffness coefficients, (k_{xy}- k_{yx}> 0) add energy to the whirl orbits. Note k_{xy} is

approximately equal to $-k_{yx}$. As a reminder, $(k_{xy} = -k_{yx})$ is a typical driver of instability in a RBS.

The inner film damping coefficients in Figures 16 (c) and (d) decrease with shaft speed due to the journal displacement closer towards the center of the ring. The outer film direct damping coefficients decrease with shaft speed because the ring eccentricity decreases (ring moves towards the center of the bearing). The outer film cross coupled damping coefficients equal zero, and are not shown in Figures 16 (e) and (f).
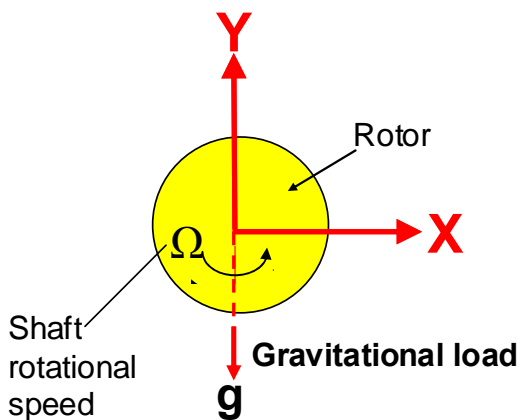

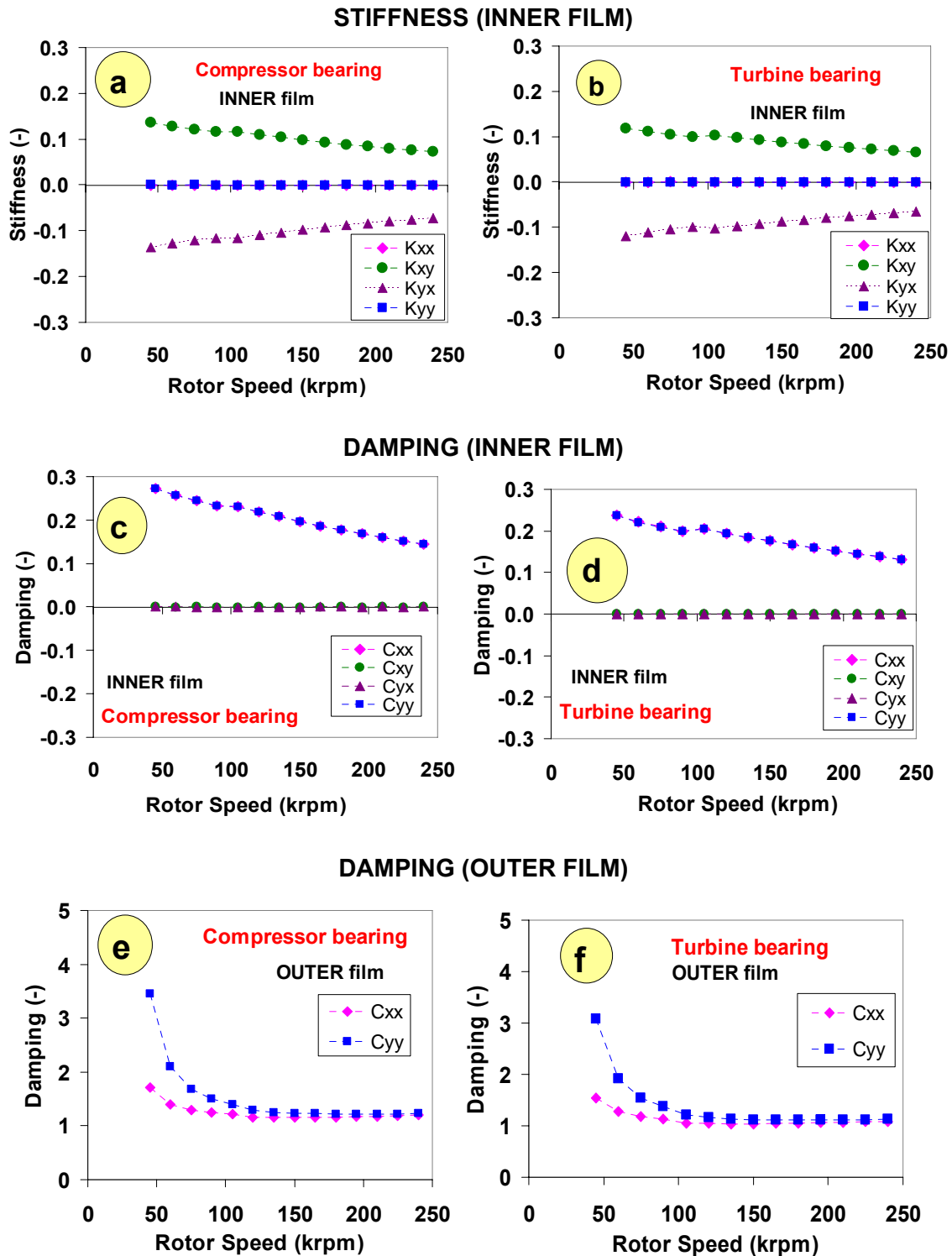**Figure 15: Schematic view of rotor coordinate system for analysis of rotor motions**

Figure 16: Predicted SFRB normalized force coefficients; (LEFT) compressor bearing, (RIGHT) turbine bearing; (a) and (b) inner film stiffness $\bar{k}$; (c) and (d) inner film damping $\bar{c_i}$; (e) and (f) outer film damping coefficients $\bar{c_o}$.

Figure 17 (top) depicts the damped natural frequency map of the TC analyzed, with mode shapes at 95 krpm shaft speed shown. The compressor and turbine ends of the TC are marked on the mode shapes with letters 'C' and 'T', respectively. The black dashed line denotes the shaft synchronous speed. The bottom figure depicts the corresponding damping ratios versus shaft speed. The 1st natural frequency corresponds to a conical rigid body mode, frequency ranging from 8Hz to 230Hz as rotor speed increases. This mode is well-damped (at 95 krpm shaft speed, damping ratio ξ=0.68). The 2nd natural frequency corresponds to a conical mode with the SFRB whirling in a conical mode as well. This mode is always unstable (at 95 krpm shaft speed, damping ratio ξ= -0.05). The 3rd natural frequency corresponds to a rotor cylindrical bending mode with the SFRB whirling in a cylindrical mode. This mode is also always unstable (at 95 krpm shaft speed, ξ= -0.09). Figure 17 (bottom) shows negative damping ratios for the 2nd and the 3rd natural frequencies, which indicates unstable modes. The 4th natural frequency corresponds to a cylindrical bending mode (at 95 krpm shaft speed, ξ=0.24), and the highest natural frequency within the TC shaft operating speed range is a well-damped first elastic mode ranging from 1,000 Hz to 2,300 Hz (at 95 krpm shaft speed, ξ=0.30).

Figure 18 depicts the damped natural frequency map for the unstable modes. The ($\triangle$) and ($\blacklozenge$) symbols represent the unstable 2nd and 3rd natural modes, respectively. Note at 140 krpm shaft speed, the 2nd natural frequency represents a conical mode with SFRB whirling in a conical mode. As the shaft speed increases to 145 krpm, the shaft still whirls in a conical mode, but the SFRB whirls in a cylindrical mode. Eventually, as the shaft speed increases, the 2nd natural frequency represents a cylindrical bending mode with the SFRB whirling in a cylindrical mode. A similar phenomenon occurs at the 3rd natural frequency, which represents a cylindrical bending mode at low shaft speeds. As the rotor speed increases to 145 krpm, the shaft still whirls in a cylindrical bending mode, whereas the ring starts whirling in a conical mode. As the rotor speed further increases, the 3rd mode represents a conical mode with the SFRB in a conical mode. One can attribute this transition of modes (between conical and cylindrical) to the

closely spaced natural frequencies. In fact, it seems the ring motion encourages the rotor whirl transition from one mode to the other.
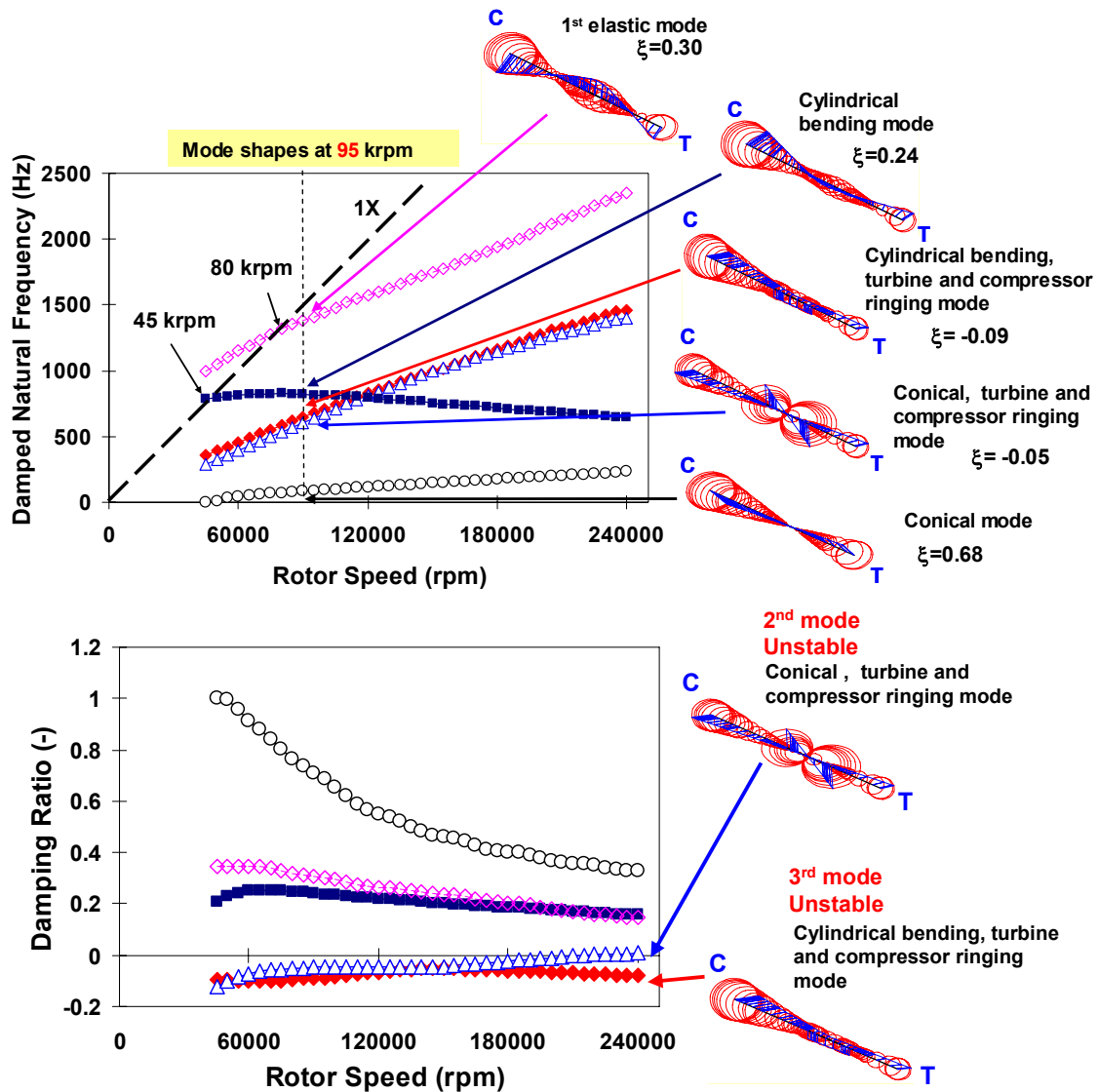
Figure 17: (TOP) TC damped natural frequency map and mode shapes at rotor speed of 95 krpm, (BOTTOM) damping ratio versus rotor speed
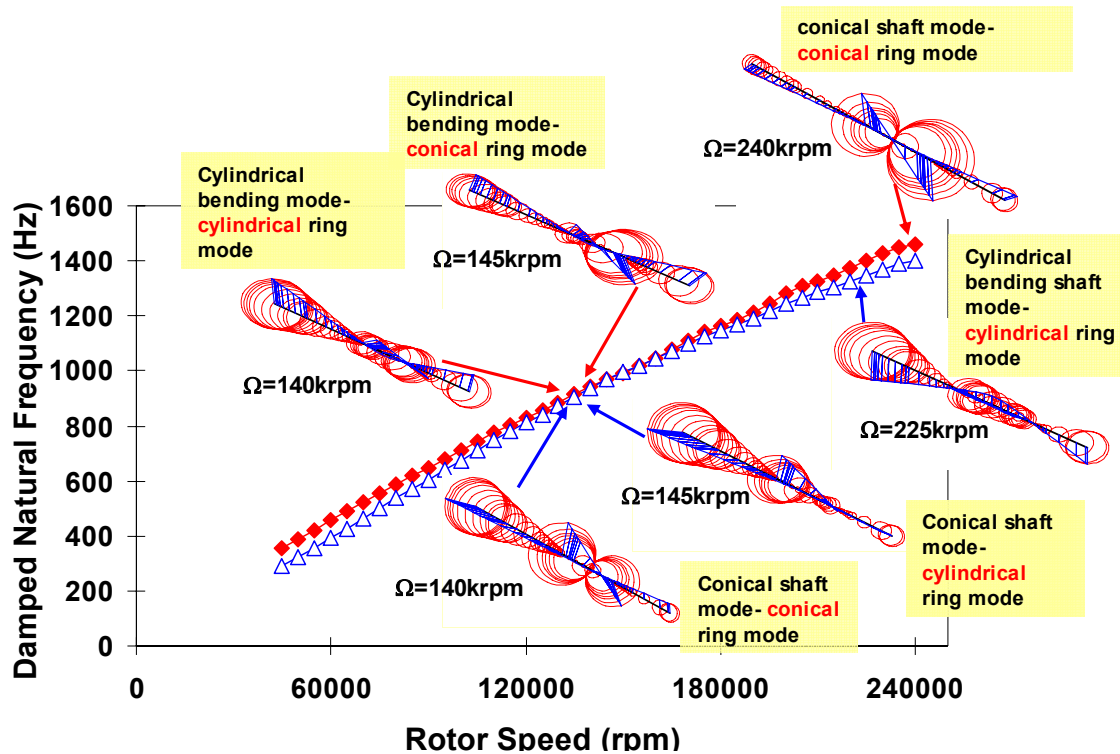
Figure 18: TC damped natural frequency map and mode shapes for the unstable modes

Figure 19 depicts the predicted amplitude of imbalance synchronous rotor response (at the compressor end) obtained from the linear analysis (blue line) and from the nonlinear rotor speed transient analysis (▲). In addition, the synchronous responses from the nonlinear time transient analysis (obtained at a fixed speed) are shown at the highest shaft speeds (☐).   In the transient rotor speed analysis the shaft accelerates with a 500 Hz/s speed ramp rate[†]. The amplitudes of response are normalized with respect to the maximum physical displacement at the compressor end (listed in Appendix A).

The synchronous response from the linear rotordynamics analysis in Fig. 19 shows peak amplitudes at 45 krpm and at 110 krpm. According to the damped natural

---

[†] In the FFT analysis of the time data, data is broken into segments of 512 points. The sampling time Δt = 0.1ms, and the time span over each FFT is approximately 52ms. The shaft speed variation over each FFT segment is approximately 1,500 rpm (~26Hz). The sampling frequency in FFT analysis is rather large (~20Hz). Since the FFT sampling frequency (~20Hz) is close to the speed variation over each FFT (~26Hz), even though the rotor speed changes, the FFT analysis of synchronous motion captures one speed per FFT segment. Therefore, the speed transient synchronous response amplitude is similar to the ones from the nonlinear fixed rotor speed analysis.

frequency map (Fig. 17), at ~ 45 krpm rotor speed, the cylindrical bending mode (ξ=0.20) coincides with the rotor synchronous speed. A simple estimation using the half power frequency law [38] shows the corresponding damping ratio at the critical speed in Fig. 19 is ξ~0.22 which is close to the one for cylindrical bending mode at the critical speed (ξ=0.20). Hence, the peak response in Fig. 19 is due to rotor speed exciting the cylindrical bending mode. The natural frequency map also shows at approximately 80 krpm the synchronous speed coincides with the first elastic mode. Results from the linear rotordynamic analysis in Fig. 19 shows a well-damped (ξ=0.33) peak response at around 110 krpm, which may be due to the rotor speed exciting the first elastic mode.

Note the discrepancies between the synchronous responses from the linear rotordynamic analysis and the nonlinear (at fixed shaft speed and speed transient) analyses. The linearized bearing force coefficients are obtained using small perturbations of the rotor about a static equilibrium position. However, nonlinear analysis shows large rotor and ring motions (see Chapter VI for details on nonlinear analysis), which explains the discrepancies between the linear and nonlinear predictions.
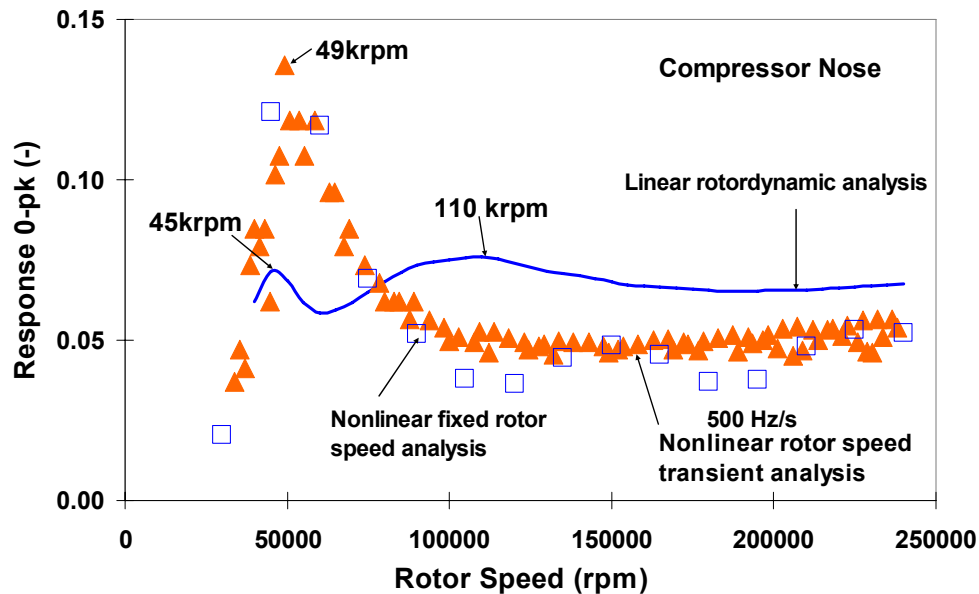
Figure 19: Predicted amplitude of TC synchronous response at compressor end (vertical direction). Results from linear rotordynamics analysis, nonlinear analysis at fixed rotor speed, and nonlinear analysis with varying rotor speed.

CHAPTER VI

NONLINEAR ROTORDYNAMIC PREDICTIONS

This section contains predictions of the nonlinear time transient, rotor speed transient, TC rotor response. Automotive TC shaft operation normally involves a varying shaft speed. In this analysis the shaft accelerates from 30 krpm to 240 krpm and decelerates down to 30 krpm with 500Hz/s speed ramp rate, unless otherwise stated. The time duration is 7 seconds for the shaft to accelerate from the lowest to the highest shaft speed. In the numerical integration, the sampling rate equals 10,000 samples/sec (Δt = 0.1ms). Table 1 lists the parameters used in the nonlinear speed transient numerical analysis.

The results are best understood in the frequency domain; hence, the predicted responses are converted from the time domain into the frequency domain using the discrete Fast Fourier Transform (FFT). The frequency contents of the predictions are obtained by dividing the whole time domain data into segments of 2^{11} (2048) points (time span of each segment ~102ms) and applying the FFT on each time segment. The maximum shaft speed is 240 krpm (4,000Hz), hence the maximum frequency and Δf in the FFTs are 5,000Hz and 4.88 Hz, respectively.
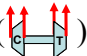
Table 1. Parameters for speed transient, time transient. Shaft speed=30-240krpm, sampling time=100μs

Ramp Rate	Δf	Time Segment Duration	Time Steps per Segment	Total Integration Time	Number of Time Segments	Total # of Time Steps	Total ‡CPU Time for Speed Transient
[Hz/s]	[Hz]	[s]	-	[s]	-		[hr]
±500	4.88	0.5	5,000	7.0	14	70,000	~9.0

‡ The processor and other specifications of the computer used in this analysis are Intel^R Core^TM2 CPU 4300@ 1.80GHz, 1.79 GHz, 2.00GB of RAM

In order to determine the effect of various operating conditions, and bearing and rotor characteristics, on bifurcations and frequency jump phenomenon, only one parameter is varied at a time. A baseline case is below, showing the typical results for the corresponding operating conditions[§].

Baseline Case

      Appendix A lists the operating conditions as well as the rotor and bearing specifications for the baseline case. The rotor speed ramp rate is 500Hz/s, and a 4-plane static imbalance distribution is used ( ).

      The predicted response amplitudes in the following sections are presented in dimensionless form with respect to the maximum physical displacement at the compressor end, which is listed in Appendix A.

      Figures 20 and 21 depict the predicted waterfalls of TC shaft motion at the compressor end, along the horizontal and vertical directions, respectively. The synchronous response is labeled with '1X'. Figure 21 (bottom) shows the contour map of shaft motions in the vertical direction and the synchronous line is marked with yellow arrows. In the waterfall plots, subsynchronous whirl frequencies are marked with 'ω_1' and 'ω_2', respectively.

      Both waterfalls show motions with a subsynchronous whirl frequency (ω_1) up to 165 krpm (2.75 kHz) shaft speed. At this speed ($\Omega_{bifurcation}$) there is a jump from ω_1 to a second whirl frequency, ω_2. Note the second whirl frequency persists up to the highest shaft speed, 240 krpm (4 kHz).

      As the shaft decelerates, ω_2 disappears at 182 krpm (~3 kHz), and ω_1 shows up and persists up to the lowest shaft speed, 30 krpm (500 Hz). The 2nd whirl motion persists over a longer speed span during the ramp up motion than when the rotor decelerates. The differences in response (in this case ω_1, ω_2, and $\Omega_{bifurcation}$) between the ramp up and ramp down cases are hereby named hysteresis, which is a typical characteristic of subcritical bifurcations [18]. The contour map in Fig. 21 shows the

---

[§] The operating conditions follow TC manufacturer practice.

frequency jump and the hysteresis in the corresponding $\Omega_{bifurcation}$ during shaft acceleration and deceleration. Also, note the amplitude of ω_1 is higher in the vertical direction than along the horizontal direction, which will be discussed later. In each FFT, the shaft speed variation is rather fast (~6,200 rpm, 103Hz). Recall (from Table 1) the FFT step frequency Δf ~5Hz. The fast variation of shaft speed over each time span smears (no sharp peaks) the synchronous response.
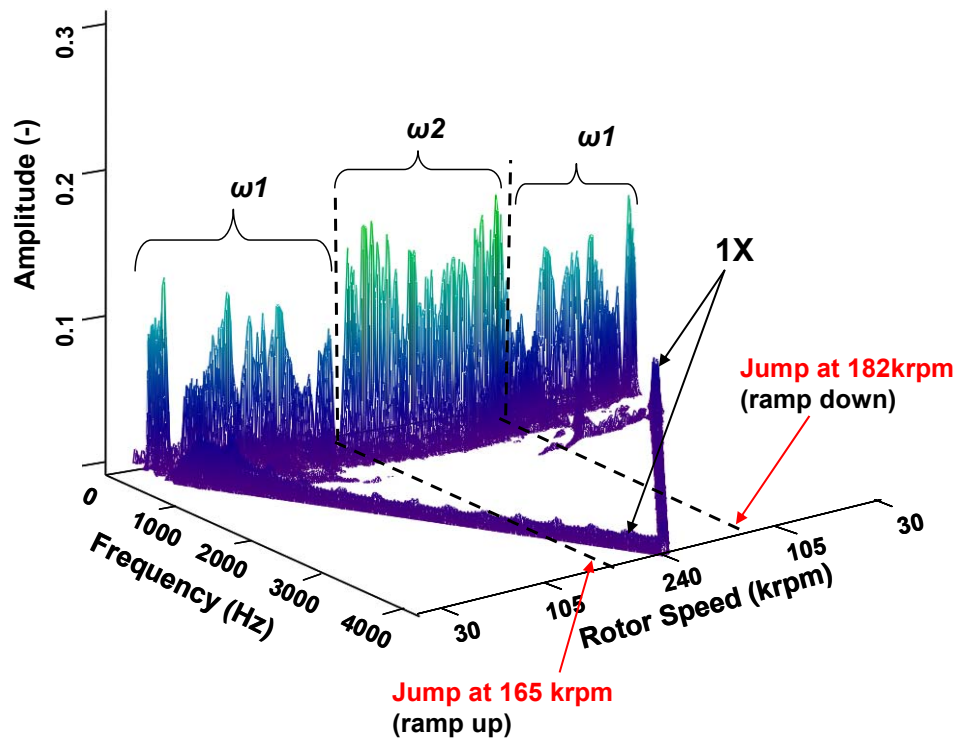

Figure 20: Waterfalls of predicted TC shaft motion at the compressor end, horizontal direction, baseline case. Shaft speed ramp rate =500 Hz/s.
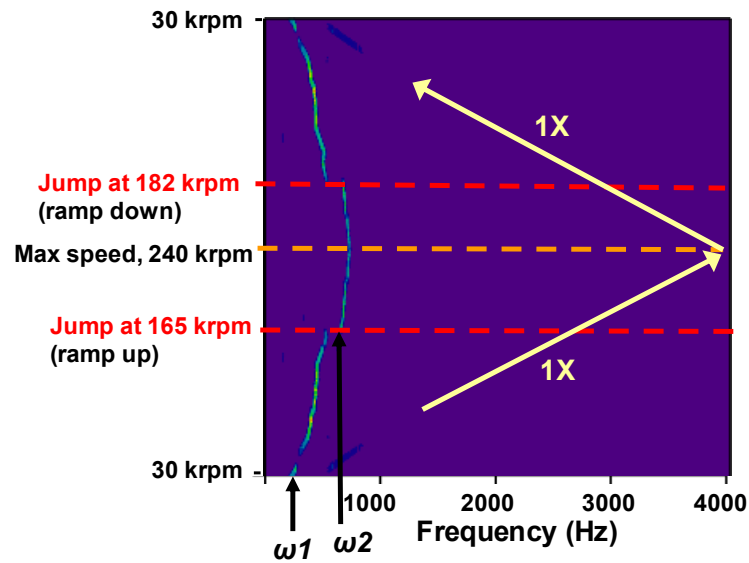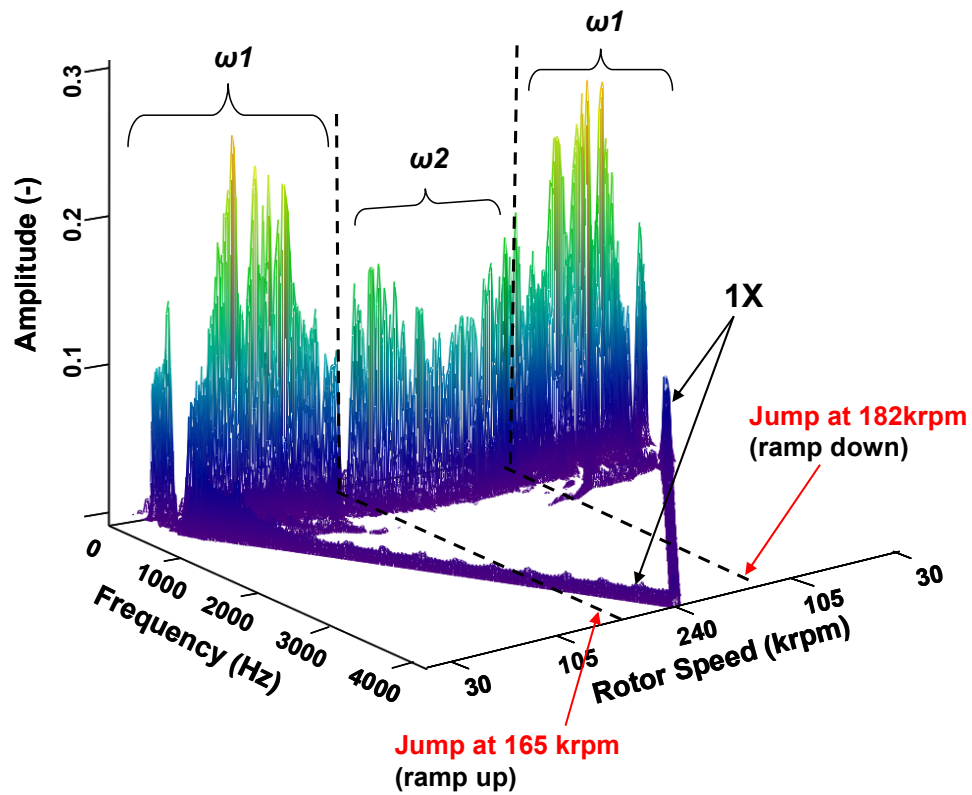
Figure 21: Waterfalls of predicted TC shaft motion at the compressor end, vertical direction; (TOP) waterfall, (BOTTOM) contour map; baseline case. Shaft speed ramp rate =500 Hz/s.

Figure 22 depicts the peak to peak (pk-pk) amplitude of shaft total motion at the compressor end during rotor acceleration (■) and deceleration (□). The total shaft motion contains amplitudes of synchronous, all subsynchronous, and supersynchronous (if any) motions. The total amplitude of shaft motion remains unchanged whether the rotor accelerates or decelerates. The amplitude of total shaft motion is between ~ 20% and 40% of the maximum allowed shaft motions at the compressor end.
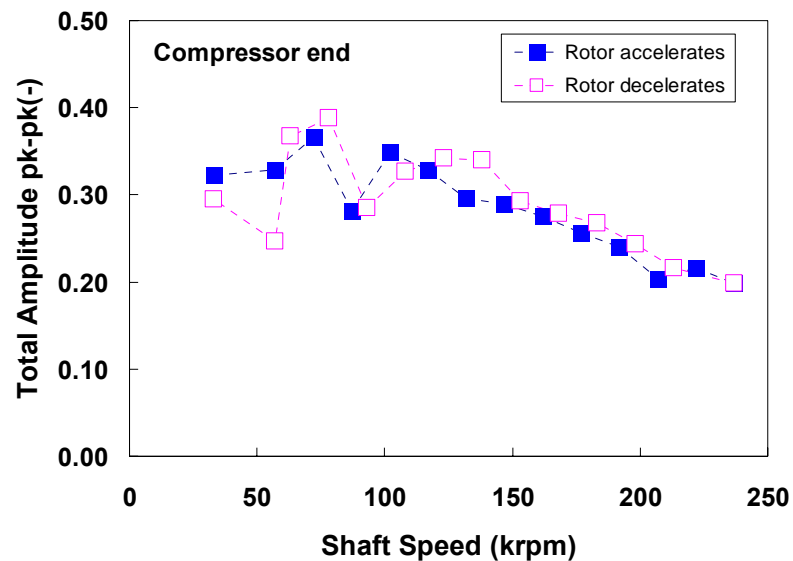
Figure 22: Total TC shaft motion (pk-pk) amplitude at the compressor end during rotor acceleration (■) and deceleration (□). Baseline case, shaft speed ramp rate =500 Hz/s.

Figure 23 (top) depicts the predicted inner and outer film static reaction forces (in vertical direction) at the (a) compressor bearing and (b) turbine bearing. The outer film static reaction forces, shown in these figures, are normalized with respect to the rotor weight, and closely correspond to the hydrostatic loads applied along the vertical direction on the bearings. Note the nearly nil inner film static loads.

Figure 23 (c) depicts the static[**] displacements (vertical direction) of the compressor ring with respect to the outer film clearance. The hydrostatic side load is applied on the ring; hence the ring eccentricity is ~ 83% of the outer film clearance at low

---

[**] The "static" displacements correspond to the zero frequency component of the DFT (Discrete Fourier Transform) of shaft motions and obtained from the time varying rotor response in the nonlinear analysis.

shaft speeds. The static displacement of the turbine ring (not shown) is similar to that of the compressor bearing, ranging from ~85% (low shaft speeds) to 70% (high shaft speeds) of the outer film clearance. Figure 23 (d) shows the journal static displacements relative to the ring (normalized with respect to the inner film clearance). As results in Figure 23(d) show, the journal (relative to the ring) static displacements vary between 0% and~ 4.5% of the inner film clearance, indicating of journal operation close to the ring center due to the nearly nil static load acting on the inner film.

Figure 24 shows the compressor ring displacements (along the vertical direction) versus time. The displacements are normalized with respect to the outer film clearance. Note the maximum peak to peak (pk-pk) ring displacement is ~ 60% of the outer film clearance. Figure 24(b) depicts the results in Fig. 24(a) in a time span from 3.9s to 3.906s. The frequency of the ring motion over this time span is ~ 667Hz (WFR~0.27), while the shaft speed is ~ 147 krpm (2,450 Hz). The pk-pk displacements at the turbine ring are smaller (maximum value ~ 15% of the outer film clearance). Time transient predictions show that ring motions have frequencies ranging from ~ 300Hz to 900Hz as the shaft speed increases from 30 krpm (500Hz) to 240 krpm (4,000Hz).

Note the outer film in a SFRB is a squeeze film damper (SFD). The results in Figure 23 show the outer film supports the hydrostatic side load. According to Refs. [39] and [40], high frequency damper journal motions and operation at high instantaneous journal eccentricities induces lubricant cavitation in the film. However, the high oil supply pressure (see Table A.5) may prevent or delay this eventuality. Refs. [42-43] show cases where a SFD without retainer springs relies on unbalance force for journal lift-off. In this study, rotor whirl motions induce inner film forces that act on the ring. The ring whirl motions generate hydrodynamic pressures in the outer film, which results in ring lift-off.
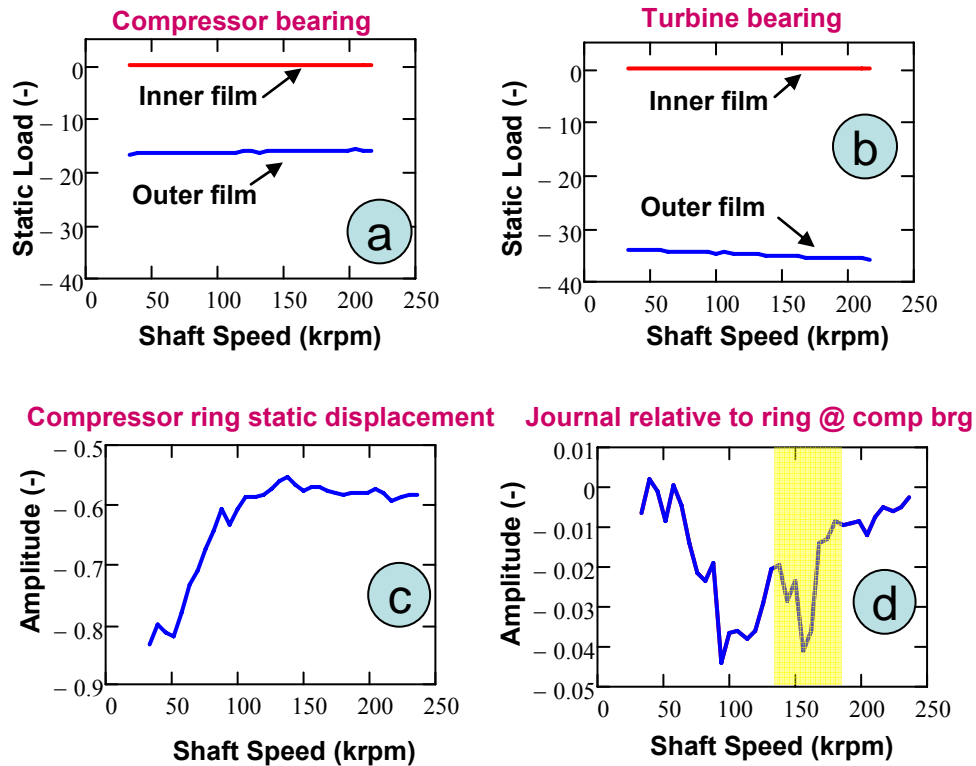
Figure 23: Prediction from transient shaft speed analysis. Static load on inner and outer films (a) compressor bearing and (b) turbine bearing; [Normalized with respect to rotor weight]. Predicted static displacements in vertical direction (c) compressor ring (normalized with respect to the outer film clearance), (d) rotor relative to the ring (normalized with respect to the inner film clearance).
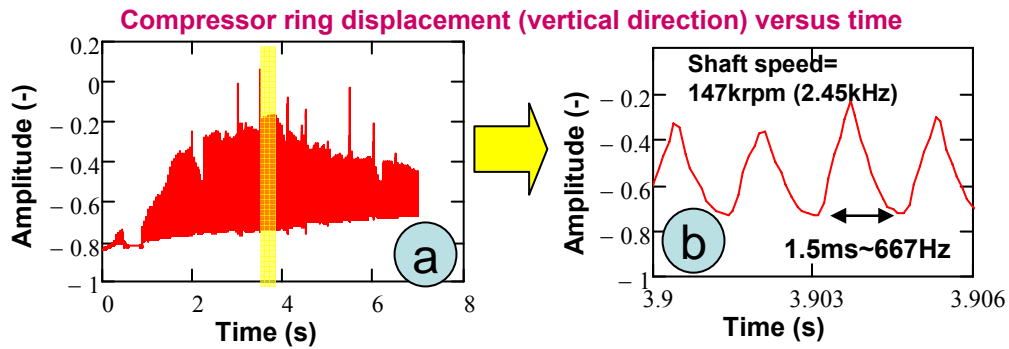
Figure 24: Compressor ring displacements along the vertical direction (from the nonlinear analysis) versus time. (a) Time between 0-7 seconds, (b) a portion of highlighted time window in (a).

Figures 25 and 26 depict the amplitude of subsynchronous whirl motions at the compressor end during rotor acceleration and deceleration, respectively. The figures

show shaft motions in (a) horizontal and (b) vertical planes. The symbols ◆ and ▲ correspond to the first (ω_1) and second (ω_2) subsynchronous frequencies, respectively. Whether the shaft accelerates or decelerates, the amplitude of first whirl frequency is somewhat larger in the vertical direction compared to that in the horizontal direction (non-circular orbits of shaft motion at low rotor speeds). The outer film forces may not be the same squeeze along the horizontal and vertical directions. In the following sections, for brevity, only the motions in the vertical direction are presented.

Results in Figs. 25(b) and 26(b) show there is hysteresis associated with $\Omega_{bifurcation}$ when the rotor accelerates and decelerates. However, there is no significant hysteresis in the amplitude of subsynchronous motion between ramp up and ramp down cases. As a note, in cases where there are multiple shaft speeds where there is a jump between ω_1 and ω_2, the one associated with the highest subsynchronous amplitude is noted as $\Omega_{bifurcation}$.
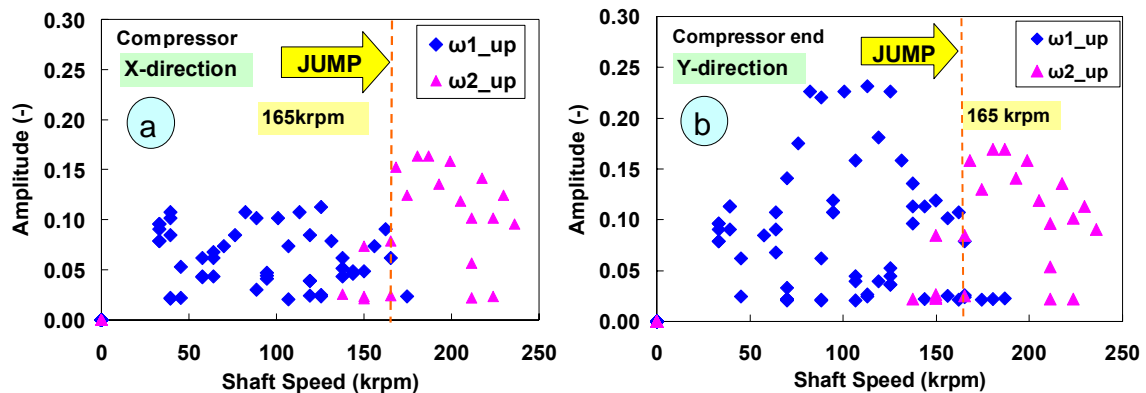
Figure 25: Subsynchronous whirl amplitudes versus shaft speed, rotor accelerates (+500Hz/s). Motions at the compressor end in (a) horizontal and (b) vertical directions. 1st whirl frequency ω_1 (◆), 2nd whirl frequency ω_2 (▲). Baseline case.
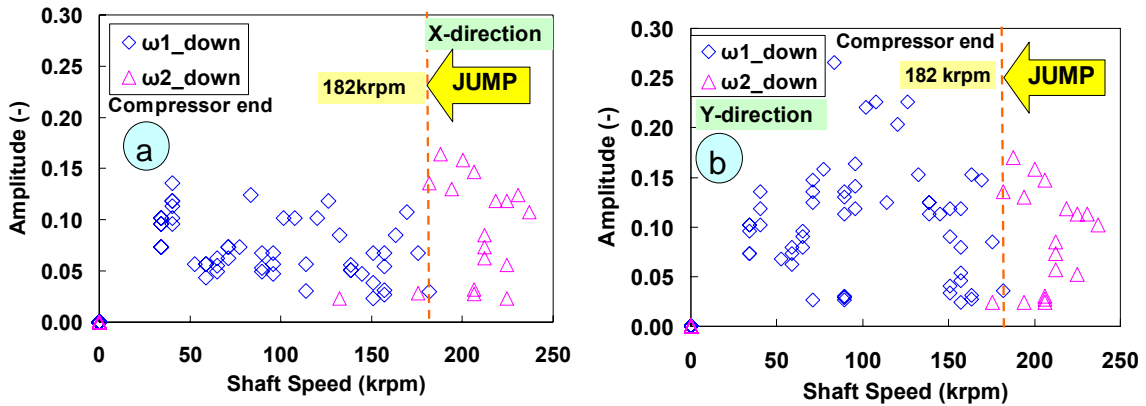
Figure 26: Subsynchronous whirl amplitudes versus shaft speed, rotor decelerates (-500Hz/s). Motions at the compressor end in (a) horizontal and (b) vertical directions. 1st whirl frequency ω₁ (◇), 2nd whirl frequency ω₂ (△). Baseline case.

Figures 27 and 28 depict the predicted subsynchronous whirl frequencies versus shaft speed during rotor acceleration and deceleration, respectively. In both figures, the corresponding whirl motion amplitudes are shown with vertical lines. The graphs provide a scale for quantifying the whirl amplitudes. The scale denotes 10% of the maximum physical displacement at the compressor end. The diamond and triangle symbols denote the first (ω_1) and the second (ω_2) subsynchronous frequencies, respectively. The mode shapes shown, are obtained by filtering the frequency content of the nonlinear response predictions (obtained at five locations in the turbocharger rotor). In other words, the frequency range of interest is selected in the results from the FFT analysis. Hence, each mode shape corresponds to a certain whirl frequency. Appendix B details the procedure in obtaining the filtered mode shapes.

Figure 27 shows the first whirl frequency (ω_1) ranges from ~300 Hz to 670 Hz, and the second frequency (ω_2) ranges from ~820 Hz to 900 Hz. High amplitude motions have characteristic frequencies mainly ranging from ~450 Hz to 600 Hz. The obtained rotor mode shapes show that the first whirl frequency (ω_1) corresponds to a conical mode, and the second whirl frequency (ω_2) represents a cylindrical bending mode. At the $\Omega_{bifurcation}$, 165 krpm (2,750 Hz), five times the first whirl frequency ($5\omega_1$) is approximately equal to four time the second whirl frequency ($5\omega_1 \sim 4\omega_2$). In addition, at $\Omega_{bifurcation}$, 165 krpm (2,750 Hz), $3\omega_1 + \omega_2 \sim \Omega_{bifurcation}$.

Figure 28 shows that during rotor deceleration, the frequency content of the first and second subsynchronous frequencies is similar to those during rotor acceleration. However, the $\Omega_{bifurcation}$ occurs at a higher shaft speed, 182 krpm (~3 kHz). Hence, the combined relation between the whirl frequencies and the running speed is $2\omega_1 + 2\omega_2$ ~$\Omega_{bifurcation}$. Interestingly, the internal relation between ω_1 and ω_2 at the $\Omega_{bifurcation}$ is identical to that during rotor acceleration.

Figure 29 overlays the predicted damped natural frequencies on the subsynchronous whirl frequencies (during rotor acceleration). The 1st whirl frequency (ω_1) follows the conical mode (with SFRB in conical mode) up to shaft speeds around 80 krpm. At shaft speeds above 80 krpm the whirl frequencies ω_1 and ω_2 do not follow any of the predicted natural frequencies from the eigenvalue analysis. Note the filtered rotor motions shown in Figs. 27 and 28 are obtained from the nonlinear analysis (see Appendix B for details). If the whirl frequencies would represent the RBS natural frequencies, based on the definition in Ref [12], the abovementioned relations, ($5\omega_1$ ~$4\omega_2$) and ($2\omega_1 + 2\omega_2$ ~$\Omega_{bifurcation}$), would be referred to as an internal resonance and a combined resonance, respectively. However, throughout this thesis these relations are called simply internal and combined relations.

Figure 27: Subsynchronous whirl frequencies versus rotor speed; acceleration = +500Hz/s; baseline case. Normalized amplitudes at compressor end in vertical direction shown (scale included).
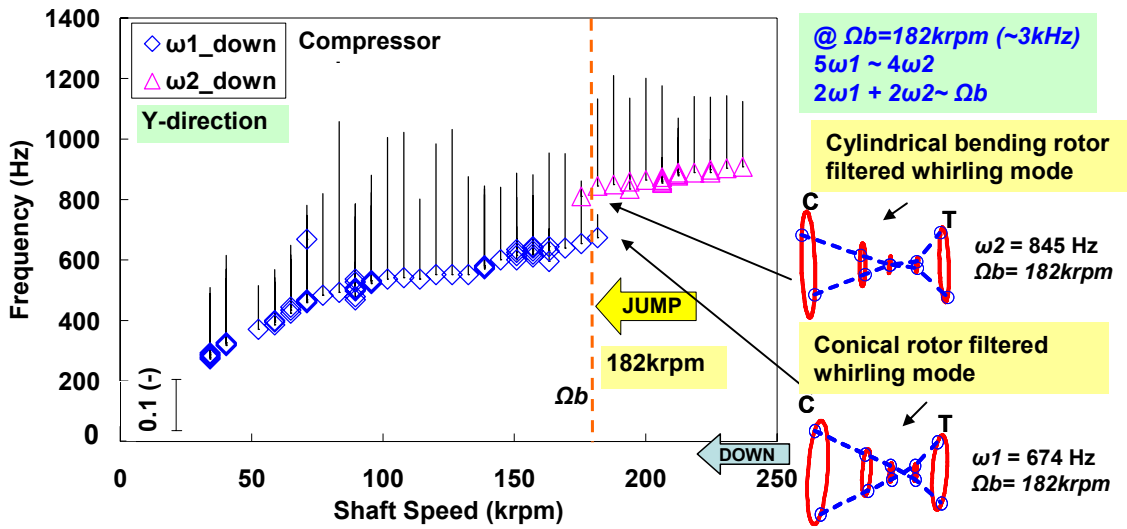
Figure 28: Subsynchronous whirl frequencies versus rotor speed; deceleration = -500Hz/s; baseline case. Normalized amplitudes at compressor end in vertical direction shown (scale included).
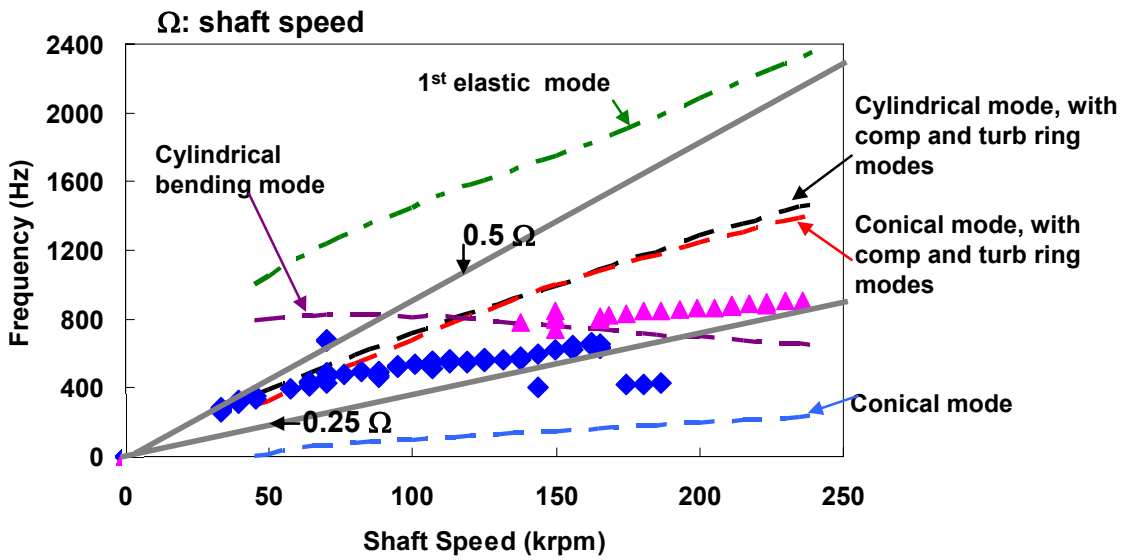
Figure 29: Subsynchronous whirl frequencies and damped natural frequencies (from eigenvalue analysis) versus rotor speed.

Figures 30 and 31 depict the predicted whirl frequency ratios (WFRs) versus rotor speed during rotor acceleration and deceleration, respectively. The WFR equals subsynchronous frequency divided by the frequency of shaft rotation. Predictions correspond to shaft motions in the vertical direction at the compressor end. The

horizontal dashed lines denote 50% and 25% of rotor speed. Results in both figures show that the subsynchronous frequencies at low shaft speeds (below 50 krpm) are 50% of the rotor speed. The ½ rotor frequency is a typical oil whirl instability in rotors supported on plain journal bearings. Since the SFRB does not rotate, the inner film acts as a plain journal bearing. In addition, at the $\Omega_{bifurcation,}$ the TC rotor whirls at a frequency close to 25% of the rotor speed. This observation holds during both rotor acceleration and deceleration for all the cases (with various operating conditions) in this thesis study. Hence, for brevity, the WFR versus shaft speed is provided only for the baseline case. In general, as the shaft speed increases, the first whirl frequency decreases from 50% to ~22% of the rotor speed, up to $\Omega_{bifurcation}$. After the frequency jump, the second whirl frequency decreases from ~30% to 20% of the rotor speed. The WFRs are almost identical during rotor acceleration and deceleration.
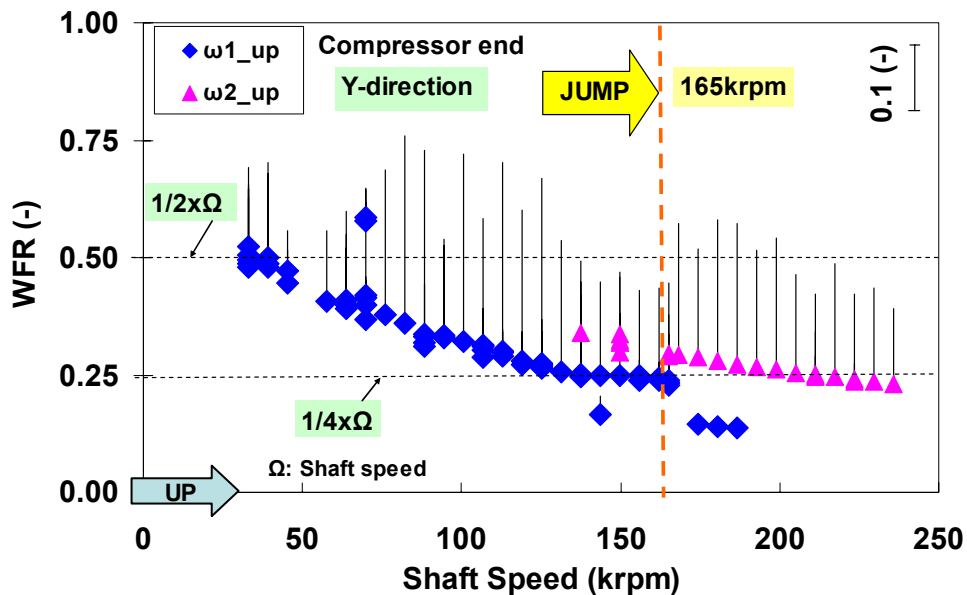
Figure 30: Predicted whirl frequency ratio versus rotor speed; acceleration = +500Hz/s; baseline case. Normalized amplitudes at compressor end in vertical direction shown (scale included).
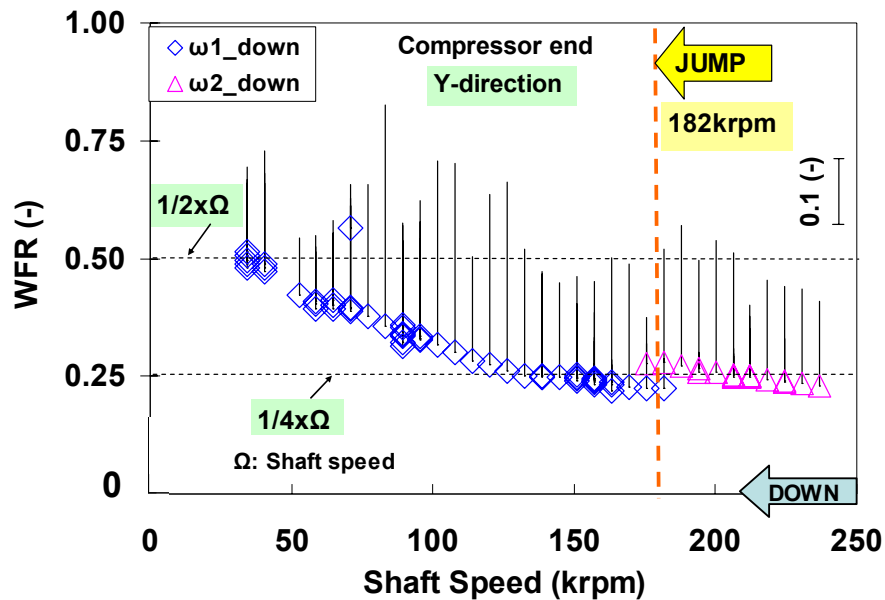
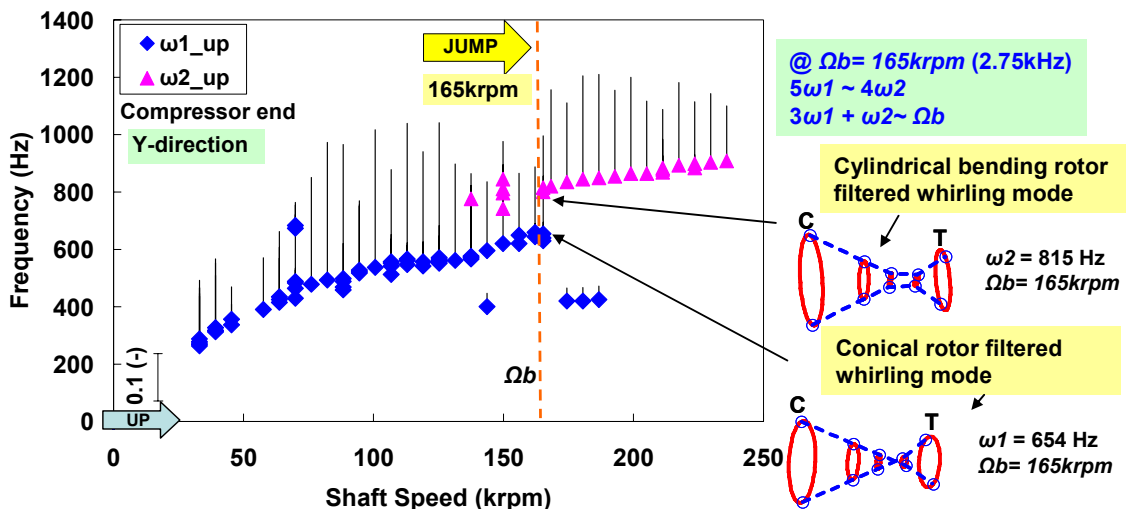**Figure 31: Predicted whirl frequency ratio versus rotor speed; deceleration = -500Hz/s; baseline case. Normalized amplitudes at compressor end in vertical direction shown (scale included).**

As a reference to the reader, Appendix C provides the waterfalls of shaft motion (vertical direction) at the compressor end for the results shown in the following sections.

The Effect of Oil Supply Pressure on Jump Phenomenon

In this section of the analysis, the supply pressure is reduced by 33% from its baseline magnitude. Figures 32 and 33 depict the predicted subsynchronous whirl frequencies versus shaft speed during rotor acceleration and deceleration, respectively. The magnitudes of the first and second subsynchronous whirl frequencies are similar to the ones in the baseline case. As a note, the decreased oil supply pressure slightly decreases the ring eccentricity (by $\sim$ 4%). A reduced oil supply pressure promotes cavitation in a squeeze film damper (SFD). Consequently, the second whirl frequency, ω_2, appears at a lower shaft speed and persists over a wider range of rotor speeds during acceleration and deceleration. The figures also show three frequency jumps and the relations between ω_1, ω_2, and the rotor speed Ω at the corresponding jump speeds, Ω_b[♣].

[♣] For brevity, from this point throughout the document Ω_b is used instead of $\Omega_{bifurcation}$

Another point of interest is the effect of supply pressure on the amplitude of total motion. Figure 34 depicts the predicted amplitudes of shaft total motions at the compressor end during rotor acceleration and deceleration for the baseline case and the reduced supply pressure case. At the lower supply pressure, the total amplitude of shaft motion is smaller, mainly due to a reduced amplitude of subsynchronous motions (i.e. see the vertical lines, representing subsynchronous amplitudes, in Figs. 27 and 32). This observation is already reported for a different TC unit in Ref [43].

Predicted results show that a higher oil inlet supply pressure delays the onset speed of the second whirl frequency, and therefore, further delays the onset of the bifurcation speed, Ω_b. This finding is consistent with measurements by Schweizer and Sievert [31] where increasing the supply pressure from 1.5 bar to 3 bar delays Ω_b from 45 krpm to 60 krpm. However, Ref. [10] reports that oil supply pressure has an insignificant effect on Ω_b. Alas, no test data is provided by the TC manufacturer to support this observation.

Figure 32: Predicted subsynchronous whirl frequencies versus rotor speed; acceleration= +500Hz/s; oil supply pressure reduced by 33%. Normalized amplitudes in vertical direction shown at compressor end (scale included).

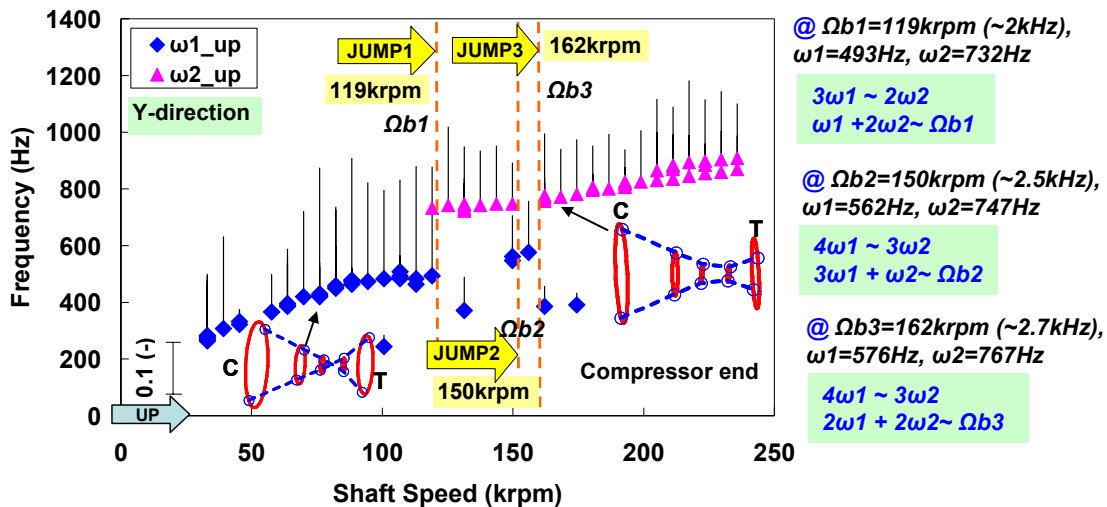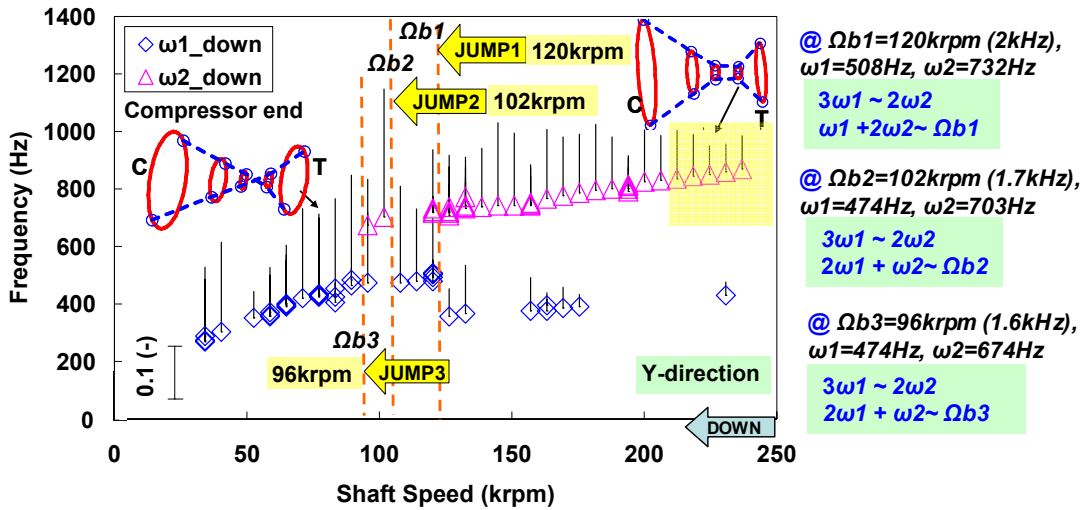**Figure 33: Predicted subsynchronous whirl frequencies versus rotor speed; deceleration= -500Hz/s; oil supply pressure reduced by 33%. Normalized amplitudes in vertical direction shown at compressor end (scale included).**
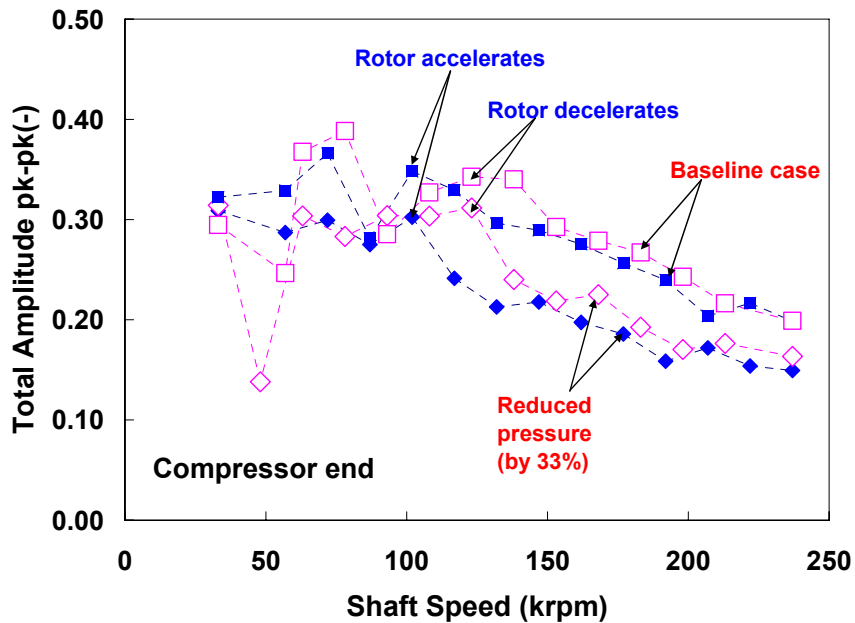

Figure 34: Predicted amplitude of total shaft motions at the compressor end during rotor acceleration and deceleration; baseline and reduced (33%) supply pressure cases.

The Effect of Oil Supply Temperature on Jump Phenomenon

This section assesses the effect of lubricant supply temperature on the subsynchronous frequency jump phenomenon of the studied TC unit. Predictions are conducted at three different oil supply temperatures: T_{low}, $T_{baseline}$, T_{high}. Table A6 lists the actual oil supply temperatures. Figure 35 shows the effective (inner and outer) oil film viscosity, at the compressor bearing, for the three oil supply temperatures. The highest (T_{high}) and the lowest (T_{low}) temperatures cause the outer film viscosity to vary by 15-20% and the inner film viscosity to vary by 10-15% from the ones in the baseline case.

Figures 36 and 37 show the predicted subsynchronous whirl frequencies at the compressor end for T_{low} and T_{high} oil supply temperatures, respectively. The results in the top graphs correspond to cases with rotor accelerating, and the bottom graphs correspond to speed ramp down cases. Figure 36 also includes an inset corresponding to the whirl frequency versus shaft speed for the baseline case. Despite the changes in inner and outer oil film viscosities, the subsynchronous (as well as the total) amplitudes of shaft motions remain similar in all cases with various oil supply temperatures. However, the supply temperature affects the speeds at which the whirl frequencies (ω_1 and ω_2) appear (or disappear). Increasing the oil supply temperature from T_{low} to $T_{baseline}$ increases the Ω_b during ramp down (from 163 krpm to 182 krpm). However, further increasing the oil supply temperature from $T_{baseline}$ to T_{high}, lowers the onset speed of ω_2 appearance, with Ω_b occurring at a lower speed (150 krpm). This finding is consistent with the test data provided in Figs. 2 and 3 where increasing the oil supply temperature from 30°C to 100°C decreases the Ω_b (from 108 krpm to 84 krpm). Note the multiple frequency jumps in Fig. 37 as a result of a reduced oil viscosity (higher temperature). Interestingly, at a certain oil supply temperature, the internal relations between ω_1 and ω_2 (provided in Figs. 36 and 37) remain the same at all jump speeds during rotor acceleration and deceleration. In other words, at all bifurcations speeds, Ω_b, at T_{low} oil supply temperature, $5\omega_1 \sim 4\omega_2$ and at T_{high} oil supply temperature, $4\omega_1 \sim 3\omega_2$.
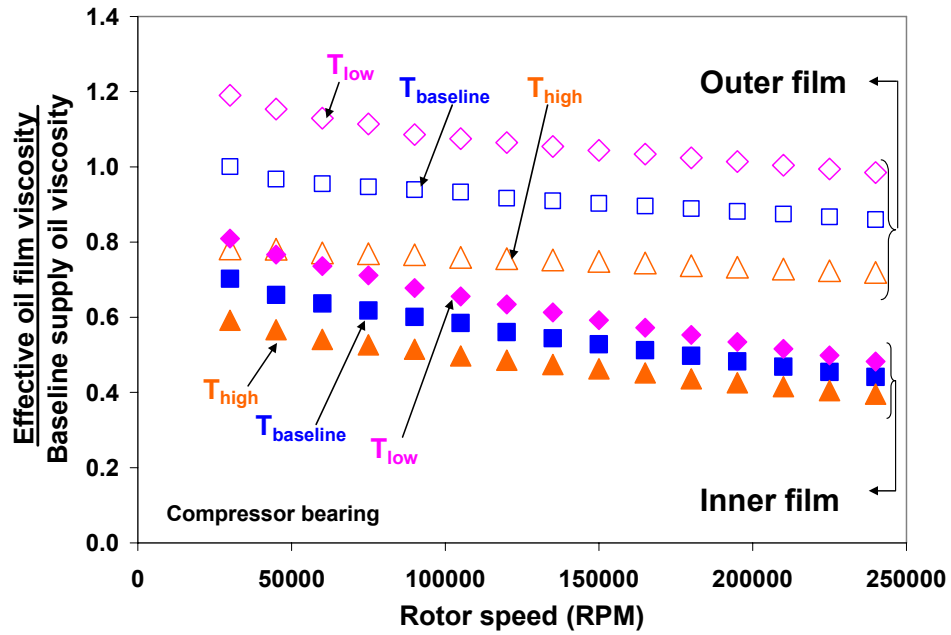
Figure 35: Predicted effective (inner and outer) oil film viscosity (at compressor bearing) at three oil supply temperatures (baseline case, above and below baseline temperature).
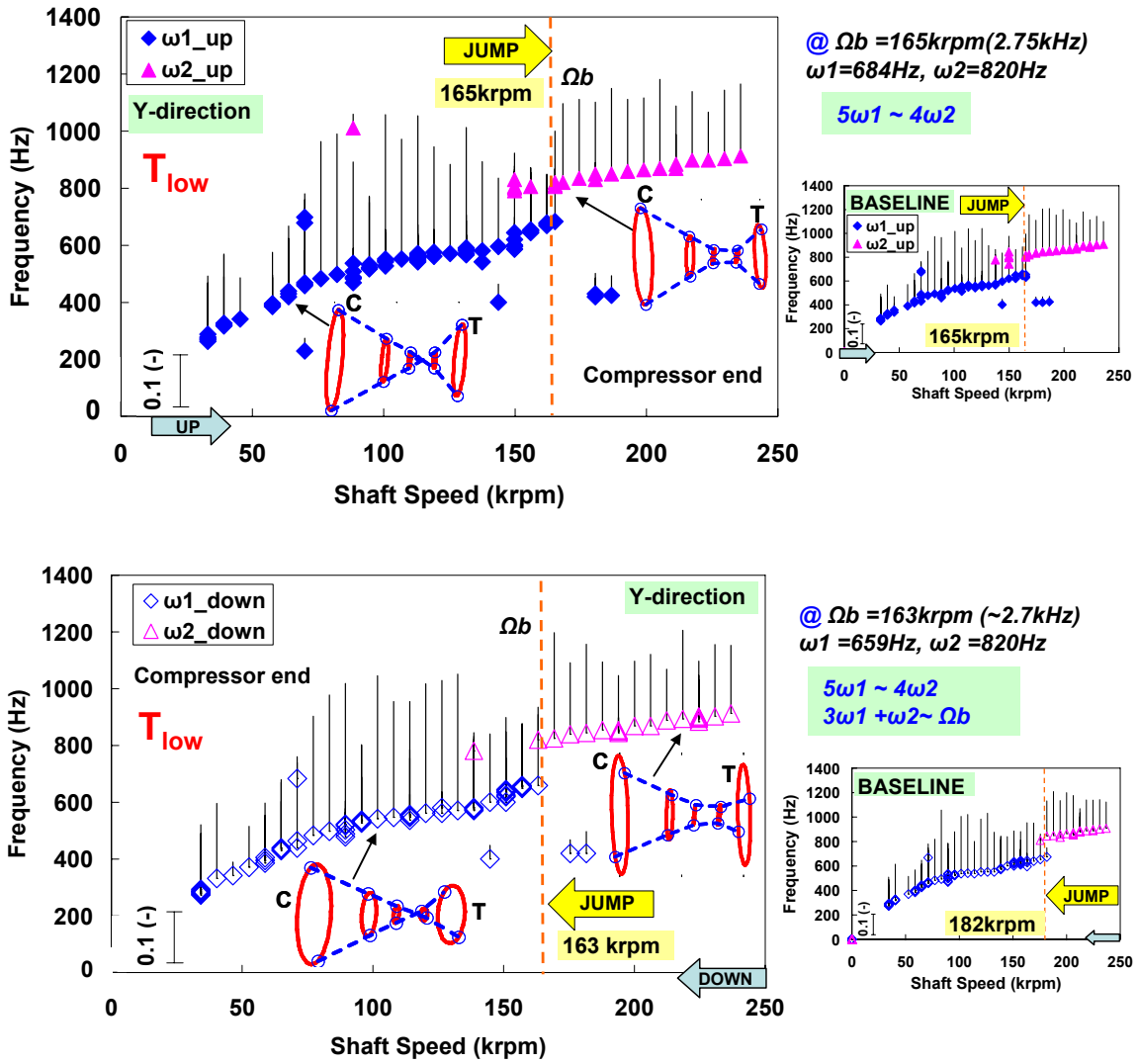
Figure 36: Predicted subsynchronous whirl frequencies versus rotor speed; reduced oil supply temperature (T_low). (TOP) rotor acceleration = 500Hz/s; (BOTTOM) rotor deceleration= -500Hz/s. Normalized amplitudes in vertical direction shown at compressor end (scale included).

Figure 37: Predicted subsynchronous whirl frequencies versus rotor speed; increased oil supply temperature (T$_{high}$). (TOP) rotor acceleration = 500Hz/s; (BOTTOM) rotor deceleration= -500Hz/s. Normalized amplitudes in vertical direction shown at compressor end (scale included).

The Effect of Bearing Inner Film Length on Jump Phenomenon

The bearing inner film length is increased by 15%, (compared to the baseline length), and nonlinear predictions are obtained for shaft speed ramp up and ramp down cases. In this analysis, the hydrostatic side loads applied on the bearings are identical to the ones in the baseline case. Therefore, the ring static displacement is the same as for the baseline case. Figure 38 depicts the subsynchronous whirl frequencies at the compressor end versus shaft speed. The figures include insets corresponding to the results for the baseline case. The shaft amplitudes of total motions decrease by~ 11% with increasing the bearing inner length. This observation is consistent with the general statement in Ref. [15] regarding the increase in amplitude of TC shaft motion as a result of shortening the bearing inner film length.

For the longer inner film length, at shaft speeds between 120 krpm (~2 kHz) and 162 krpm (2.7 kHz), the first subsynchronous whirl frequency, ω_1, increases. This increase in ω_1 creates a smooth transition between ω_1 and ω_2 at Ω_b=162 krpm during ramp up and at Ω_b=163 krpm (~2.72 kHz) during rotor deceleration. Figure 38 (top) shows an inset of (normalized) rotor static displacement (in vertical direction) relative to the ring at the compressor bearing. The highlighted regions correspond to the shaft speeds over which ω_1 increases (compared to the baseline case).

Recall the baseline case where the rotor static displacement shows a sudden dip at around Ω_b, see Fig. 23(d) (highlighted region), with a jump in whirl frequency at Ω_b, see Fig 27. Presently, for the bearing with a longer inner length, at speeds around Ω_b the journal climbs smoothly towards the ring center, without showing a jump in whirl frequency (see Fig. 38). For the same applied static load on the bearing, the rotor operates closer to the center when the inner film length is increased. Therefore, journal operation is similar to the one at high shaft speeds, which explains the increase in ω_1 at shaft speeds close to Ω_b.

Interestingly, the subsynchronous frequencies (and amplitudes) remain unchanged for the two studied inner film lengths, at low (below 100 krpm) and at high (above 170 krpm) shaft speeds. The main discrepancies occur at shaft speeds close to the bifurcation speed.

Figure 38: Predicted subsynchronous whirl frequencies versus rotor speed; bearing inner length increased by 15% (compared to baseline case). (TOP) rotor acceleration = 500Hz/s; (BOTTOM) rotor deceleration = -500Hz/s. Normalized amplitudes in vertical direction shown at compressor end (scale included).
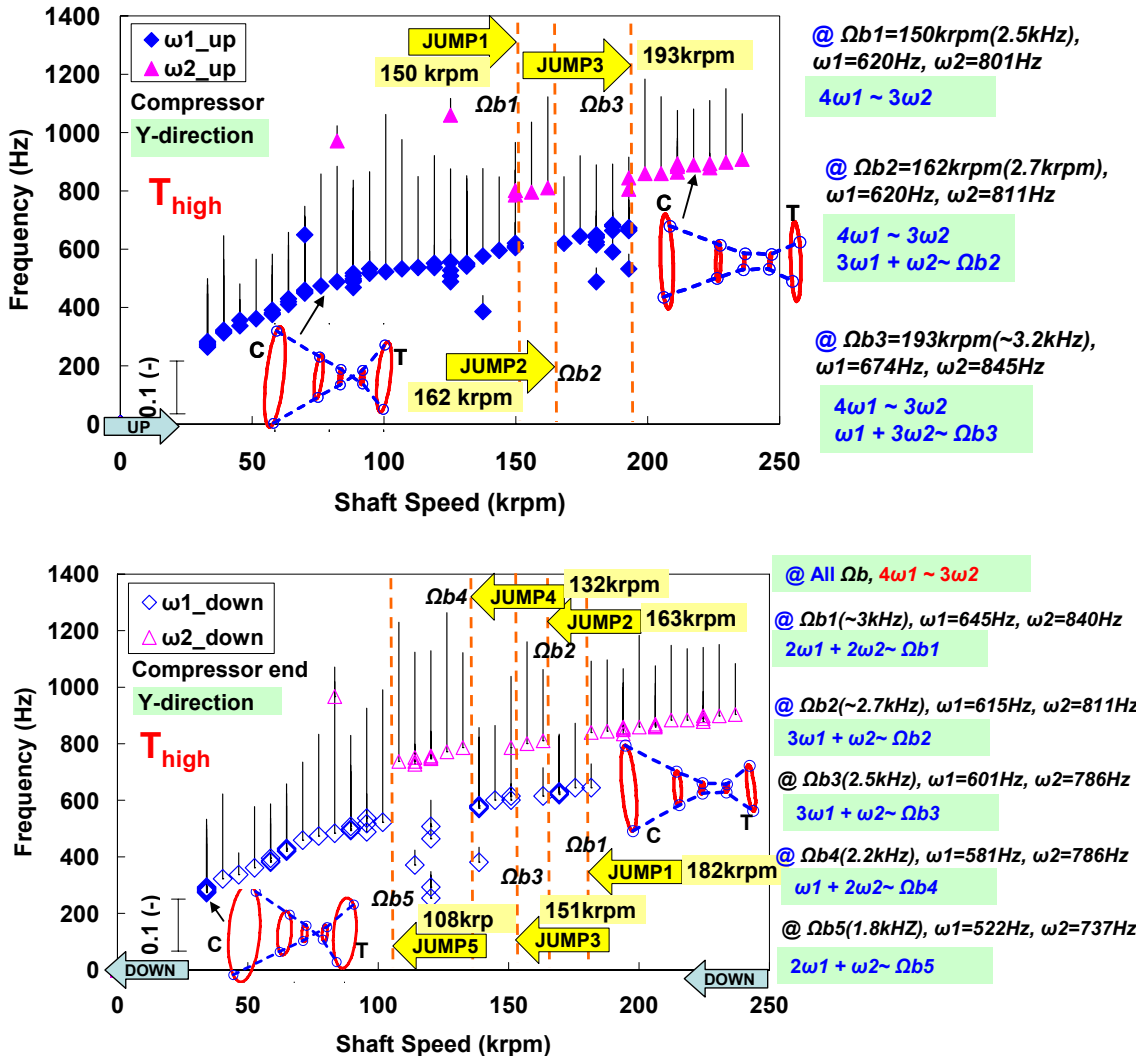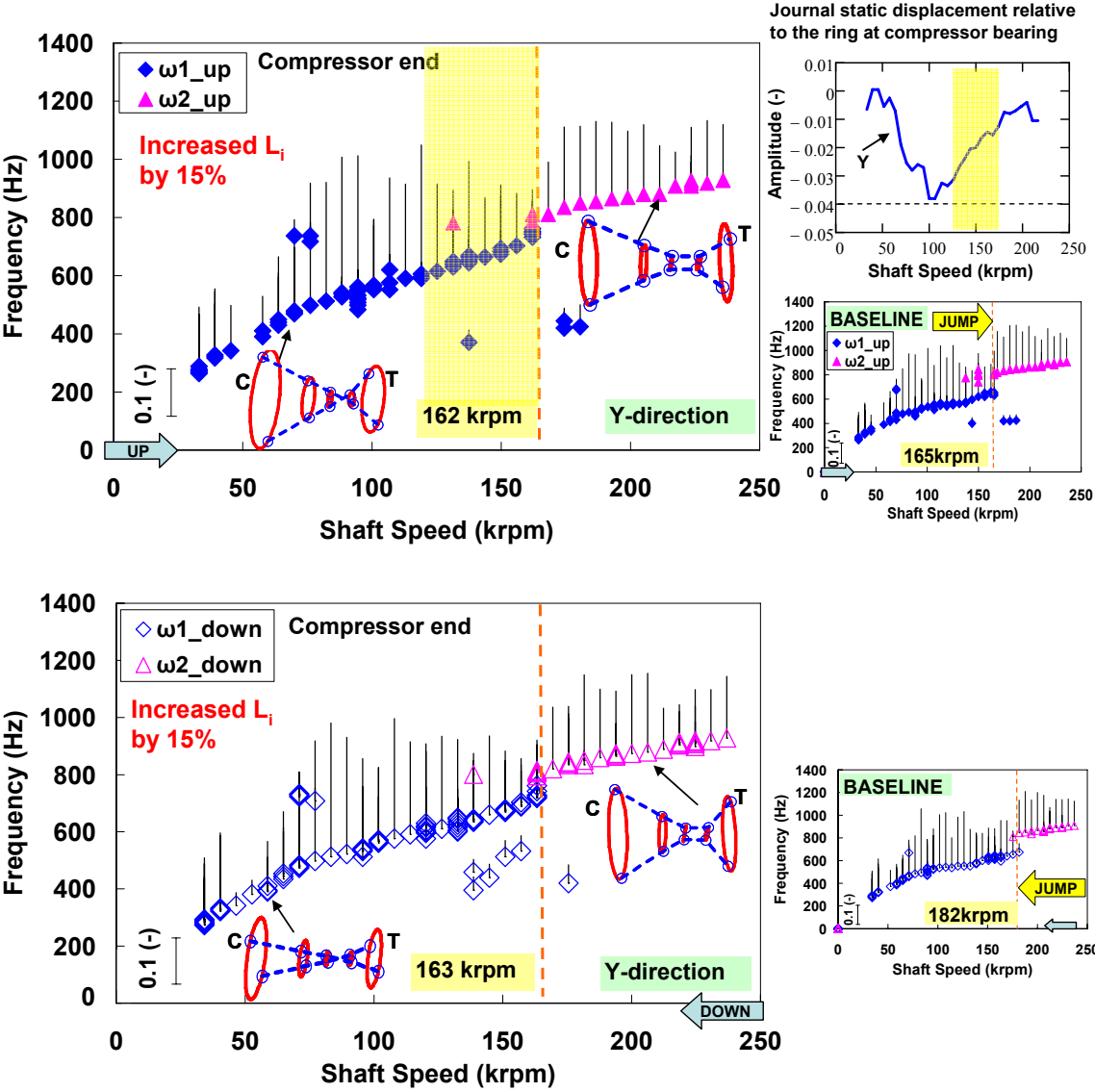
The Effect of Rotor Acceleration/Deceleration on Jump Phenomenon

The effect of rotor acceleration or deceleration on the frequency jump phenomenon is assessed. Predictions are conducted at fixed shaft speeds as well as with various shaft speed ramp rates: 250 Hz/s, 500 Hz/s (baseline case), and 750 Hz/s. In order to reduce computational time, predictions for the 250 Hz/s ramp rate are conducted only at shaft speeds between 90 krpm (1.5 kHz) and 190 krpm (~3.2 kHz) (includes the bifurcation speed). Figure 39 depicts the amplitude of total shaft motion (pk-pk) at the rotor compressor end during rotor (a) acceleration and (b) deceleration as well as for the fixed shaft speed condition. The amplitude of total motion remains unchanged with shaft acceleration or deceleration, and it is between 20% and 40% of the physical limit at the compressor end. As the rotor speed increases, the amplitude of total motion decreases.

Figure 40 depicts the subsynchronous whirl frequency versus shaft speed at the compressor end. The shaft accelerates (top graph) and decelerates (bottom graph) with 250 Hz/s ramp rate. In addition, the figure shows the subsynchronous whirl frequencies for the baseline case (500 Hz/s). Results in Fig. 40 shows an internal relation between the whirl frequencies, $4\omega_1 \sim 3\omega_2$, similar for both ramp up (+250 Hz/s) and ramp down (-250 Hz/s) cases. Figure 41 depicts the whirl frequencies versus rotor speed for 750 Hz/s ramp rate. In this case, the internal relations between the whirl frequencies ω_1 and ω_2 are different during rotor acceleration and deceleration. In other words, at high speed ramp rates, there is hysteresis in the internal relations between the two whirl frequencies. The reason is that at high speed ramp rates there is a larger difference between Ω_b during rotor acceleration and deceleration. Therefore, the corresponding whirl frequencies (ω_1 and ω_2) at Ω_b (and the internal relations between them) are different for the speed ramp up and speed ramp down cases (see Fig. 41 for the appropriate relationship).

In general, increasing the rotor spin acceleration delays the bifurcation speed Ω_b. In addition, decreasing the rotor rate of speed change decreases the difference between Ω_b values during rotor acceleration and deceleration. For instance, the difference between the bifurcation speeds during rotor acceleration and deceleration are as follows: 7 krpm (for 250 Hz/s), 17 krpm (for 500 Hz/s), and 58 krpm (for 750 Hz/s). In other

words, increasing the shaft speed ramp rate leads to a stronger hysteresis in Ω_b during ramp up and ramp down cases.

Prior work by San Andrés and the author [44], related to the effect of shaft acceleration/deceleration on the dynamic response of turbochargers, also shows that a higher speed ramp rate leads to a stronger hysteresis of subsynchronous whirl motions (amplitude and frequency). This behavior is common in nonlinear systems, and it is a characteristic of subcritical bifurcation.
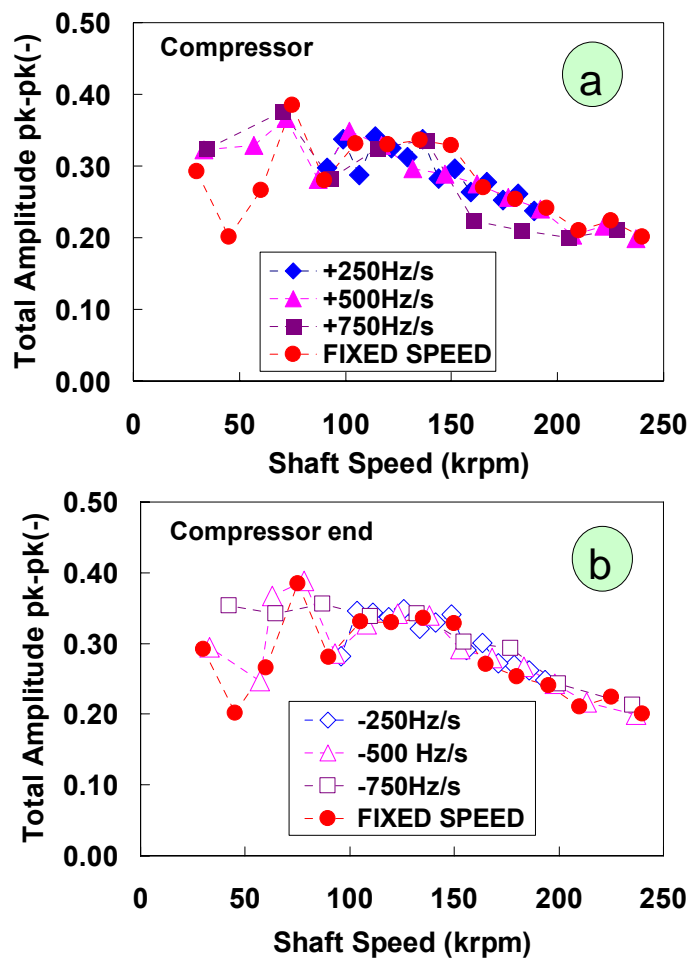
Figure 39: TC total shaft motion amplitude (pk-pk) at compressor end during rotor (a) acceleration and (b) deceleration; speed ramp rates= 0Hz/s (fixed speed), 250Hz/s, 500Hz/s, 750Hz/s.
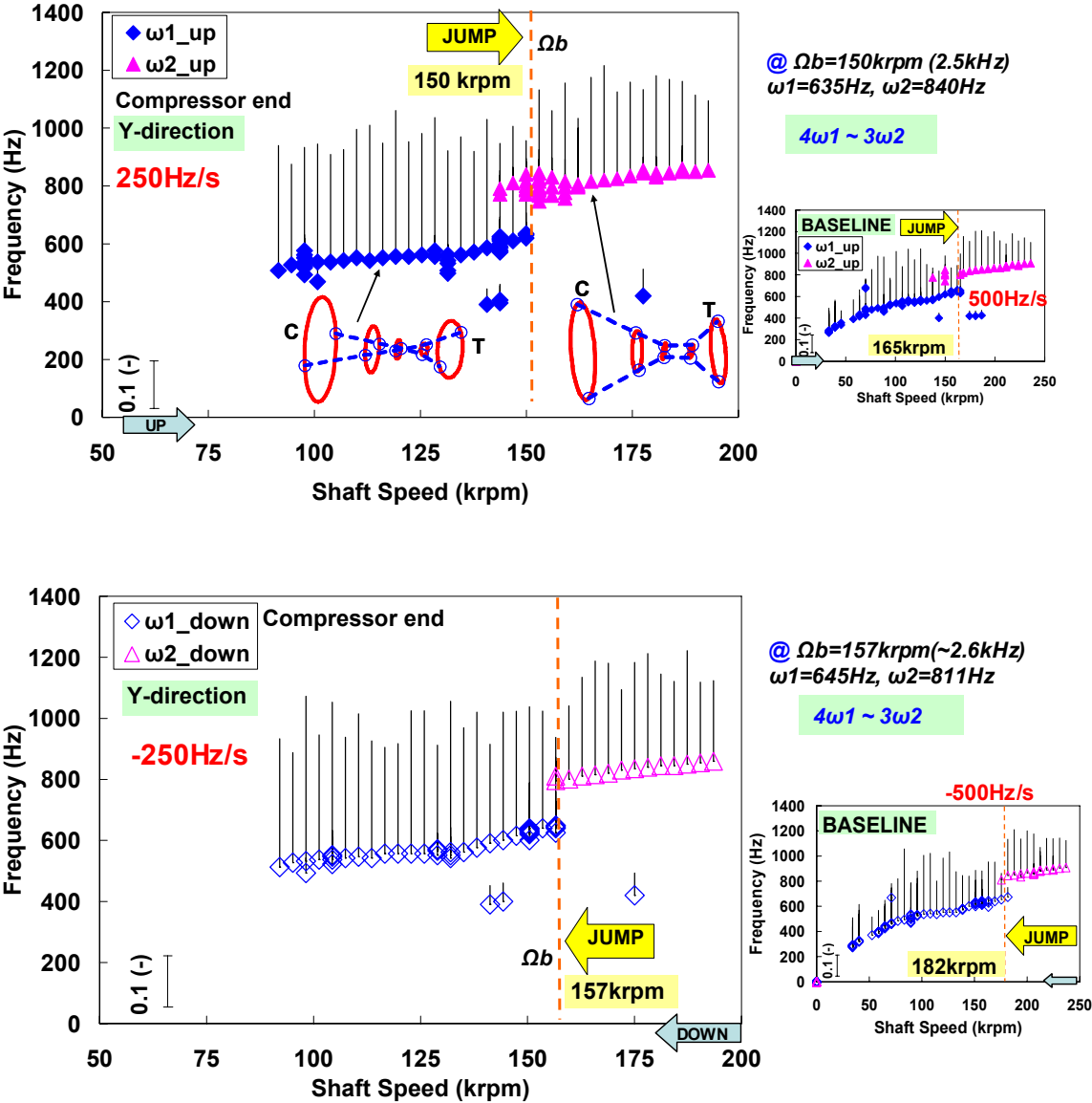
Figure 40: Predicted subsynchronous whirl frequencies versus rotor speed; (TOP) rotor acceleration = +250Hz/s; (BOTTOM) rotor deceleration = -250Hz/s. Normalized amplitudes in vertical direction shown at compressor end (scale included).

Figure 41: Predicted subsynchronous whirl frequencies versus rotor speed; (TOP) rotor acceleration = +750Hz/s; (BOTTOM) rotor deceleration = -750Hz/s. Normalized amplitudes in vertical direction shown at compressor end (scale included).

The Effect of Imbalance Distribution on Jump Phenomenon

In this analysis a four-plane imbalance distribution is applied (at the compressor nose, compressor back, turbine nose, and turbine back). The imbalance amount remains constant but the phase is varied (0° or 180°), creating three different imbalance distribution: opposed couple, static all-in-phase (baseline case), and turbine-back-out-of-phase. An inset in Figures 43 and 44 shows the imbalance condition in the TC. Further nonlinear predictions of TC dynamic response are conducted with the three imbalance distributions.

Figure 42 depicts the shaft total motions at the compressor end for the opposed coupled imbalance distribution. As the shaft speed increases, the total amplitude of shaft motion decreases from ~38% to ~10% of the maximum physical limit at the compressor bearing. Recall from Figure 23 that the total shaft motions for the baseline case (static imbalance) varies between 40% and 20% of the maximum physical limit at the compressor end. Therefore, the opposed couple imbalance leads to a decrease of the total shaft motion at high rotor speeds.

Figure 43 depicts the predicted subsynchronous whirl motions versus shaft speed for the opposed couple imbalance distribution. The opposed couple distribution delays the bifurcation speed Ω_b to 180 krpm (3 kHz) during rotor acceleration. Recall in the baseline case (static imbalance distribution), Ω_b equals 165 krpm (2.75 kHz) during rotor acceleration. Note the decreased amplitude of subsynchronous whirl motion at high shaft speeds (highlighted in Fig. 43). Indeed, the total motions at high shaft speeds reduce for the opposed couple case due to the decrease in amplitudes of subsynchronous motions.

Figure 42: Total TC shaft motion (pk-pk) amplitude at the compressor end during rotor acceleration (■) and deceleration (☐); imbalance distribution: opposed couple. Shaft speed ramp rate =500 Hz/s.
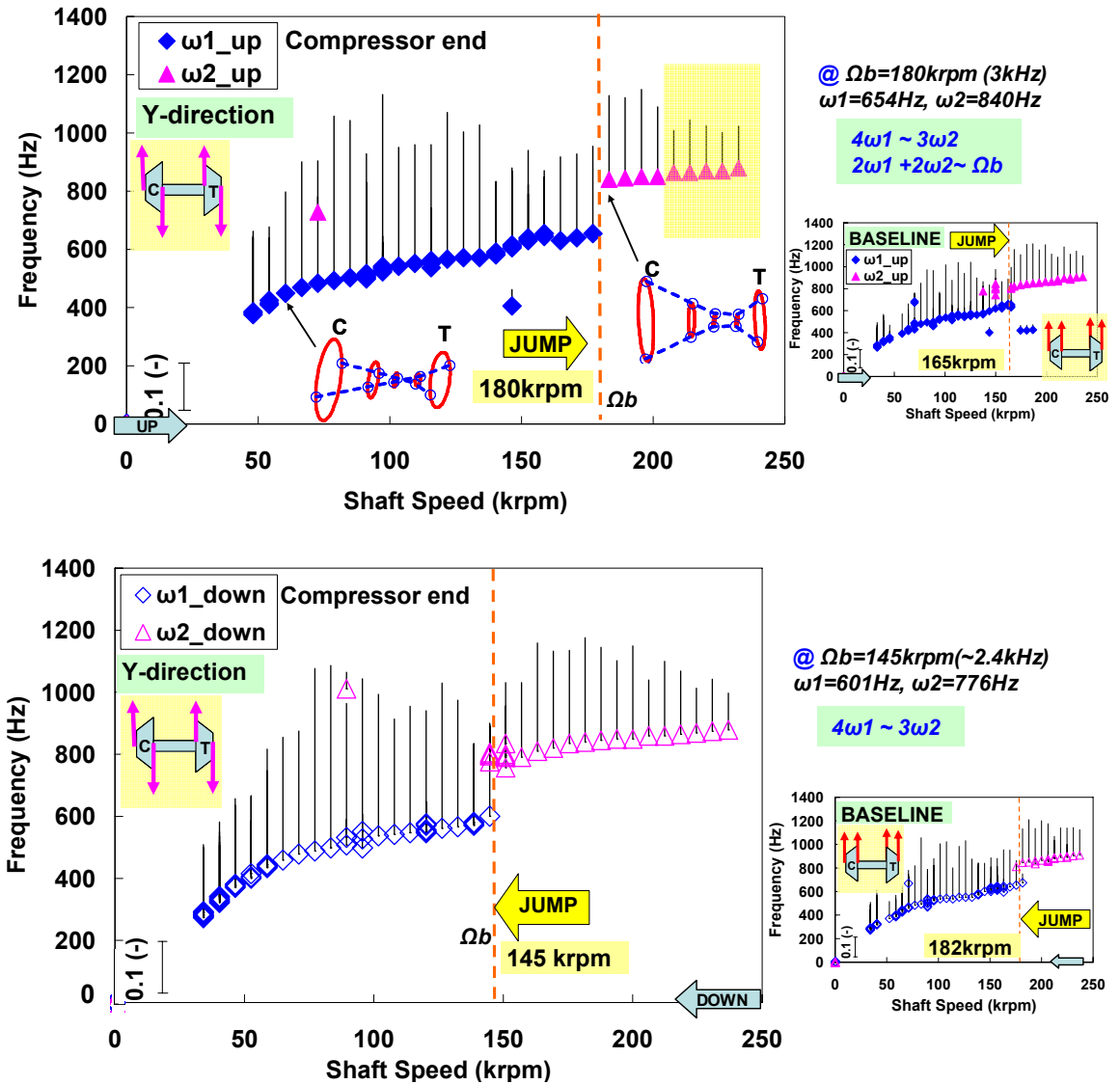
Figure 43: Predicted subsynchronous whirl frequencies versus rotor speed; imbalance distribution: opposed couple. (TOP) Rotor acceleration = 500Hz/s; (BOTTOM) Rotor deceleration= -500Hz/s. Normalized amplitudes in vertical direction shown at compressor end (scale included).
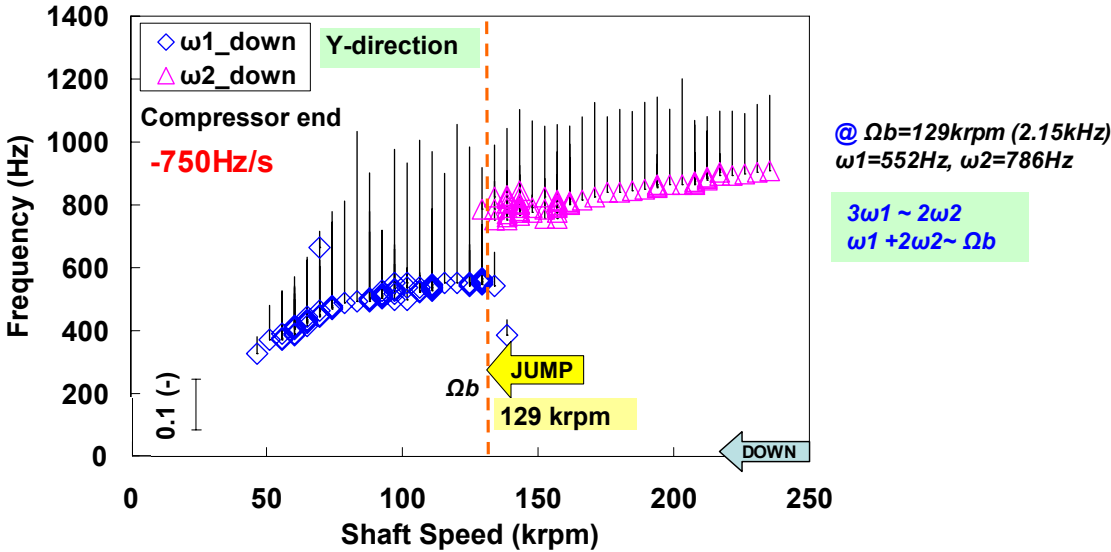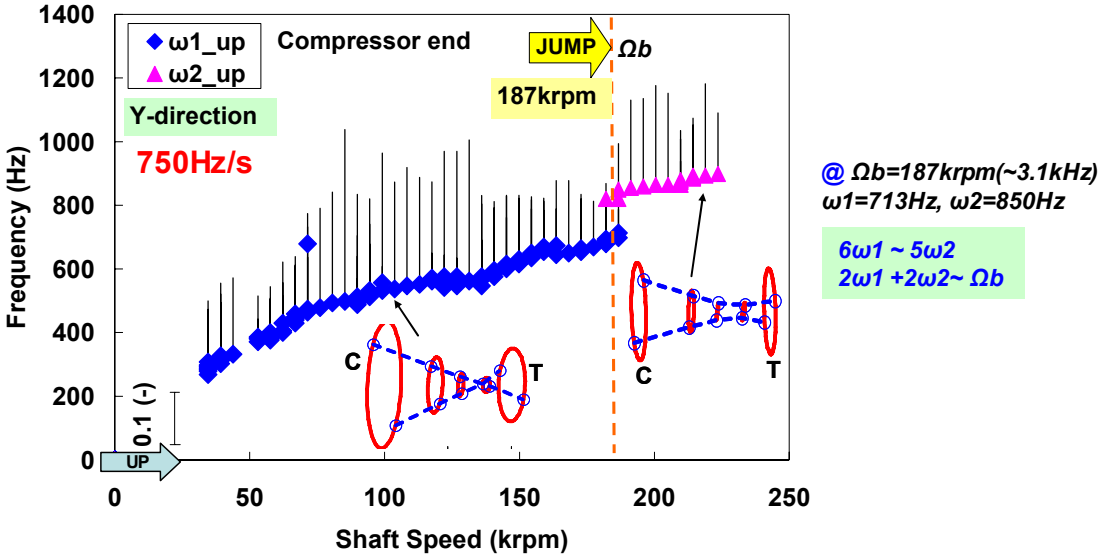
Figure 44 depicts the predicted subsynchronous frequencies versus shaft speed for the turbine-back-out-of-phase (TBOP) imbalance distribution. This imbalance condition decreases the Ω_b for both, shaft speed ramp up and ramp down cases. However, the second whirl frequency, ω_2 disappears shortly after the bifurcation speed. During rotor deceleration, the second whirl frequency appears at the highest shaft speed; however, it has a small amplitude of motion. In this case, the internal relations between the two whirl frequencies, ω_1 and ω_2, at Ω_b are different during ramp up ($4\omega_1 \sim 3\omega_2$) and ramp down ($3\omega_1 \sim 2\omega_2$) motions. The combined relations for the speed ramp up ($3\omega_1 + \omega_2 \sim \Omega_b$) and speed ramp down ($\omega_1 + 2\omega_2 \sim \Omega_b$) cases are also different. However, these combined relations are different during shaft acceleration and deceleration in most cases (unless Ω_b is almost identical during either a shaft speed ramp up or a ramp down case).

Figure 45 depicts the total amplitude of shaft motion at the compressor end for the TBOP imbalance. Note at rotor speeds above ~160 krpm the total amplitude of shaft motion is less than 10% of the physical limit at the compressor end. Due to the reduced amplitudes of motion, the TBOP imbalance distribution is particularly interesting. For completeness, the effect of an increased imbalance amount (for the TBOP distribution) on the frequency jump phenomenon is assessed next.

Figure 44: Predicted subsynchronous whirl frequencies versus rotor speed; imbalance distribution: turbine back out of phase. (TOP) Rotor acceleration = 500Hz/s; (BOTTOM) Rotor deceleration= -500Hz/s. Normalized amplitudes in vertical direction shown at compressor end (scale included).
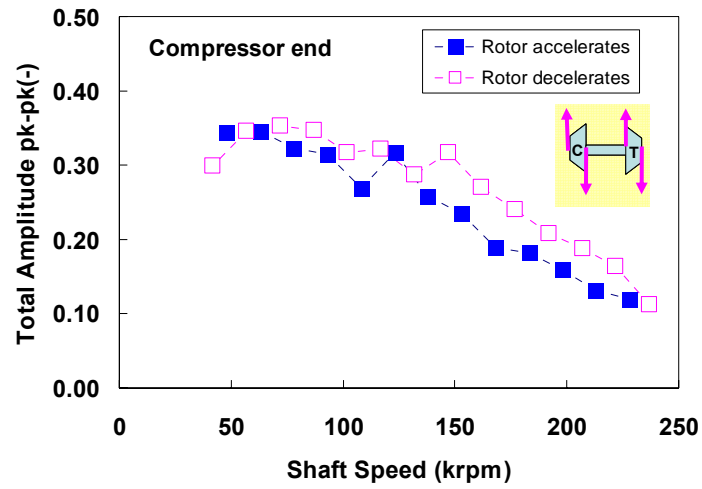
Figure 45: Total TC shaft motion (pk-pk) amplitude at the compressor end during rotor acceleration (■) and deceleration (□); imbalance distribution: turbine-back-out-of-phase. Shaft speed ramp rate =500 Hz/s.

Figure 46 depicts the subsynchronous whirl frequency versus shaft speed for a case with turbine-back-out-of-phase imbalance distribution. However, the imbalance amounts are twice the ones in the previous distribution. Note with increased imbalance amounts, the whirl frequencies disappear at ~100 krpm (1.67 kHz) for both speed ramp up and ramp down cases. There are no bifurcations in this case. This observation agrees with the test data in Fig. 6, where increased imbalance amounts leads to subsynchronous whirl motion disappearance, (i.e. stability!).   Figure 47 shows the total amplitude of shaft motion at the compressor end. Expectedly, the total amplitude decreases at shaft speeds above ~100 krpm (where the subsynchronous whirl motions disappear). However, the total amplitude of shaft motion increases with rotor speed due to the increased imbalance amounts (which increases the amplitude of synchronous motions). See Appendix C for the waterfalls of shaft motion.

Overall, the imbalance distribution greatly affects the subsynchronous whirl motions (amplitude and frequency); hence, also the bifurcation speeds and the internal relations between the whirl frequencies. In addition, the imbalance distribution also affects the degree of hysteresis in the RBS nonlinear response.
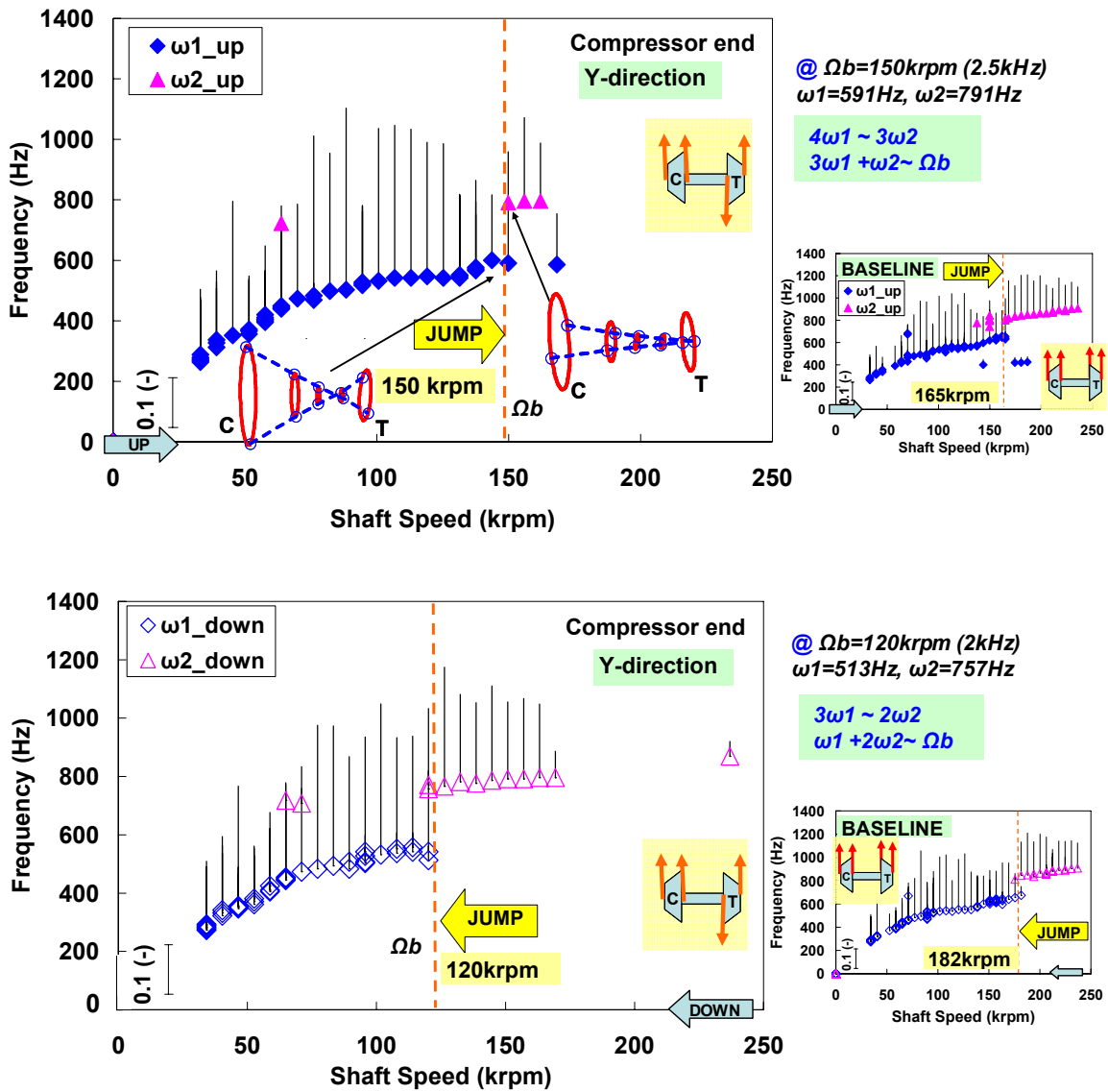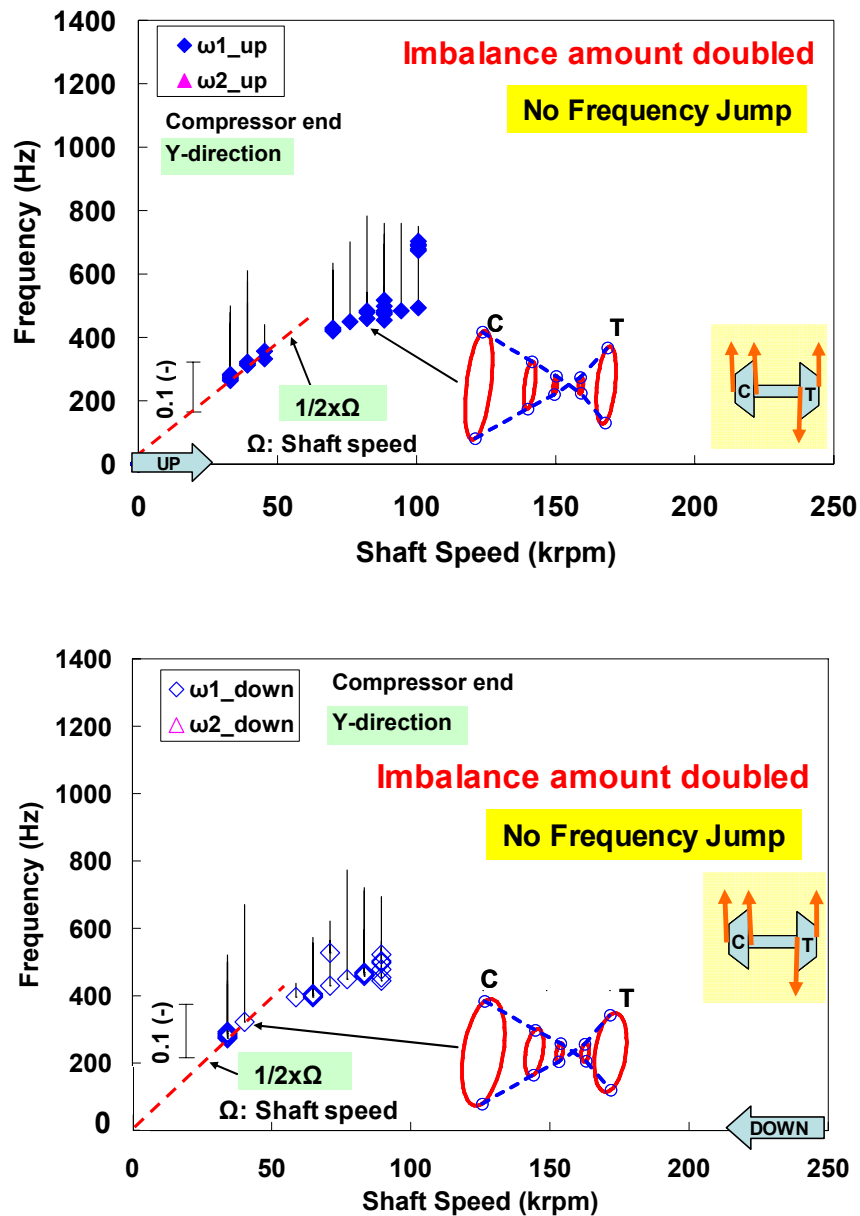
Figure 46: Predicted subsynchronous whirl frequencies versus rotor speed; imbalance distribution: turbine back out of phase; imbalance amount doubled. (TOP) Rotor acceleration = 500Hz/s; (BOTTOM) Rotor deceleration= -500Hz/s. Normalized amplitudes in vertical direction shown at compressor end (scale included).
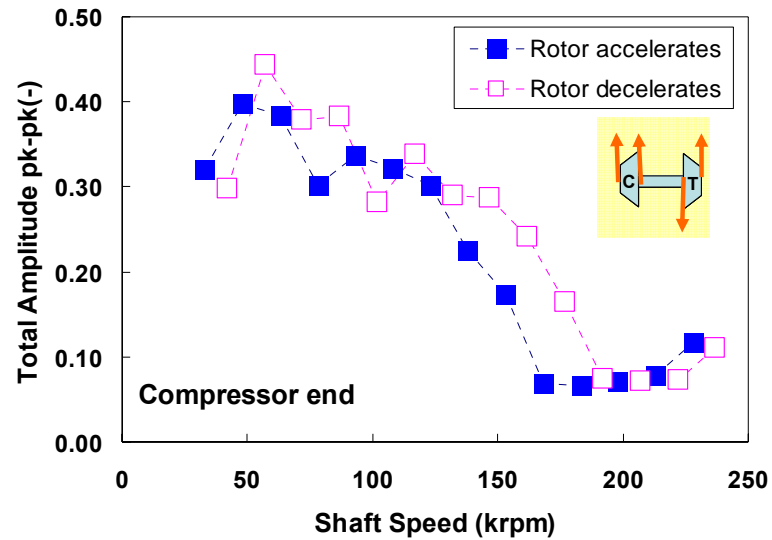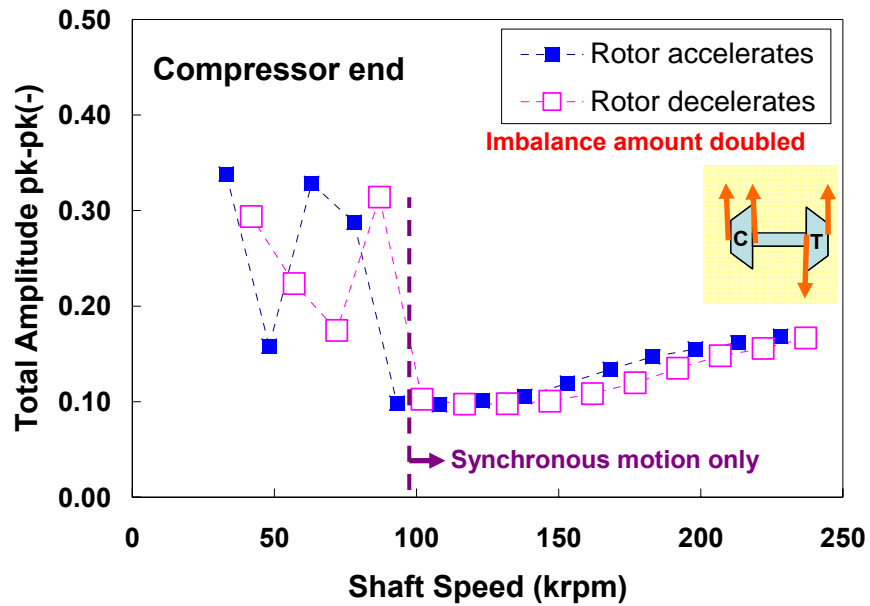
Figure 47: Total TC shaft motion (pk-pk) amplitude at the compressor end during rotor acceleration (■) and deceleration (□); imbalance distribution: turbine-back-out-of-phase; imbalance amount doubled. Shaft speed ramp rate =500 Hz/s.

CHAPTER VII

CONCLUSIONS

A frequency jump between a first and a second subsynchronous rotor whirl motions increases noise level in automotive TCs [11]. In an effort to improve turbocharger dynamic performance and to reduce noise generation levels in TC operation, the focus of this thesis is to assess factors (operating conditions and bearing performance parameters) affecting the onset and persistence of the frequency jump phenomenon.

Nonlinear predictions are conducted for a TC supported on a SFRB, operating with various conditions (oil inlet temperature and pressure), bearing geometry, rotor acceleration/deceleration rate, as well as various imbalance distribution. In addition, a linear eigenvalue analysis is conducted to predict the rotor-bearing system (RBS) damped natural frequencies. TC shaft nonlinear response predictions (at the compressor end) display, over the whole speed range typically, two subsynchronous whirl frequencies ω_1 and ω_2 corresponding to a conical mode and a cylindrical bending mode, respectively. At all operating conditions, ω_1 is present from startup (lowest shaft speed of 30 krpm) to a shaft speed $(\Omega_{bifurcation})$, where there is a frequency jump from ω_1 to ω_2. The second whirl frequency (ω_2) may persist (depending on operating conditions) up to the highest shaft speed (240 krpm, 4 kHz).

At low shaft speeds, the compressor and turbine rings operate at high static eccentricities (~ 85% of outer film clearance). As the rotor speed increases, the rings move closer to the bearing center (~ 60% of the outer film clearance). The outer film supports the hydrostatic side loads applied on the bearings, and the rotor operates at a centered position (relative to the ring).

Linear eigenvalue analysis predicts two unstable natural frequencies, characterizing a conical mode (with SFRB in conical mode) and a cylindrical bending mode (with SFRB in cylindrical mode). The two natural frequencies are closely spaced.

The first whirl frequency ω_1 follows the 2nd damped natural frequency (unstable conical mode), only at low shaft speeds up to ~80 krpm (~1.3 kHz). In addition, the rotor

synchronous response is calculated from the linear and nonlinear (at fixed shaft speed and speed transient) analyses. Predictions show discrepancies between the linear and nonlinear results. These discrepancies are due to the large rotor whirl motions predicted using nonlinear analysis, whereas in the linear analysis only small perturbations about a static equilibrium position are assumed.

Interestingly, predicted rotor subsynchronous whirl motions are similar in frequency and amplitude for most cases (regardless of operating conditions) at low shaft speeds (below~ 100 krpm) and at high shaft speeds (above~ 200 krpm). This is with the exception for cases with turbine-back-out-of-phase imbalance distribution for which the system becomes stable at high shaft speeds. Operating conditions mainly affect the TC response over a speed range (~100 krpm-200 krpm) enclosing the bifurcation speed ($\Omega_{bifurcation}$). Also, in all cases, the first whirl frequency (ω_1) (conical mode) at low shaft speeds (below 50 krpm) is 50% of the rotational frequency. In addition, at the $\Omega_{bifurcation}$, the TC rotor whirls at a frequency close to 25% of the rotor speed.

In most cases, there is an internal relation between the two whirl frequencies (ω_1 and ω_2) at the $\Omega_{bifurcation}$. Table 2 lists the corresponding internal and combined relations for all cases. For each case, the internal relations (between ω_1 and ω_2) are the same during rotor acceleration and deceleration, except for the case with turbine-back-out-of-phase (TBOP) imbalance distribution and the case with the highest shaft speed ramp rate (750Hz/s). In each case, the combined relations are different during rotor acceleration and deceleration unless the $\Omega_{bifurcation}$ is almost identical during rotor speed ramp up and ramp down cases (i.e. reduced pressure case).

The total amplitude of rotor motion at the compressor end is generally between 20% and 40% of the maximum allowed shaft motions. However, a TBOP imbalance distribution reduces the total amplitude of motion at high shaft speeds (above 100 krpm). The reason is due to the subsynchronous whirl motions disappearing at high shaft speeds. In general, predictions and test data confirm that rotor imbalance distribution greatly affects the onset speed of subsynchronous frequency appearance (or disappearance), the total amplitude of shaft motion, and the bifurcation speed.

Predictions show that a 33% increase oil supply pressure delays the onset speed of second subsynchronous whirl motion (ω_2); hence, also delaying the bifurcation speed ($\Omega_{bifurcation}$). This observation is in agreement with the test data in Ref. [31]. Also, predictions (cases with three supply temperatures studied) show that increasing the oil supply temperature leads to a decrease of the onset speed of (ω_2) whirl motion and hence, also decreases $\Omega_{bifurcation}$. Also, test data (provided by a TC manufacturer) confirms this finding (see Figs. 2 and 3). Increasing the bearing inner film length by 15% decreases the amplitude of shaft total motions. In addition, increasing the inner film length leads to rotor operation at even lower eccentricities (similar to operation at very high shaft speeds). Therefore, predictions show an increase in the first subsynchronous frequency (ω_1) near $\Omega_{bifurcation}$, which leads to a smooth transition (rather than a jump) from ω_1 to ω_2.

Note the effect of the abovementioned operating conditions and bearing parameters on response bifurcations are studied only for a few cases. Further analyses must be conducted to generalize the findings.

Predictions in most cases display hysteresis in $\Omega_{bifurcation}$ when the rotor accelerates to a top speed and decelerates from this high magnitude. Hysteresis is stronger in cases with faster acceleration/deceleration rates. Also, increasing rotor acceleration delays the onset speed of the second whirl motion (ω_2), therefore delaying the $\Omega_{bifurcation}$. The total shaft motion amplitude though, remains unchanged with rotor speed ramp rate.

Predicted results in this analysis agree well (qualitatively) with the test data in the literature and provided by a TC manufacturer. Further analysis should be done to assess the effects of clearances, ring rotation, lubricant type, and bearing outer film length on the frequency jump phenomenon. Additional imbalance distributions should be studied to assess the imbalance condition that results in small or no subsynchronous motions. In addition, validating the predictions against test data assists refinement of the predictive tool, which can save significant time and cost in TC manufacturing industry.

Table 2. The internal and combined relations (at the bifurcation speed (Ω_b)) between the two subsynchronous whirl frequencies (ω_1 and ω_2) and the Ω_b.

Case	Ω_b (Hz)	ω_1 (Hz)	ω_2 (Hz)	Internal relation	Combined relation
Baseline (up[♠])	2,750	654	815	$5\omega_1 \sim 4\omega_2$	$3\omega_1 + \omega_2 \sim \Omega_b$
Baseline (down[♥])	3,030	674	845	$5\omega_1 \sim 4\omega_2$	$2\omega_1 + 2\omega_2 \sim \Omega_b$
Reduced Pressure (up)	1,980	493	732	$3\omega_1 \sim 2\omega_2$	$\omega_1 + 2\omega_2 \sim \Omega_b$
Reduced Pressure (down)	2,000	508	732	$3\omega_1 \sim 2\omega_2$	$\omega_1 + 2\omega_2 \sim \Omega_b$
Reduced Temperature (up)	2,750	684	820	$5\omega_1 \sim 4\omega_2$	N/A
Reduced Temperature (down)	2,720	659	820	$5\omega_1 \sim 4\omega_2$	$3\omega_1 + \omega_2 \sim \Omega_b$
Increased Temperature (up)	2,500	620	801	$4\omega_1 \sim 3\omega_2$	N/A
Increased Temperature (down)	3,030	645	840	$4\omega_1 \sim 3\omega_2$	$2\omega_1 + 2\omega_2 \sim \Omega_b$
Increased Inner Length (up) [††]	2,700	762	786	N/A	N/A
Increased Inner Length (down)	2,720	762	796	N/A	N/A
Low Acceleration (+250Hz/s)	2,500	635	840	$4\omega_1 \sim 3\omega_2$	N/A
Low Deceleration (-250Hz/s)	2,620	645	811	$4\omega_1 \sim 3\omega_2$	N/A
High Acceleration (+750Hz/s)	3,120	713	850	$6\omega_1 \sim 5\omega_2$	$2\omega_1 + 2\omega_2 \sim \Omega_b$
High Deceleration (-750Hz/s)	2,150	552	786	$3\omega_1 \sim 2\omega_2$	$\omega_1 + 2\omega_2 \sim \Omega_b$
Opposed Couple Imb Dist. (up)	3,000	654	840	$4\omega_1 \sim 3\omega_2$	$2\omega_1 + 2\omega_2 \sim \Omega_b$
Opposed Couple Imb Dist. (down)	2,420	601	776	$4\omega_1 \sim 3\omega_2$	N/A
TBOP Imb Dist. (up)	2,500	591	791	$4\omega_1 \sim 3\omega_2$	$3\omega_1 + \omega_2 \sim \Omega_b$
TBOP Imb Dist. (down)	2,000	513	757	$3\omega_1 \sim 2\omega_2$	$\omega_1 + 2\omega_2 \sim \Omega_b$

[♠] Up means rotor accelerates from 30 krpm to 240 krpm with a +500 Hz/s speed ramp rate.

[♥] Down means rotor decelerates from 240 krpm to 30 krpm with a -500 Hz/s speed ramp rate.

[††] There is no frequency jump in this case (both during rotor acceleration and deceleration), rather, there is a smooth transition between the two whirl frequencies (ω_1 and ω_2).

REFERENCES

[1]   San Andrés, L., Rivadeneira, J. C., Chinta, M., Gjika, K., and LaRue, G., 2007, "Nonlinear Rotordynamics of Automotive Turbochargers: Predictions and Comparisons to Test Data," ASME J. Eng. Gas Turb. Power, **129**, pp.488-493.

[2]   Haller, C. L., Killinger, A. G., and Smith, L. A., 1995, "Methods to Reduce Diesel Engine Exhaust Emissions at Established Installations to Comply with the Clean Air Act," ASME/ ICE Journal, **4**, pp.75-84.

[3]   Maruyama, A., 2007, "Predictions of Automotive Turbocharger Nonlinear Dynamic Forced Response with Engine-Induced Housing Excitations: Comparisons to Test Data," M.S. thesis, Texas A&M University, College Station, TX.

[4]   San Andrés, L., and Kerth, J., 2004, "Thermal Effects on the Performance of Floating Ring Bearings for Turbochargers," *Proc. of the Inst. of Mech. Eng., Part J, J. Eng. Tribol.*, **218**(5), pp. 437-450.

[5]   Holt, C., San Andrés, L., Sahay, S., Tang, P., LaRue, G., and Gjika, K., 2005, "Test Response and Nonlinear Analysis of a Turbocharger Supported on Floating Ring Bearings," ASME J. Vib. Acoust., **127**, pp. 107-115.

[6]   Gjika, K., San Andrés, L., and LaRue, G., 2007, "Nonlinear Dynamic Behavior of Turbocharger Rotor-Bearing Systems with Hydrodynamic Oil Film and Squeezed Film Damper in Series: Prediction and Experiment," *Proc. of the 21st Biennial Conference on Mechanical Vibration and Noise*, Las Vegas, NV, September 4-7, Paper No. DETC 2007-34136.

[7]   San Andrés, L., 2008, *XLFEMSFRB™ v8.0 Software Suite*, Tribology Group, Turbomachinery Laboratory, Texas A&M University, College Station, TX.

[8]   *XLTRC^2™ Rotordynamics Software Suite v.2.22*, 2008, Turbomachinery Laboratory, Texas A&M University, College Station, TX.

[9]   Gjika, K., 2004, *Bearing Systems Behavior - Subsynchronous Vibration and Relationship with Noise: Applications to PV Turbochargers,* Honeywell Turbo Technologies Proprietary, France.

[10]   Gjika, K., 2006, *Sur le comportement dynamique non linéaire des turbo compresseurs d'automobile*, Partenariat entre le Laboratoire de Mécanique des Contacts et des Structures (LAMCOS, UMR CNRS 5514 de L'INSA de Lyon) et Honeywell Turbo Technologie.

[11]   Gjika, K., Personal Communication, 5 May, 2009.

[12]   Yamamoto, T., and Ishida, Y., 2001, *Linear and Nonlinear Rotordynamics: A Modern Treatment with Applications,* Wiley, New York.

[13]   Nayfeh, A. H., and Balachandran, B., 1989, "Modal Interactions in Dynamical and Structural Systems," ASME Appl Mech Rev, **42**, pp.175-201.

[14]   Xia, S., 2006, *Unbalance Configuration Effect on Subsynchronous Shift*, Honeywell Turbo Technologies Internal Presentation and Proprietary, France.

[15]   Sahay, S. N., and LaRue, G., 1997, "Turbocharger Rotordynamic Instability and Control," NASA CP3344, pp. 247-257.

[16]   Noah, S., and Sundararajan, P., 1995, "Significance of Considering Nonlinear Effects in Predicting the Dynamic Behavior of Rotating Machinery," J. Vibration and Control, **1**, pp. 431-458.

[17]   Shaw, J., and Shaw, S. W., 1990, "The Effect of Unbalance on Oil Whirl," Nonlinear Dynamics, **1**, pp. 293-311.

[18]   Wang, J. K., and Khonsari, M. M., 2006, "On the Hysteresis Phenomenon Associated with Instability of Rotor-Bearing Systems," ASME, **128**, pp. 188-196.

[19]   Pinkus, O., 1956, "Experimental Investigation of Resonant Whip," Trans. ASME, **78**, pp. 975-983.

[20]   Muszynska, A., 1998, "Transition to Fluid-Induced Stability Boundaries Self-Excited Vibrations of a Rotor and Instability Threshold 'Hysteresis'," *Proc. of ISROMAC-7, The 7th International Symposium on Transport Phenomena and Dynamics of Rotating Machinery*, February, Honolulu, HI, pp. 775-784.

[21]   Choi, S. K., and Noah, S. T., 1994, "Mode Locking and Chaos in a Modified Jeffcott Rotor with a Bearing Clearance," J. Appl. Mech., **61** (1), pp. 131-138.

[22]   Brown, R. D., Drummond, G., and Addison, P. S., 2000, "Chaotic Response of a Short Journal Bearing," ASME J. Appl. Mech., **214**, pp. 387- 400.

[23]   Inoue, T., and Ishida, Y., 2003, "Chaotic Vibration and Internal Resonance Phenomena in Rotor Systems (Part I: Theoretical Analysis)," *Proc. of Design Engineering Technical Conferences and Computers and Information in Engineering Conference,* Chicago, IL, September 2-6, **5(A),** pp. 867-876.

[24] Nayfeh, T. A., Asrar, W., and Nayfeh, A. H., 1992, "Three-Mode Interactions in Harmonically Excited Systems with Quadratic Nonlinearities," Nonlinear Dynamics, **3**, pp. 385-410.

[25] Childs, D., 1993, *Turbomachinery Rotordynamics: Phenomena, Modeling, & Analysis*, John Wiley & Sons, Inc., New York.

[26] Ishida, Y., and Inoue, T., 2004, "Internal Resonance Phenomena of the Jeffcott Rotor with Nonlinear Spring Characteristics," J. Vibration and Acoustics, **126**, pp. 476-484.

[27] Shaw, J., and Shaw, S.W., 1991, "Non-Linear Resonance of an Unbalanced Rotating Shaft with Internal Damping," J. Sound Vib., **147**, pp. 435-451.

[28] Yamamoto, T., and Yasuda, K., 1977, "On the Internal Resonance in a Nonlinear Two-Degree-of-Freedom system (Force Vibrations near the Lower Resonance Point when the Natural Frequencies Are in the Ratio 1:2)," Bull. JSME, **20**, pp. 168-175.

[29] Asmis, K. G., and Tso, W. K., 1972, "Combination and Internal Resonance in a Nonlinear Two-Degree-of-Freedom System," J. Appl. Mech., **39**, pp. 832-834.

[30] Mook, D. T., HaQuang, N., and Plaut, R. H., 1986, "The Influence of an Internal Resonance on Nonlinear Structural Vibrations under Combination Resonance Conditions," J. Sound Vib., **104**, pp. 229-241.

[31] Schweizer, B., and Sievert, M., 2009, "Nonlinear Oscillations of Automotive Turbocharger Turbines," J. Sound Vib., **321**, pp. 955-975.

[32] Kerth, J., 2003, "Prediction and Measurement of the Rotordynamic Response of an Automotive Turbocharger with Floating Ring Bearings," M.S. thesis, Texas A&M University, College Station, TX.

[33] Rivadeneira, J. C., 2005, "Predictions Versus Measurements of Turbocharger Nonlinear Dynamic Response," M.S. thesis, Texas A&M University, College Station, TX.

[34] San Andrés, L., 2007, *Project Progress Report #41*, Proprietary, Honeywell Turbo Technologies, May, Texas A&M University, College Station, TX.

[35] Taylor, R. I., 1999, "The Inclusion of Lubricant Shear Thinning in the Short Bearing Approximation," Proc. Instn Mech Engrs, **213** (1), pp. 35-46.

[36]   Tsuruta, Y., and Tsuda, K., 1986, "Investigation into an Effect of Floating Bush Bearing, in Suppressing Oil-Whip at Higher Shaft Speed," J. of JSLE, **7**, pp. 135-140.

[37]   Nelson, H. D., and Meacham, H., 1981, "Transient Analysis of Rotor Bearing System Using Component Mode Synthesis," *Proc. of ASME Gas Turbine Conference and Product Show,* Houston, TX, March 9-12.

[38]   Paz, M., and Leigh, W. E., 2004, *Structural Dynamics*, Kluwer Academic Publishers, Norwell, MA.

[39]   San Andrés, L., 2008, "Modern Lubrication Theory, Notes 4. Static Load Performance of Plain Journal Bearings," Texas A&M University, pp.1-14, 2 Feb. 2009, http://phn.tamu.edu/TRIBGroup.

[40]   Zeidan, F. Y., and Vance, J. M, 1990, "Cavitation Regimes in Squeeze Film Dampers and Their Effect on the Pressure Distribution," Tribol. Trans., **33**, pp. 447-453.

[41]   Rezvani, M. A., and Hahn, E. J., 1996, "An Experimental Evaluation of Squeeze Film Dampers without Centralizing Springs," Tribol. Intl. , **29** (1), pp. 51-59.

[42]   Tonnesen, J., 1976, "Experimental Parametric Study of a Squeeze Film Bearing," J. Lub. Tech., **98**, pp.206-213.

[43]   San Andrés, L., 2008, *Project Progress Report #50*, Proprietary, Honeywell Turbo Technologies, February, Texas A&M University, College Station, TX.

[44]   San Andrés, L., 2009, *Project Progress Report #57*, Proprietary, Honeywell Turbo Technologies, January, Texas A&M University, College Station, TX.

[45]   San Andrés, L., Personal Communication, 9 April, 2009.

APPENDIX A

PHYSICAL PROPERTIES OF TURBOCHARGER ROTOR AND SFRB

Appendix A is removed, proprietary material to Honeywell Turbo Technologies.

APPENDIX B

FILTERED MODE SHAPES

In order to determine the rotor whirling mode corresponding to a certain subsynchronous frequency, the nonlinear predictions of the shaft motion are obtained at 5 TC rotor locations (1: compressor end, 2: compressor backface, 3: compressor bearing, 4: turbine bearing, 5: turbine end) shown in Figure B1.   The Discrete Fourier Transforms (DFT) of the predicted results are obtained over a range of shaft speeds. The DFT consist of a real part (Re) and an imaginary part (Im). The frequency of interest is selected from the DFTs and the corresponding orbits are generated, using equation B.1 [45], for the specified frequency, at each of the 5 rotor locations.

$$
\begin{aligned}
X &= \mathrm{Re}(DFT_X)\cos(\theta) - \mathrm{Im}(DFT_X)\sin(\theta) \\
Y &= \mathrm{Re}(DFT_Y)\cos(\theta) - \mathrm{Im}(DFT_Y)\sin(\theta)
\end{aligned}
\tag{B.1}
$$

where DFT_X and DFT_Y are the Discrete Fourier Transforms of the time data rotor motions along the horizontal and vertical directions, respectively. Also, θ is a parameter that varies between 0 and 2π.
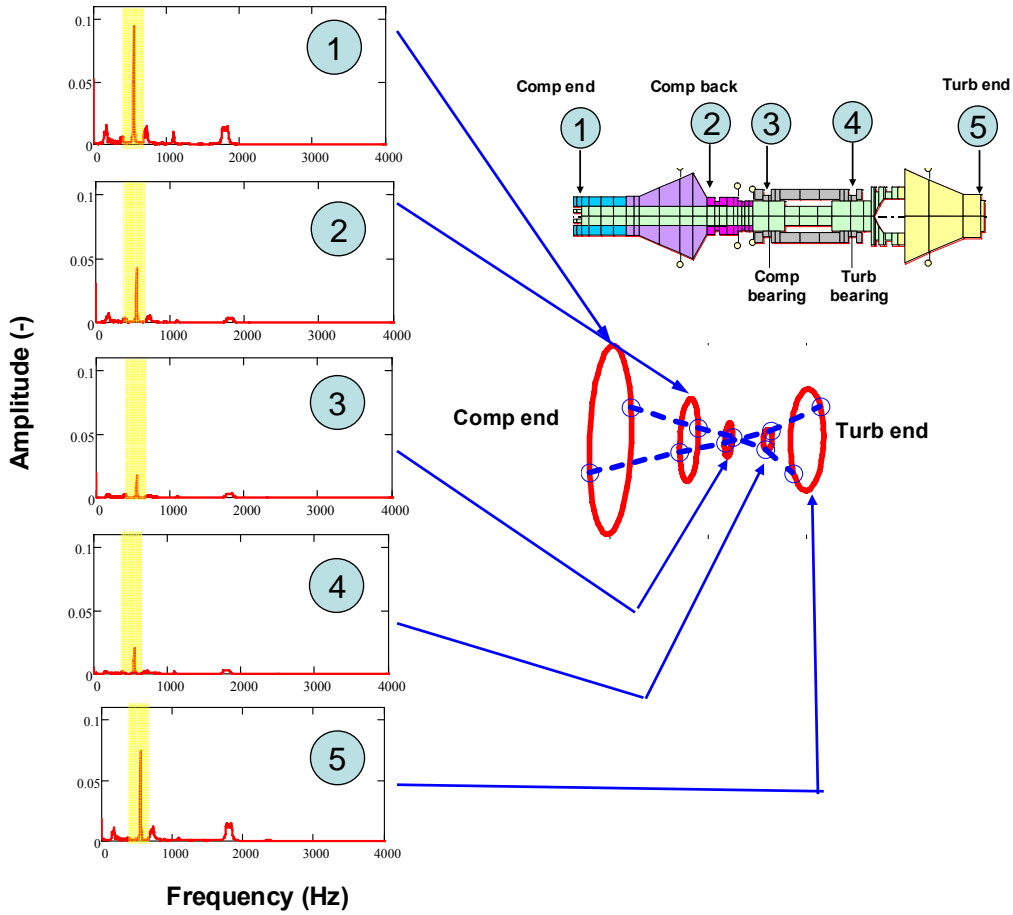
Figure B.1: TC rotor model and the 5 axial stations where responses are obtained. DFT amplitude of shaft motion at the corresponding 5 stations; a filtered mode shape.

APPENDIX C

PREDICTED WATERFALLS OF TC ROTOR MOTION FOR VARIOUS CASES

Figures C.1-C.6 depict the predicted waterfalls of rotor motion (along the vertical direction) at the compressor end. The captions list the operating conditions. Motions are normalized with respect to the maximum physical limit at compressor end.
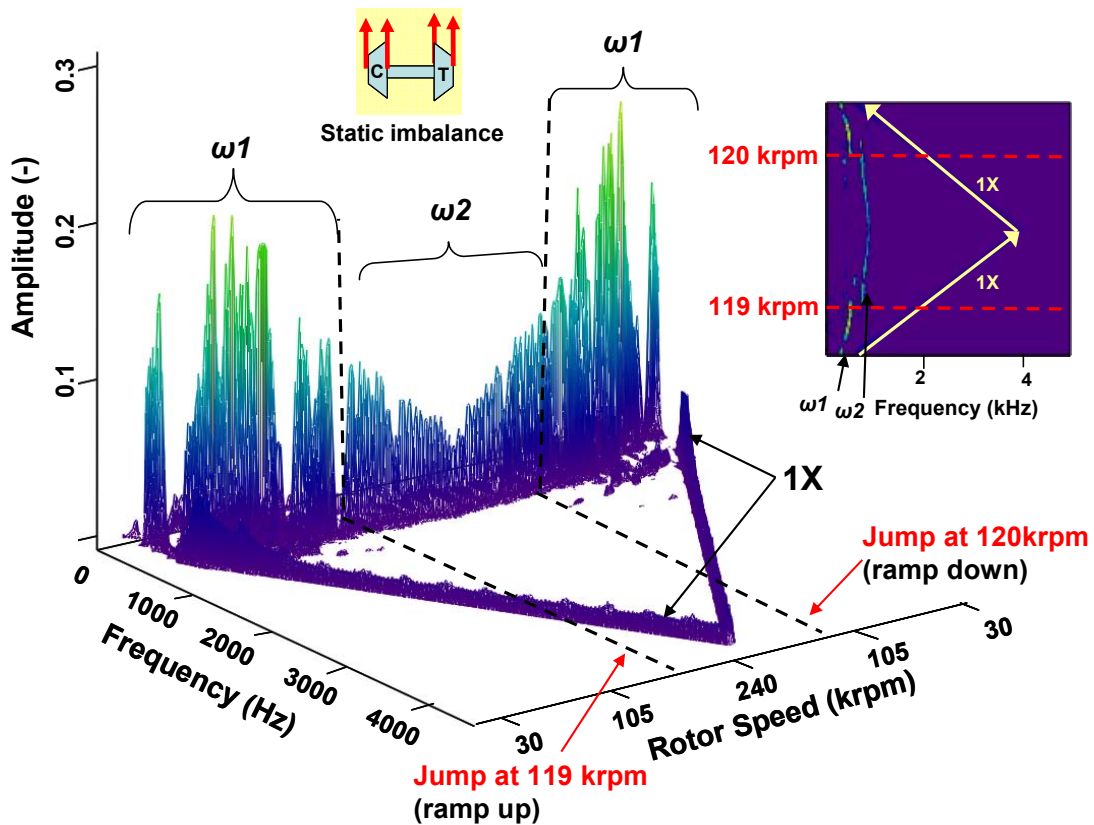

Figure C.1: Waterfalls of predicted TC shaft motion at the compressor end, vertical direction; static imbalance distribution, speed ramp rate = 500Hz/s. Oil supply pressure reduced by 33%.
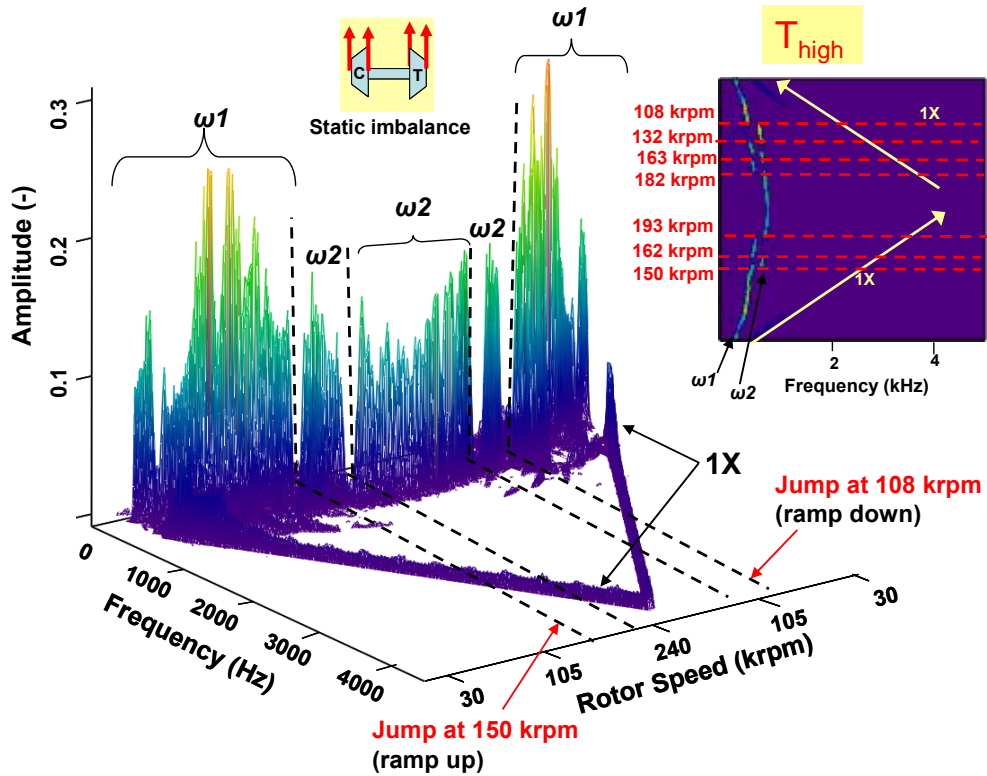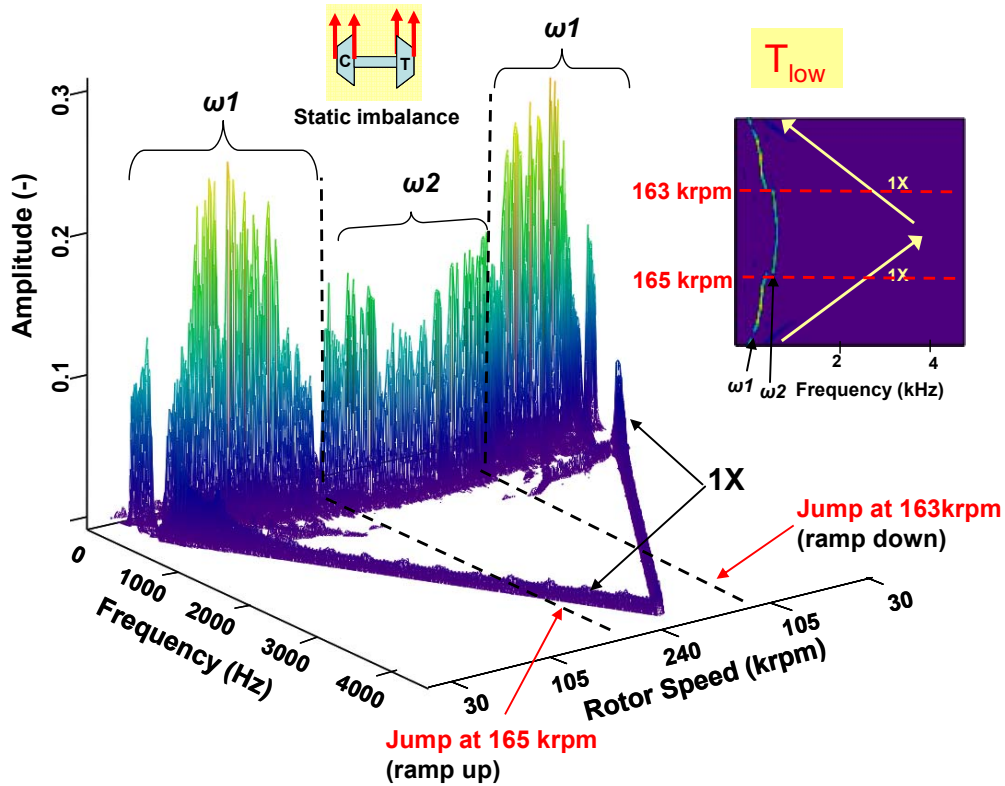
Figure C.2: Waterfalls of predicted TC shaft motion at the compressor end, vertical direction; oil supply temperature: (TOP) reduced (T_{low}), (BOTTOM) increased (T_{high}), static imbalance distribution, speed ramp rate = 500Hz/s.
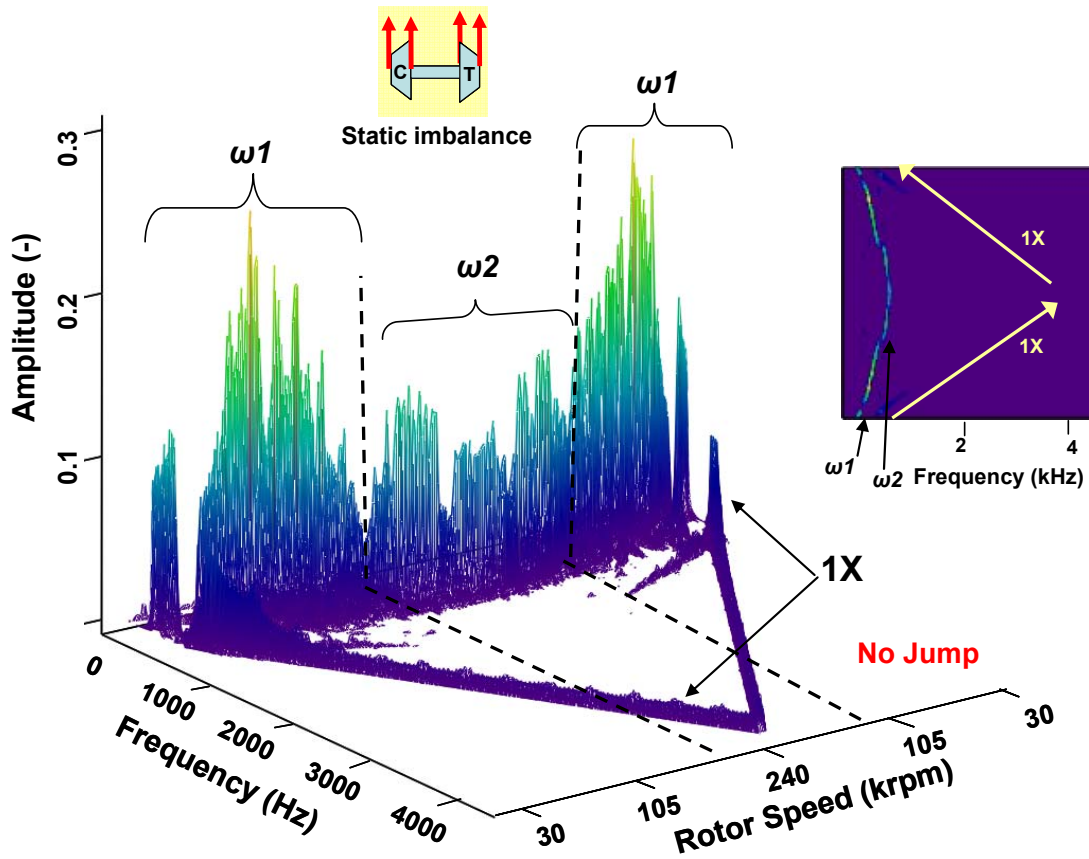
Figure C.3: Waterfalls of predicted TC shaft motion at the compressor end, vertical direction; static imbalance distribution, speed ramp rate = 500Hz/s. Bearing inner film length increased by 15%.
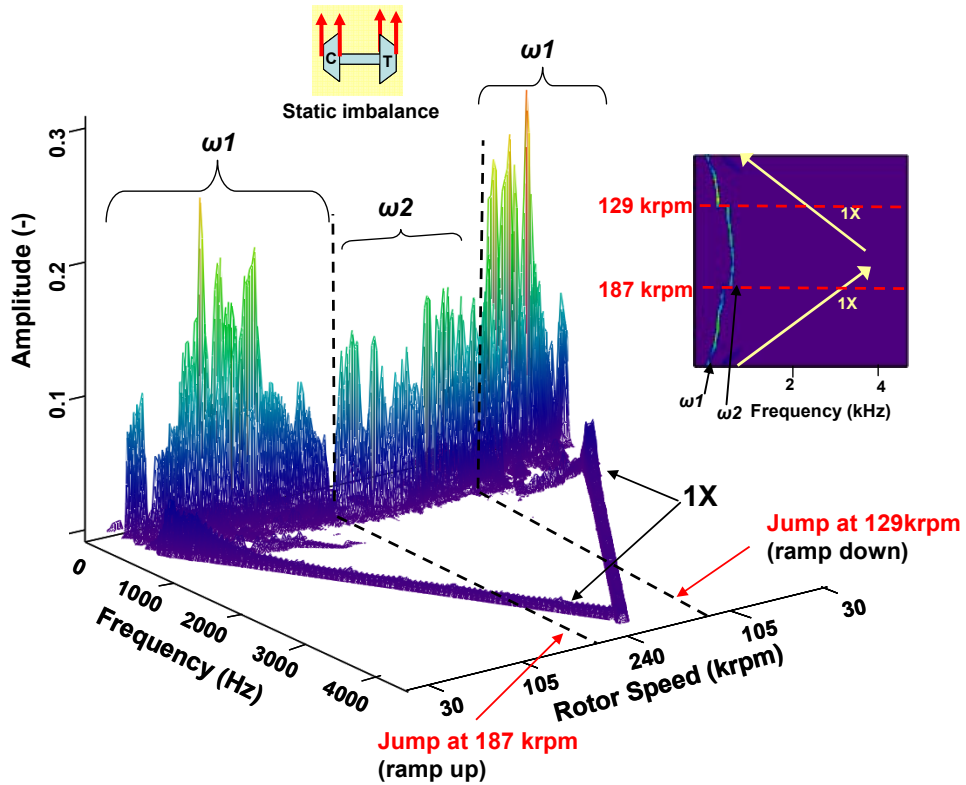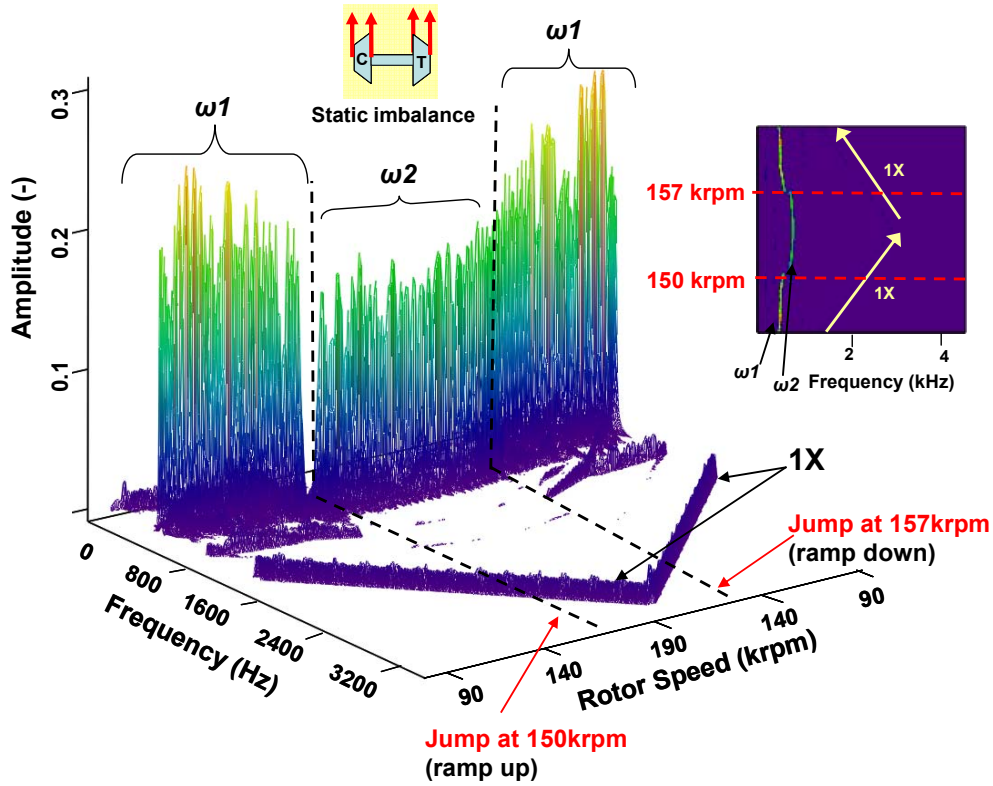
Figure C.4: Waterfalls of predicted TC shaft motion at the compressor end, vertical direction; static imbalance distribution, speed ramp rate: (TOP) 250Hz/s, (BOTTOM) 750Hz/s.
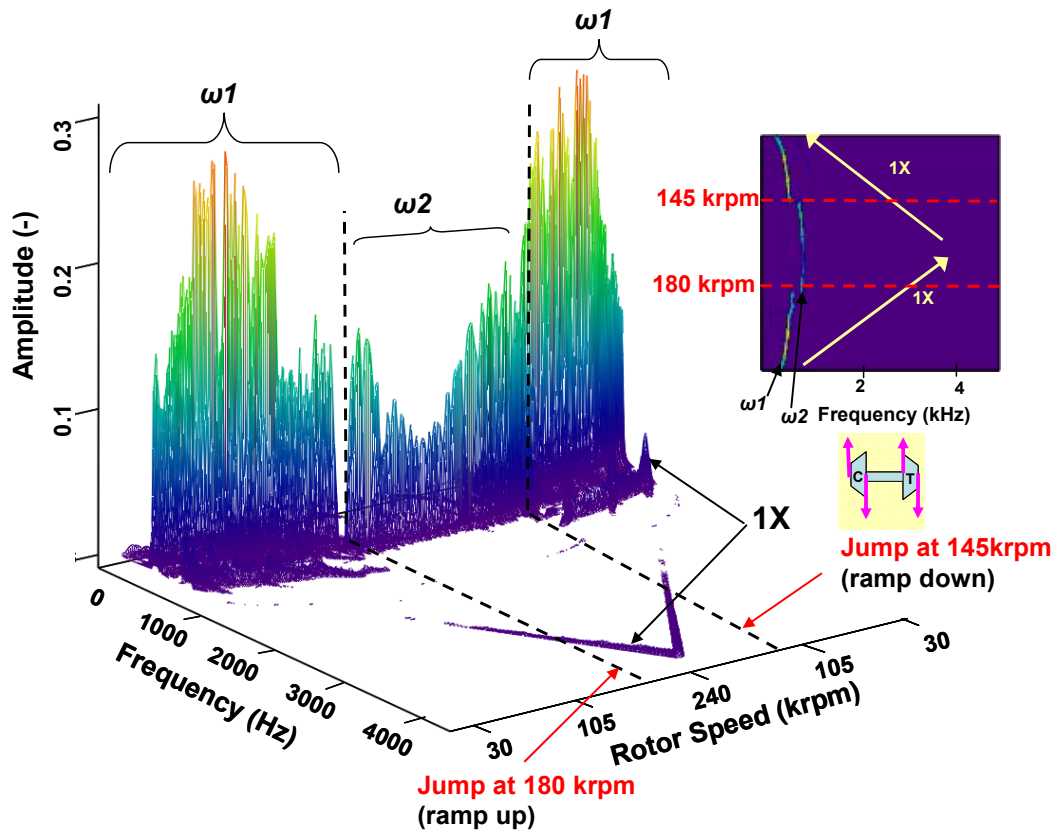
Figure C.5: Waterfalls of predicted TC shaft motion at the compressor end, vertical direction; imbalance distribution: opposed couple, speed ramp rate= 500Hz/s.
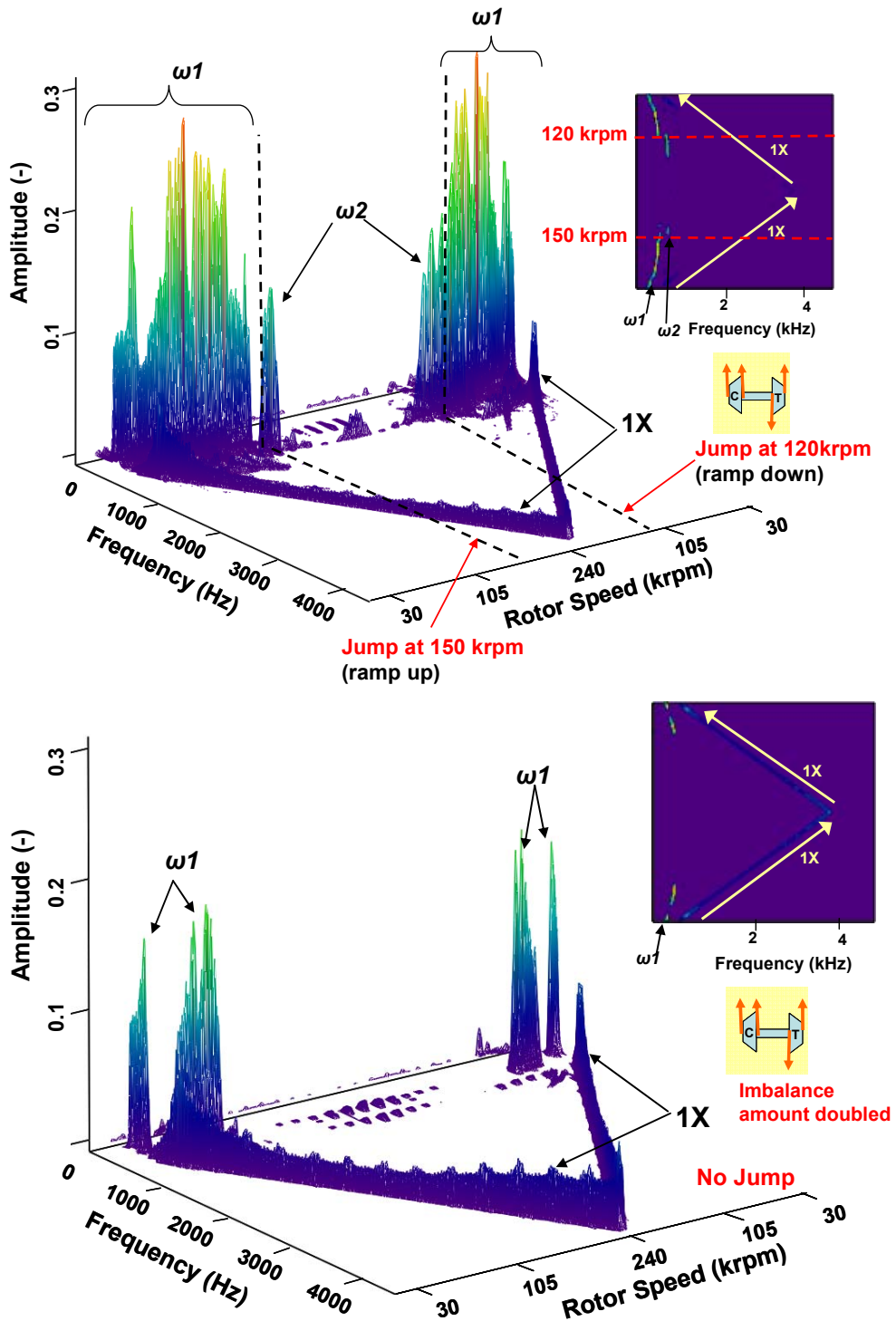
Figure C.6: Waterfalls of predicted TC shaft motion at the compressor end, vertical direction; imbalance distribution: opposed couple, (BOTTOM) imbalance amount doubled, speed ramp rate= 500Hz/s.

APPENDIX D

ROTOR BEARING SYSTEM EQUATIONS OF MOTION

Nomenclature

$[M]$	Global translational mass matrix
$[M_R]$	Global rotational mass matrix
$[C]$	Global damping matrix
$[G]$	Global gyroscopic matrix
$[K]$	Global Stiffness matrix
$\{F\}$	Vector of (external and bearing reaction) forces and moments
$F_{bearing}$	Bearing reaction forces (expressed as impedance formulas)
M	External moment
m	Imbalance mass
e	Mass eccentricity (distance between center of mass and axis of rotation)
ϕ	Rotor angular displacement (about axis of rotation)
$\dot{\phi}$	Rotor angular speed
$\ddot{\phi}$	Rotor angular acceleration
W	Static load (i.e. rotor-bearing weight, hydrostatic side loads)
X	Rotor displacement in horizontal direction
$\dot{X}$	Rotor velocity in horizontal direction
$\ddot{X}$	Rotor acceleration in horizontal direction
Y	Rotor displacement in vertical direction
$\dot{Y}$	Rotor velocity in vertical direction
$\ddot{Y}$	Rotor acceleration in vertical direction
θ	Rotor angular displacement

Subscripts

X	Along the horizontal direction
Y	Along the vertical direction

The equations of motions for a rotor bearing system with variable rotational speed ($\dot{\phi}$) are [25]

$$\left([M]+[M_R]\right)\{\ddot{u}\}+[C]\{\dot{u}\}-[G]\dot{\phi}\{\dot{u}\}+[K]\{u\}=\{F\} \qquad \text{(D.1)}$$

Note the rotor model consists of 42 elements (total of 43 nodes[Ψ]). For each node the displacement, velocity, acceleration and force-moment vectors are defined as:

$$\{u\}=\begin{Bmatrix} X \\ \theta_X \\ Y \\ \theta_Y \end{Bmatrix},\{\dot{u}\}=\begin{Bmatrix} \dot{X} \\ \dot{\theta}_X \\ \dot{Y} \\ \dot{\theta}_Y \end{Bmatrix},\{\ddot{u}\}=\begin{Bmatrix} \ddot{X} \\ \ddot{\theta}_X \\ \ddot{Y} \\ \ddot{\theta}_Y \end{Bmatrix},\{F\}=\begin{Bmatrix} F_X \\ M_X \\ F_Y \\ M_Y \end{Bmatrix} \qquad \text{(D.2)}$$

The forces in horizontal and vertical directions are defined as:

$$\{F_X\}=F_{X\_bearing}+m.e\left[\dot{\phi}^2\cos(\phi)+\ddot{\phi}\sin(\phi)\right] \qquad \text{(D.3)}$$

$$\{F_Y\}=F_{Y\_bearing}+m.e\left[\dot{\phi}^2\sin(\phi)-\ddot{\phi}\cos(\phi)\right]+W \qquad \text{(D.4)}$$

$$F_{bearing}=\begin{Bmatrix} F_{X\_bearing} \\ F_{Y\_bearing} \end{Bmatrix},\ F_{bearing}=f(X,\dot{X},Y,\dot{Y}) \qquad \text{(D.5)}$$

The bearing reaction forces have cross-coupling terms that couple equations (D.3) and (D.4). Note the bearing reaction loads are expressed as impedance formulas and depend on the rotor instantaneous position and velocity. Therefore, the bearing reaction loads are calculated at each time step and integrated into the equations of motion.

[Ψ] Each station in the finite element rotor model in Fig 9 is defined as a node

VITA

Name: Arian Vistamehr

Address: 10735 Mist Haven Terrace, Rockville, MD 20852

Email Address: arianvista@yahoo.com

Education: A.S., Mechanical Engineering, Montgomery College, Rockville, MD,
                    2004
                    B.S., Mechanical Engineering, Texas A&M University, 2007
                    M.S., Mechanical Engineering, Texas A&M University, 2009